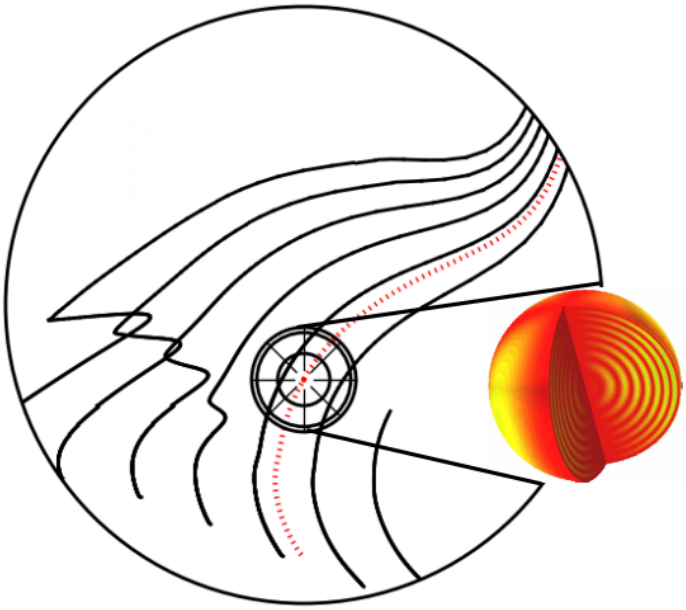

Asteroseismic characterisation of exoplanet-host stars in preparation for NASA's TESS and ESA's PLATO space missions

Benard Nsamba

Programa Doutoral em Astronomia

Departamento de Física e Astronomia

2020

Orientadores

Mário João P. F. G. Monteiro

Professor Associado, Faculdade de Ciências da Universidade do Porto

& Investigador, Instituto de Astrofísica e Ciências do Espaço (IA)

Tiago L. Campante

Professor Auxiliar Convidado, Faculdade de Ciências da Universidade do Porto

& Investigador, Instituto de Astrofísica e Ciências do Espaço (IA)

Asteroseismic characterisation of exoplanet-host stars in preparation for NASA's TESS and ESA's PLATO space missions

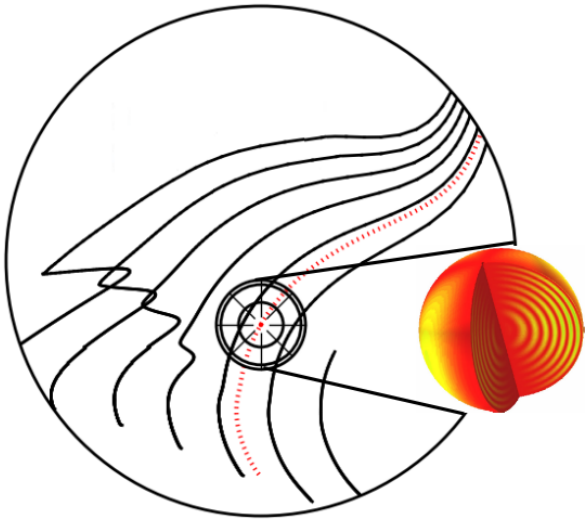

Benard Nsamba

Centro de Astrofísica da Universidade do Porto
Faculdade de Ciências da Universidade do Porto

A thesis submitted for the degree of
Doutor em Astronomia (3º Ciclo da Universidade do Porto)

January 2020

The cover figure is composed of images taken from
http://bison.ph.bham.ac.uk/spaceinn/aims/tutorial/ and
https://www.mps.mpg.de/helioseismology-asteroseismology/research/.

"We should be unwise to trust scientific inference very far when it becomes divorced from opportunity for observational test".

The Internal Constitution of the Stars (Eddington, 1926)

Abstract

New insights on stellar evolution and stellar interior physics are being made possible by asteroseismology, i.e., the study of stars by the observation of their natural, resonant oscillations. Asteroseismology is proving to be particularly significant for the study of solar–type stars, in great part due to the exquisite data that have been made available by NASA's *Kepler* space telescope. An increase in the number of stars with detected oscillations by several orders of magnitude is expected due to the recently launched NASA's Transiting Exoplanet Survey Satellite (TESS) and the future ESA's PLAnetary Transits and Oscillations of stars (PLATO) missions. The information contained in stellar oscillations allows the internal stellar structure to be constrained to unprecedented levels, while also allowing fundamental stellar properties (e.g., mean density, radius, mass, and age) to be precisely determined.

This thesis is composed of seven chapters. Chapter one details a historical background of stellar pulsations/variability. Since this thesis is centered on solar–type oscillations, an extensive discussion is placed on the stochastic excitation that drives such oscillations. Chapter two gives a review of the stellar structure equations, stellar pulsation equations, and assumptions considered when generating stellar models and their corresponding adiabatic oscillation frequencies, with insight on how they are handled by the stellar evolution and pulsation codes, namely, MESA (Modules for Experiments in Stellar Astrophysics) and GYRE, respectively. Chapter three presents the subjects at the core of this thesis, mainly involving discussions on the stellar model physics explored (namely, atomic diffusion, solar metallicity mixtures, and nuclear reaction rates) and forward modelling techniques applied. The major goal of this thesis is to quantify the systematic uncertainties on the derived stellar parameters arising from the model input physics when applying asteroseismic modelling techniques.

Chapter four is devoted to the scientific results focusing on the systematic uncertainties on the inferred stellar parameters arising from not only the essential model physics adopted in asterosesismic modelling of low–mass main sequence stars but also the different surface correction recipes. The model physics explored in this chapter are atomic diffusion and solar metallicity mixtures. Considering α Centauri A as

a reference star, chapter five explores how the adopted nuclear reaction rates affect the properties of stellar cores. This is mainly because they contribute towards the determination of the dominant energy production process taking place in stellar cores. A distinct addition to the optimisation process in this chapter, is the inclusion of a precise interferometric radius. This complements the seismic and classical constraints, thus aiding in tightly constraining the stellar model selection process. Chapter six further explores the impact of microphysics on the core properties of α Centauri A. This chapter addresses the contribution of both metallicity mixtures and the corresponding opacities to the nature of the core of α Centauri A. Conclusions and future prospects are highlighted in chapter seven.

The findings of this thesis confirm that atomic diffusion is a vital transport process in low–mass stars and when neglected in the modelling yields systematic uncertainties of 0.5%, 0.8%, 2.1%, and 16% in mean density, radius, mass, and age, respectively, with systematic uncertainties in mass and age greater than the statistical uncertainties. The research findings in this thesis also show that the nuclear reaction rates and solar metallicity mixtures adopted in modelling stars in the transition region between models with and without convective cores (i.e., between 1.1 $M_{\odot}$ and 1.15 $M_{\odot}$) have a significant impact on the properties of stellar cores. In an effort to ascertain the nature of the core of α Centauri A, the findings in this thesis show that $\gtrsim 70\%$ of the models reproducing the revised dynamical mass of α Centauri A have convective cores, regardless of solar metallicity mixtures and nuclear reaction rates adopted. Based on these results, α Centauri A may be adopted in the calibration of stellar model parameters when modelling solar–like stars with convective cores. Furthermore, the research activities carried out in this thesis have contributed to the testing of the recently developed asteroseismic optimisation tool AIMS (Asteroseismic Inference on a Massive Scale). Finally, the combination of the state–of–the–art tools employed in this thesis allowed for important contributions to a series of "hare and hounds" activities involving both main–sequence and subgiant stars and directed towards the preparation of ESA's PLATO mission.

Sumário

A Astrossismologia consiste no estudo de estrelas através da observação dos seus modos próprios de oscilação, permitindo novas descobertas sobre a evolução estelar e a física do interior de estrelas. A Astrossismologia tem-se mostrado particularmente importante para o estudo de estrelas de tipo solar, em grande parte devido aos dados de elevada qualidade disponibilizados pelo telescópio espacial da NASA, o Kepler. Espera-se também um aumento de várias ordens de magnitude no número de estrelas com oscilações detetadas com o recém-lançado Transiting Exoplanet Survey Satellite (TESS) da NASA, assim como a futura missão da ESA PLAnetary Transits and Oscillations of stars (PLATO). A informação obtida através das medições destas oscilações estelares permite-nos conhecer a estrutura interna de uma estrela a um nível sem precedentes, possibilitando também uma caracterização precisa de parâmetros estelares fundamentais (e.g., densidade média, raio, massa e idade).

Esta tese é composta por sete capítulos. O Capítulo 1 apresenta uma revisão detalhada da história do estudo das pulsações e variabilidade estelares. Uma vez que esta tese se foca nas oscilações de estrelas de tipo solar, uma seção extensa é dedicada à excitação estocástica que está na origem deste tipo de oscilações. O Capítulo 2 contém uma revisão das equações de estrutura estelar e das equações das oscilações estelares. Abordam-se ainda algumas das hipóteses e equações que são usadas no cálculo de modelos estelares e das correspondentes frequências de oscilação adiabáticas, com destaque para o tratamento usado pelos códigos de evolução estelar MESA (Modules for Experiments in Stellar Astrophysics) e GYRE, respetivamente. O Capítulo 3 apresenta os temas centrais desta tese, em particular a discussão sobre a física estelar explorada (nomeadamente, difusão atómica, abundâncias de metais e taxas de reações nucleares) e as técnicas de modelização direta usadas.

O Capítulo 4 é dedicado aos resultados científicos produzidos quando se estuda as incertezas sistemáticas dos parâmetros estelares inferidos. Estas incertezas surgem, não só da física fundamental adotada na modelização sísmica de estrelas de sequência principal de baixa massa, mas também das diferentes formas de correção do efeito de superfície. As descrições físicas exploradas neste capítulo são a difusão atómica

e as abundâncias de metais. Considerando α Centauri A como estrela de referência, o Capítulo 5 explora como as taxas de reação nuclear escolhidas podem afetar as propriedades do núcleo estelar. Tal deve-se principalmente ao seu contributo para a determinação do processo dominante de produção de energia que tem lugar no núcleo da estrela. Uma outra adição ao processo de optimização descrito neste capítulo é a inclusão de uma medida precisa do raio interferométrico. Este dado complementa as restrições sísmicas e clássicas e ajuda a limitar o processo de seleção de modelos estelares compatíveis com as observações. O Capítulo 6 explora o impacto da microfísica nas propriedades do núcleo de α Centauri A. Este capítulo também explora as contribuições, tanto das abundâncias de metais como das opacidades correspondentes, para a natureza do núcleo de α Centauri A.

As conclusões e os planos para o futuro são abordados no Capítulo 7. De referir em particular que esta tese veio confirmar que a difusão atómica é um processo de transporte vital nas estrelas de baixa massa, e que, quando negligenciada nos modelos, leva a incertezas sistemáticas de 0.5%, 0.8%, 2.1%, e 16% na densidade média, raio, massa, e idade, respetivamente, com incertezas sistemáticas na massa e idade superiores às incertezas estatisticas. O trabalho desenvolvido revelou também que as taxas de reação nuclear e as abundâncias de metais no Sol, adotadas na modelização de estrelas nos regimes de transição entre modelos com e sem núcleos convectivos (isto é, entre 1.1 $M_{\odot}$ e 1.15 $M_{\odot}$), têm um impacto significativo nas propriedades dos núcleos estelares. Num esforço para perceber a natureza do núcleo de α Centauri A, os resultados apresentados nesta tese mostram que $>\sim$ 70% dos modelos que reproduzem o valor revisto da massa dinâmica de α Centauri A têm núcleo convectivo, independentemente das abundâncias de metais e taxas de reação nuclear que são adotadas. Com base nestes resultados, confirma-se que α Centauri A pode vir a ser usada na calibração dos parâmetros de modelos estelares obtidos na modelização de estrelas do tipo solar com núcleos convectivos. Adicionalmente, o trabalho desenvolvido para esta tese contribuiu ainda para o teste da ferramenta recentemente desenvolvida de optimização astrossísmica AIMS (Asteroseismic Inference on a Massive Scale). Finalmente, a combinação das ferramentas que foram desenvolvidas/utilizadas nesta tese permitiu obter várias contribuições importantes para outros estudos de estrelas na sequência principal e de estrelas sub-gigantes, no contexto da preparação da missão PLATO da ESA.

To Racheal, my parents, and all the dream chasers in the world.

Acknowledgements

I would like to express my gratitude to both my supervisors, Prof. Mário João P. F. G. Monteiro and Dr. Tiago L. Campante, for their unconditional support and invaluable suggestions throughout the whole period of my doctoral studies in Portugal. I wish to convey my utmost thanks and sincere gratitude to Dr. Tiago L. Campante for his very careful, diligent, detailed, and precise suggestions that were of enormous help to me. Your enthusiasm and interest in my research activities acted as a source of great motivation throughout the period of my PhD. I am indeed fortunate to have Prof. Mário João P. F. G. Monteiro as one of my supervisors. Your guidance, support, physical presence despite your busy schedule, and ability to calm my worries, made the accomplishment of the goals of this thesis possible.

In a special way, I wish to express my deepest appreciation to Dr. Margarida S. Cunha, for her insightful advice, suggestions, and encouragement. Your support played a significant role to the completion of my research work. I am deeply grateful to the entire asteroseismology group and my colleagues at CAUP, namely, Ms. Raquel Albuquerque, Ms. Solène Ulmer-Moll, Dr. Sérgio Sousa, Dr. Jason Neal, Dr. Mathieu Vrard, Dr. Morgan Deal, and Dr. Diego Bossini. I also thank my collaborators, Dr. Ben M. Rendle and Dr. Andrea Miglio at the University of Birmingham in the United Kingdom, Dr. Daniel Reese at LESIA – Observatoire de Paris in France, Dr. Kuldeep Verma at the Stellar Astrophysics Centre, Aarhus University in Denmark, Dr. Antonio García Hernández at University of Granada in Spain, and Dr. Chen Jiang at the School of Physics and Astronomy – Sun Yat-sen University in China.

I am indebted to my fiancée Racheal Nyangoma and the dear members of my family. I deeply appreciate your extraordinary level of patience, tolerance, love, and warm encouragement during my research stay in Portugal. I also wish to offer my special thanks to Dr. Cosmos Dumba, Dr. Joseph Ssenyonga, and Dr. Francis Bajunirwe at Mbarara University of Science and Technology in Uganda for their immeasurable support and inspiration in both my academic career and personal life.

I acknowledge the financial support provided during the course of my research work by the Fundação para a Ciência e a Tecnologia (FCT, Portugal) through PHD::SPACE,

an FCT PhD program, by means of Grant PD/BD/113744/2015. I am also grateful for the research facilitates and support rendered to me by the Instituto de Astrofísica e Ciências do Espaço during the period of my research stay. This work was supported by Fundação para a Ciência e a Tecnologia (FCT, Portugal) through national funds (UID/FIS/04434/2013) and by FEDER through COMPETE2020 (POCI-01-0145-FEDER-007672). I also acknowledge financial support from the COMPETE2020 projects; POCI-01-0145-FEDER-030389 & FCT: PTDC/FIS-AST/30389/2017 (Breaking through outstanding problems in stellar evolution with ultra-precise space-based photometry — BreakStarS), and POCI-01-0145-FEDER-028953 & FCT: PTDC/FIS-AST/28953/2017 (Exploring exoPlanets wIth CHEOPS — EPIC).

Porto, 17 January 2020

Table of contents

List of publications

Refereed Journal Papers

- **Nsamba, B.,** Campante, T. L., Monteiro, M. J. P. F. G., Cunha, M. S. et al. (2019). *Front. Astron. Space Sci. - Stellar and Solar Physics*, 6, 25. https://www.frontiersin.org/articles/10.3389/fspas.2019.00025/full

- Huber, Daniel, Chaplin, William J., Chontos, Ashley, Kjeldsen, Hans et al. (2019). *AJ*, 157, 6. https://ui.adsabs.harvard.edu/abs/2019AJ....157..245H

- Rendle, M. Ben., Buldgen, Gaël., Miglio, Andrea., Reese, Daniel., et al. (2019). *MNRAS*, 484, 771. http://adsabs.harvard.edu/abs/2019MNRAS.484..771R

- **Nsamba, B.,** Monteiro, M. J. P. F. G., Campante, T. L., Cunha M. S. et al. (2018). *MNRAS*, 479, L55. http://adsabs.harvard.edu/abs/2018MNRAS.479L..55N

- **Nsamba, B.,** Campante, T. L., Monteiro, M. J. P. F. G., Cunha, M. S. et al. (2018). *MNRAS*, 477, 5052. http://adsabs.harvard.edu/abs/2018MNRAS.477.5052N

Conference proceedings

- **Nsamba, B.,** Monteiro, M. J. P. F. G., Campante, T. L., Reese, D. R., et al. (2017). *EPJ Web of Conferences*, Volume 160, 05010. http://adsabs.harvard.edu/abs/2017EPJWC.16005010N

- **Nsamba, B.,** Campante, Tiago L., Monteiro, Mário J. P. F. G., Cunha, Margarida S., et al. (2018). arXiv: 1812.00431. DOI: 10.5281/zenodo.1468510. http://adsabs.harvard.edu/abs/2018arXiv181200431N

List of figures

List of tables

Chapter 1

Basic concepts in asteroseismology

In this chapter, the basic concepts in the asteroseismology (i.e., the study of the internal structure of stars through the interpretation of their oscillation spectra) of solar–type stars are introduced. A brief historical background to the detection of stellar variability/pulsations is first provided. The discussions are then directed towards highlighting the different mechanisms that drive stellar pulsations, with a focus on the stochastic excitation mechanism which powers pulsations in the stars explored in this thesis. This chapter is based on Kippenhahn and Weigert (1990), Bedding and Kjeldsen (2003), Aerts et al. (2010), Pols (2011), Chaplin et al. (2011), and Kippenhahn et al. (2012).

1.1 Historical account

It is imperative to introduce the concept of asteroseismology based on the famous lamentation made almost 100 years ago by Sir Arthur Eddington in his book, *The Internal Constitution of the Stars (Eddington, 1920)*:

> *"At first sight, it would seem that the deep interior of the Sun and stars is less accessible to scientific investigation than any other region of the universe. Our telescopes may probe farther and farther into the depths of space: but how can we ever obtain certain knowledge of that which is hidden behind substantial barriers? What appliance can pierce through the outer layers of a star and test the conditions within?"*

Using the knowledge of basic laws of physics, and from the observable boundary conditions at the surface of a star, the interior structure can be calculated. However, the need to validate these theoretical predictions with observations is a necessity if we are to trust such scientific inferences. There is no better way of penetrating

into stellar interiors than continuously observing their outer layers. Through such observations, many ancient amateur astronomers were able to notice variations in the stars' brightness over time. Some of these variations were observed to be regular, i.e., periodic, thus the term variable/pulsating stars.

Around 3200 years ago, ancient Egyptians documented the discovery of a variable star called "Algol", also known as the "Demon star". It is located in the constellation of Perseus (Porceddu et al., 2008). The left and right bottom panels of Fig. 1.1 show a periodogram and phase–folded light curve of Algol, respectively. Algol has a relatively stable brightness with periodic dips as shown in the right bottom panel of Fig. 1.1, with a period of $\sim$ 2.867 days. In 1596, David Fabricius (1564 - 1617), a German Lutheran pastor, discovered a variable star called Omicron Ceti (o Ceti), also known as Mira (Hoffleit, 1997). Omicron Ceti was later observed by Johannes Holwards (1618 - 1651) in 1638 and was discovered to pulsate in a regular eleven–month cycle. This was an important discovery that ended the belief held by ancient philosophers, like Aristotle, that stars were invariant. The right top panel of Fig. 1.1 demonstrates that Mira (o Ceti) has a constantly changing brightness unlike Algol (see right bottom panel of Fig. 1.1).

Between 1686 and 1704, a third variable star Chi Cygni was observed (e.g., Lo and Bechis 1977) and by 1796, eleven variable stars had been identified. With the advancement in photographic techniques since the 1850s, numerous variable stars have been observed and by 2007, over 46,000 variable stars in the Milky Way were listed in the general catalogue of variable stars (Samus et al., 2009). In the last Century, scientific efforts were geared towards understanding the cause of these periodic variations in stars. In this regard, variability in stars was categorised into two classes, i.e., stars whose brightness changes because of external factors such as being eclipsed by another star, planet or as a result of stellar rotation are called "Extrinsic variables", while stars whose absolute luminosity varies due to processes such as pulsations are referred to as "Intrinsic variables".

Cepheid variables were notably the most studied during the early times (i.e., 1910s). This is because of their large amplitude pulsations of $\sim \pm$ 1 mag. These also have a constantly changing brightness, with periods of $\sim$ 5.37 days. At Harvard College Observatory, an American astronomer, Henrietta Swan Leavitt (1868 - 1921), discovered and determined the magnitude of more than 2400 variable stars using photographic plates (Leavitt and Pickering, 1912). While analysing the variable stars discovered in the Small Magellanic Cloud (SMC), Leavitt noticed that Cepheid variables with long pulsation periods were intrinsically more luminous than the ones with short pulsation

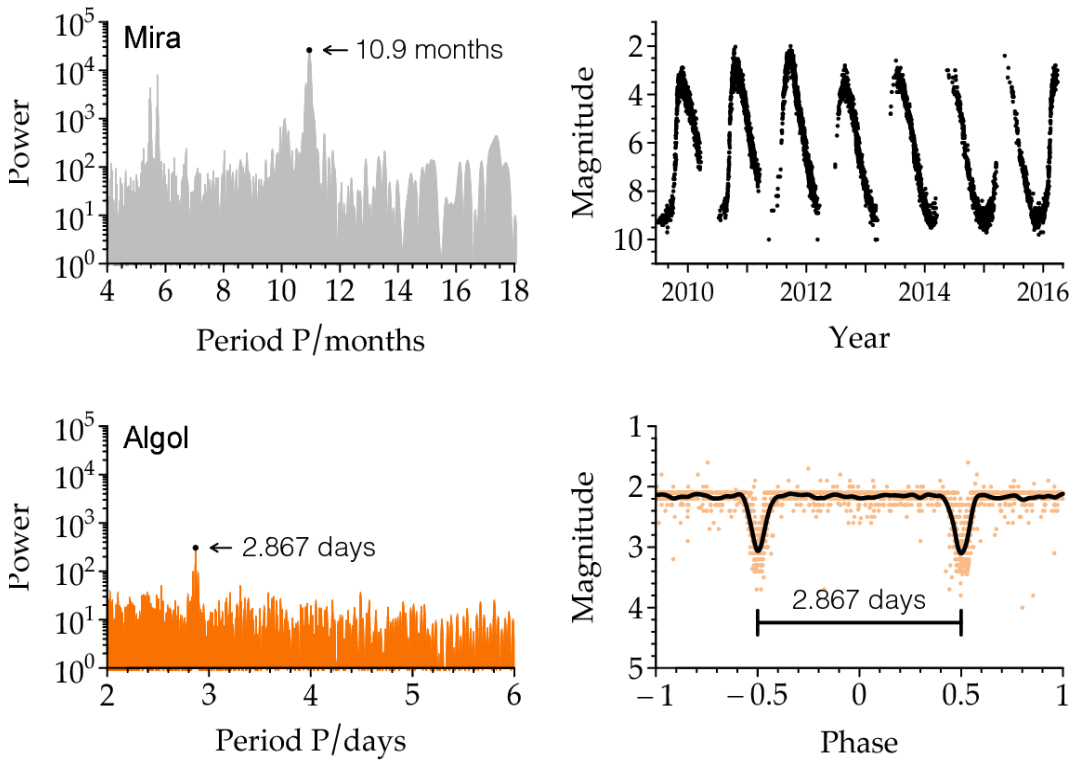

Figure 1.1: Periodograms and light curves for the first two discovered classes of periodic variable stars, i.e., Mira (top panel) and Algol (bottom panel). Credit to the American Association of Variable Star Observers for the data (Kafka and Waagen, 2017). Figure taken from Bellinger (2019).

periods (see left panel of Fig. 1.2). This led to the derivation of "a remarkable relation between the brightness of these variables and the length of their periods" (Leavitt and Pickering, 1912). This relation takes the form

$$\log P = q_0 + q_1 \log\left(\frac{L}{\mathrm{L}_\odot}\right) , \tag{1.1}$$

where q_0, q_1, are constants, $\mathrm{L}_\odot$ is the solar luminosity, and P is the period of the variation. The absolute luminosity of the star (L) can be derived following the expression

$$M_{\mathrm{bol}} - M_{\mathrm{bol},\odot} = -2.5 \log\left(\frac{L}{\mathrm{L}_\odot}\right) , \tag{1.2}$$

where the bolometric magnitude (i.e., a measure of the total radiation of a star emitted across all wavelengths of the electromagnetic spectrum) can be converted to the absolute

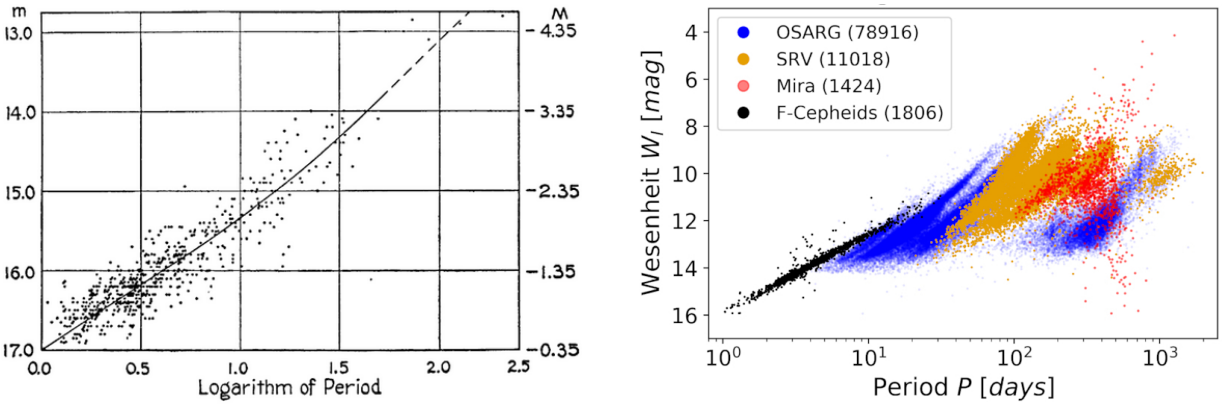

Figure 1.2: Overview of the period–luminosity relationship. Left panel shows the Classical Cepheids in the Small Magellanic Cloud, with the period in days. Figure taken from Shapley 1961. Right panel shows the modern Period–Wesenheit (P–W) relations for the different samples namely, fundamental Mode Cepheids (F–Ceph), Mira stars (Mira), semi–regular variables (SRV) and OGLE Small Amplitude Red Giant stars (OSARGs) in the Large Magellanic Cloud (LMC). The legend also indicates the number of stars in each sample. Figure taken from Rau et al. (2019).

magnitude[1], M_v, using

$$M_{\rm bol} = M_v + BC_v \ , \tag{1.3}$$

where BC_v is the bolometric correction (i.e., the quantity to be added to the absolute magnitude in a specific passband in the absence of interstellar extinction in order to account for the flux outside that band; Torres 2010) in the v band. Thus the period –luminosity relation takes the revised form

$$\log P = A_0 + A_1 M_v \ , \tag{1.4}$$

where A_0 and A_1 are constants. Once the period is known, M_v is derived from equation 1.4, and then the distance, d, can be obtained using

$$M_v = V_0 - 5\log\, d + 5 \ , \tag{1.5}$$

where V_0 is the observed magnitude of the star corrected for interstellar reddening. Hence Cepheid variables are distance indicators (e.g., Sandage 1999, Feast 1999, Storm 2006, Fiorentino et al. 2013). The right panel of Fig. 1.2 shows the modern P–W

[1]The absolute magnitude is the apparent magnitude a star would have if it were viewed from a distance of exactly 10 parsecs (32.6 light–years), with no extinction (or dimming) of its light due to absorption by interstellar dust particles. Apparent magnitude of a celestial object is the measure of its brightness as seen by an observer on Earth.

relationship for a number of long–period variable stars. It can been seen that the P–W relation for the Cepheids (shown as black dots in the right panel of Fig. 1.2) is consistent with the findings of Leavitt and Pickering (1912).

By the 1960s, efforts were directed towards understanding the mechanisms driving stars to pulsate. Attention was then focused on the nearest star to earth, i.e., the Sun. Claverie et al. (1979) are credited with having made the first detection of oscillation motions in the surface of the Sun. These pulsations were recorded to have periods of approximately five minutes (Leighton et al., 1962). And so the new science field of "Helioseismology" was born. It was devoted to exploring the solar interior based on the observation of oscillation waves on the Sun's surface. Currently this field of study has greatly improved our understanding of the solar interior, resulting in a detailed map of the Sun's internal rotation and structure. It has also highly contributed to the testing of the physical inputs (e.g., equation of state, opacities, chemical compositions, chemical transport processes) used to create stellar model interiors (e.g., Christensen-Dalsgaard et al. 1993a, Basu and Antia 1994, Bahcall et al. 1995, Richard et al. 1996, Thompson 2004, Chaplin et al. 2008, Basu and Antia 2008, Howe 2009, Basu 2018, Basu and Chaplin 2019). These findings based on the Sun gave insight on how one could "pierce through the outer layers of a star and test the conditions within". The quest to search for solar–like oscillations in other stars emerged. However, this gave birth to new challenges. For instance, other stars are farther away and therefore present observational challenges, and some stars are at different evolutionary states compared to Sun thus having different internal conditions. Interestingly, these challenges opened up an even more exciting adventure, i.e., a research field dedicated to studying the internal structure of stars through the interpretation of their oscillation spectra (e.g., Brown and Gilliland 1994, Kjeldsen and Bedding 1995, Heasley et al. 1996, Bedding et al. 2001). This is known as "Asteroseismology". This field of modern astronomy has enormously accelerated with the development of radial–velocity observation techniques and advancements in space exploration. At this point, it is important to stress that not all stars oscillate like the Sun. This is attributed to the fact that different stars have different mechanisms driving their pulsations.

1.2 Pulsation mechanisms

There are various mechanisms that drive pulsations in stars, however, it is essential to note that not all stars with a given characteristic pulsate. One may state that a star could appear constant yet may be pulsating with an amplitude below our detection

limit. Currently, the level of precision of observations in radial velocity and photometry is of the order of cm s^{-1} and μ mag, respectively. Therefore, at this level of precision, it can confidently be stated that some stars do not pulsate. During the pulsation process, the star contracts (heats) and expands (cools). The driving mechanism sustains the pulsation process by feeding energy into it during contraction which is then released during expansion.

1.2.1 κ mechanism

In 1914, an American astronomer, Harlow Shapley (1885 - 1972), proposed that stellar pulsations are mostly driven by stellar interior processes. To this end, based on the observation of Cepheid variables, Shapley suggested that the observed variations in brightness and temperature were caused by radial pulsations driven by resonating sound waves in the stellar interior, as initially suggested by Arthur Ritter in 1879 (see, Shapley 1914). More attention was given to Shapley's suggestion after Sir Arthur Eddington (1882 - 1944) proposed a model supporting radial pulsations. The major driver of pulsations in Eddington's model of stellar pulsation is the opacity in the stellar interior. The opacity at a given point is defined as the amount of absorption that a photon of a particular energy (wavelength) encounters at a particular point in the star. Opacity depends on the composition of the material, density, and temperature. In addition, it is also a function of the wavelength of the photon (Schwarzschild, 1965, Cox and Tabor, 1976).

The two most abundant elements in main–sequence stars are hydrogen (H) and helium (He). Regions with high composition gradients (e.g., the ionization zones of H and He) result into high opacity, which blocks radiation transfer, heats the gas, leading to the increase in pressure, thus causing the star to expand beyond its equilibrium point. The heating of the gas causes ionization which reduces the opacity, this increases the efficiency of energy transport and the gas cools, thus the star contracts and the process repeats itself. This pulsation mechanism is known as "κ mechanism". This process is also commonly related to the heat–engine mechanism which involves converting thermal energy into mechanical energy (e.g., de Boer and Seggewiss 2008, Maeder 2009). To highlight the relation with the thermodynamic heat–engine, one considers the stellar envelope to act as the heat engine, with the contracting and expanding envelope as the piston, radiation taking the part of the steam, and the opacity of the stellar layers representing the valve. The time it takes sound waves to travel across the

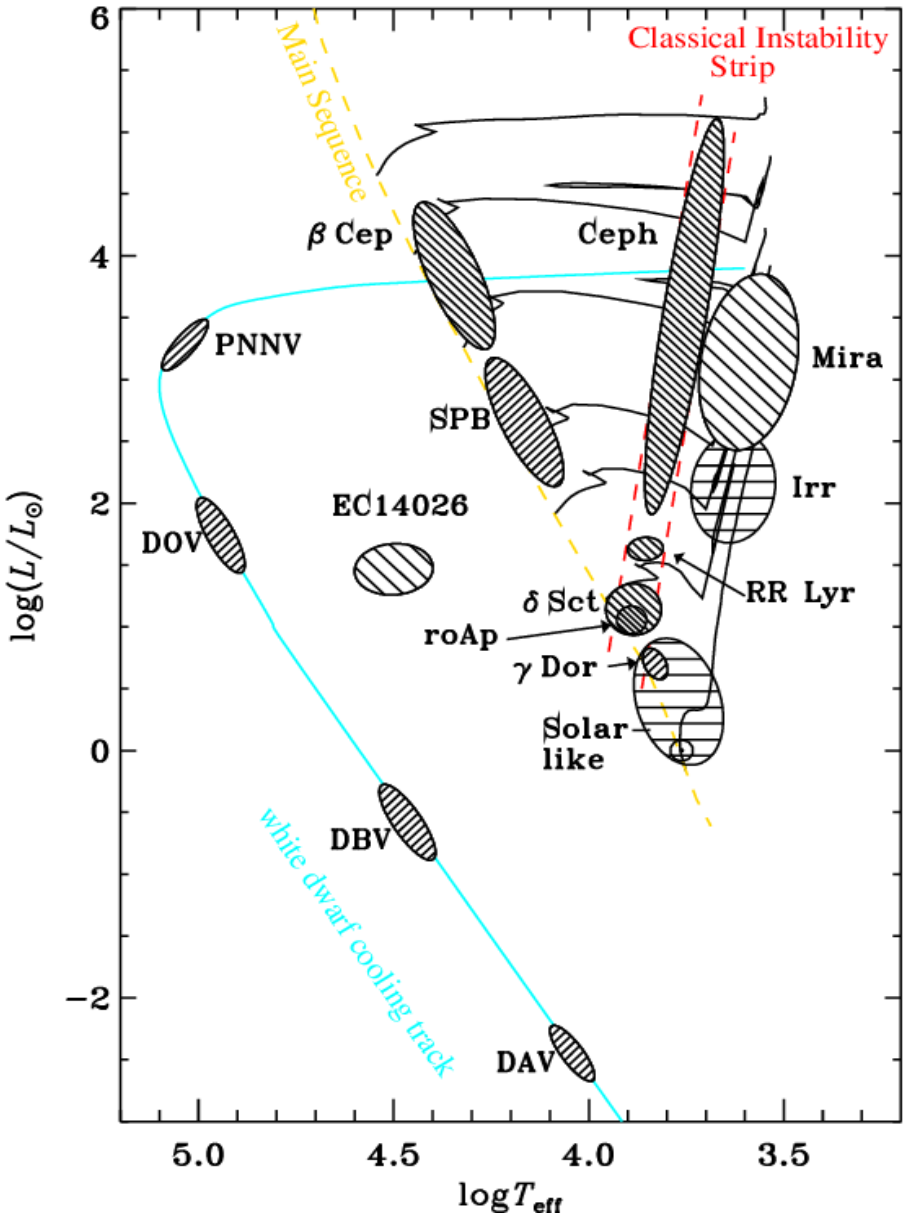

Figure 1.3: Location of various types of pulsating stars in the Hertzsprung–Russell diagram. The parallel red long–dashed lines indicate the Cepheid instability strip, the solid black lines represent evolutionary tracks, the dashed yellow line indicates the zero–age main sequence (ZAMS), the light blue line represents the white dwarf cooling evolution track. $T_{\rm eff}$ is the stellar effective temperature and L is the stellar luminosity. For the acronyms: rapidly oscillating Ap (roAp); Slowly Pulsating B (SPB); subdwarf B variables (sdBV) such as EC 14026; Planetary Nebulae Nuclei Variables (PNNV). The DBV and DAV stars are variable DB (helium–rich) and DA(hydrogen–rich) white dwarfs. Figure taken from Aerts et al. (2010).

stellar diameter, i.e., the pulsation period, Π, is given as

$$\Pi = \frac{2R}{\nu_{\rm s}} \backsimeq \sqrt{\frac{3\pi}{2\gamma G\rho}}\,, \tag{1.6}$$

where R is the stellar radius, G is the gravitational constant, γ is the ratio of the specific heats for the stellar material, i.e., $\gamma \sim 5/3$ for a monatomic gas, and ρ is the stellar density. Equation 1.6 shows that the pulsation period is inversely proportional to the square root of the stellar mean density. The κ mechanism is known to drive pulsations in the Cepheid variables, δ Sct stars, RR Lyrae stars, β Cep stars (see Fig. 1.3 for the position of these stars in a Hertzsprung–Russell diagram). Interestingly, in β Cep stars, the κ mechanism has been found to have opacity features related to iron (Fe) and not on H or He (e.g., Dziembowski and Pamiatnykh 1993). The same mechanism has been found to occur in EC 14026 (sdBV) stars shown in Fig. 1.3. The classical instability strip shown in Fig. 1.3 occupies a narrow region, this being mainly attributed to the location of the partial ionization zones which depends on the stellar temperature. Stars above the instability strip have effective temperatures $\gtrsim$ 7500 K and their ionization zones are located too close to the star's surface — have insufficient mass to efficiently power stellar pulsations. Stars below the instability strip have effective temperature $\lesssim$ 5500 K, their ionization zones are located deep in the stellar interior and, in addition, energy transport is dominated by convection. Hence the narrow temperature range occupied by the instability strip corresponds to stellar temperature ranges with partial ionization zones capable of driving stellar pulsations.

1.2.2 Stochastic excitation

The κ mechanism cannot occur in the Sun and solar–type oscillators. This is because it depends on the opacity in the ionization zones as described in Sect. 1.2.1. These zones exist in the convective envelopes of solar–type stars, yet the κ mechanism is only effective in regions where heat is transported by radiation.

Stars whose masses are $\lesssim 2\ {\rm M}_{\odot}$ possess an upper convective zone in which pulsations are excited and damped by turbulent convection. The turbulent motions generate acoustic waves that drive resonant modes of the stellar cavity (Stein, 1967, Goldreich and Keeley, 1977, Stein and Nordlund, 1991, Houdek et al., 1999, Samadi and Goupil, 2001, Stein et al., 2004, Houdek, 2006). The acoustic modes in the Sun and solar–type stars are usually of a period of a few minutes in the range of 3 –15 minutes. The amplitudes of the oscillations excited by turbulent convection depend on the efficiency of the excitation and damping processes in the convective zone. Stellar oscillations

driven in this way have been confirmed through development of theoretical models that mimic stochastic excitation in the convective envelope of solar–type stars (e.g., Goldreich and Keeley 1977, Goldreich et al. 1994, Samadi and Goupil 2001, Samadi et al. 2007, and references therein). In addition, 3D numerical hydrodynamical simulations have been employed to compute the rate at which pressure modes are excited (e.g., Stein and Nordlund 2001).

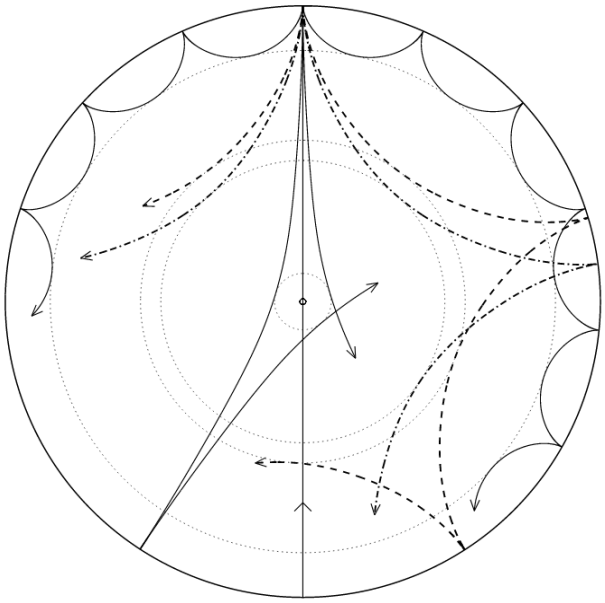

Figure 1.4: Schematic cross–section of a Sun–like star showing the propagation of acoustic waves. The rays shown illustrate modes of the same frequency but decreasing spherical degree, l. Modes with lower l penetrate deeper in the star. The vertical line passing through the centre demonstrates the behaviour of a radial mode. Dotted curves: the sound speed increases with depth causing bending of waves until they reach a depth where they undergo total internal reflection. Figure taken from Aerts et al. (2010).

In the upper convective zone of solar–type stars, oscillations are driven by pressure (p modes; illustrated in Fig. 1.4). Therefore, the p modes are very sensitive to the conditions in the outer part of the star. Figure 1.4 shows propagating acoustic waves being reflected at the stellar photosphere and refracted at particular layers in the stellar interior. This is because sound speed increases with depth (see Fig. 1.5) causing waves to be refracted towards the surface, while the rapid decrease in density causes waves to reflect off the stellar photosphere. The frequencies for the p modes are approximately described by the asymptotic relation, given by (Ulrich, 1970, Aerts et al., 2010):

$$\nu_{n,l} = \Delta\nu \left(n + \frac{1}{2} l + K \right) + \epsilon_{n,l} \ , \tag{1.7}$$

where n is the radial order, l is the angular degree, K is a constant sensitive to the surface layers, and $\epsilon_{n,l}$ is a correction defined as

$$\epsilon_{n,l} = -l(l+1) D_0 \ , \tag{1.8}$$

where, D_0 is sensitive to the sound speed near the core. $\Delta\nu$ is the large frequency separation defined as the distance between modes of the same degree, l, and consecutive radial order, n. $\Delta\nu$ may also be defined as the inverse sound travel time across the stellar acoustic diameter. This can be expressed as (Ulrich, 1970, Aerts et al., 2010):

$$\Delta\nu = \left(2 \int_0^R \frac{dr}{c(r)} \right)^{-1} \ , \tag{1.9}$$

where $c(r)$ is the sound speed across the acoustic diameter. The large separation is sensitive to the radius of the star and is proportional to its mean density (Ulrich, 1970, Kjeldsen and Bedding, 1995), i.e.,

$$\Delta\nu \propto \sqrt{\overline{\rho}} \ , \tag{1.10}$$

where $\overline{\rho} \propto (M/R^3)$. M and R are the stellar mass and radius, respectively.

In equation 1.7 and equation 1.8, D_0 is defined in terms of the small frequency separation as

$$D_0 = \frac{1}{6} \delta\nu_{0,2} \ . \tag{1.11}$$

The small separation is given as (Aerts et al., 2010):

$$\delta\nu_{n,l} = -(4l+6) \frac{\Delta\nu}{4\pi^2 \nu_{n,l}} \int_0^R \frac{dc}{dr} \frac{dr}{r} \ . \tag{1.12}$$

The integral component of equation 1.12 demonstrates that $\delta\nu_{n,l}$ is sensitive to the sound speed gradient (dc/dr) in the stellar interior, which depends on the chemical composition profile during stellar evolution. For instance, for a main–sequence solar–type star, nuclear burning results into reduction in the central hydrogen, while helium accumulates in the stellar core — increase in the mean molecular weight. This can be demonstrated following the expression of the speed of sound of the acoustic

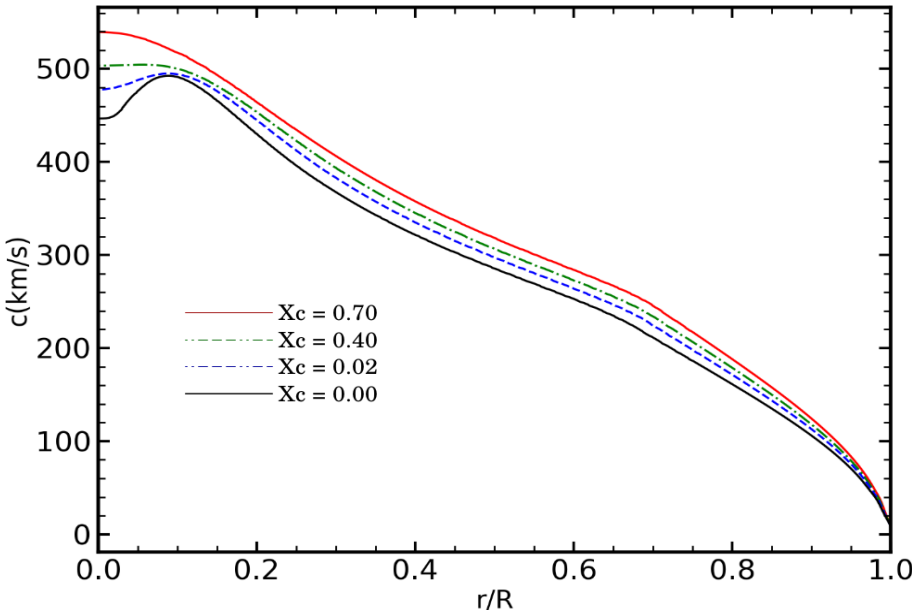

Figure 1.5: Sound speed profiles of different models along the main sequence phase expressed as a function of the model fractional radii. Xc is the central hydrogen mass fraction. The models were constructed with the same physics as described in Nsamba et al. (2017) and have a mass of 1.0 $M_{\odot}$, initial metal mass fraction of 0.018, and mixing length parameter for the description of convection of 1.8.

waves given as

$$c = \sqrt{\frac{\Gamma_1 p}{\rho}} \, , \tag{1.13}$$

where Γ_1 is an adiabatic exponent, p is the pressure, and ρ is the mean density. Substituting p/ρ with the expression below considered for a real gas

$$\frac{p}{\rho} = \frac{QT}{\mu} \, , \tag{1.14}$$

where T is the temperature of the gas, Q is a constant, and μ is the mean molecular weight, equation 1.13 becomes

$$c \propto \sqrt{T/\mu} \, . \tag{1.15}$$

Therefore, if the temperature in the stellar core is relatively constant, the sound speed in the core decreases when μ increases (see Fig. 1.5) — $\delta\nu$ in equation 1.12 decreases as the star evolves. In addition, this also demonstrates that the small separation is very sensitive to the amount of central hydrogen mass fraction, hence stellar age.

It is essential to note that stars oscillate in a variety of modes, the simplest of which being the ones in which the star maintains its spherical symmetry. The latter

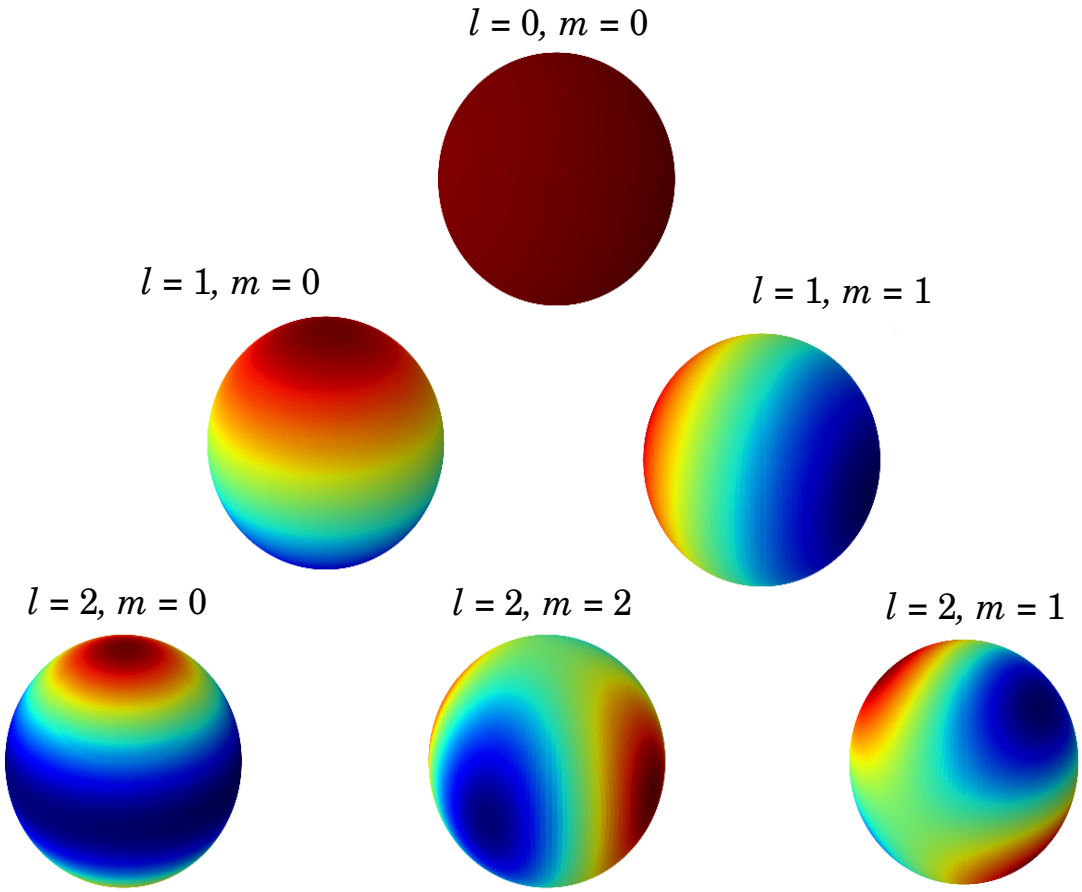

Figure 1.6: A snapshot of the surface distortions generated by pulsation modes in the range $0 \leq l \leq 2$. Areas of a star moving outwards are coloured in blue while the red–coloured areas move inwards. Figure taken from Verma (2016).

are referred to as radial modes. Stellar oscillations that change the shape of a star, i.e., cause deviations from spherical symmetry, are known as nonradial modes. Any arbitrary deviations from a sphere can be described by functions known as spherical harmonics given as:

$$Y_l^m(\theta,\phi) = (-1)^m N_l^m P_l^m \cos(\theta) \exp(im\phi) \ , \tag{1.16}$$

where N_l^m is a normalisation constant expressed as:

$$N_l^{m2} = \frac{(2l+1)(l-m)!}{4\pi(l+m)!} \ , \tag{1.17}$$

where ϕ is the longitude, θ is the angle from the polar axis (co–latitude), P_l^m is the associated Legrendre polynomial given as

$$P_l^m(\cos\,\theta) = \frac{1}{2^l l!}(1-\cos^2\theta)^{m/2}\frac{\mathrm{d}^{l+m}}{\mathrm{d}\,\cos^{l+m}\,\theta}(\cos^2\theta-1)^l\ , \tag{1.18}$$

l is the spherical harmonic degree which describes the total number of nodes on the sphere, m is the azimuthal order which describes the nodes along the longitude lines, and takes values in the range $-l \leq m \leq +l$, and n is the number of nodes in the radial direction (e.g., Takata 2005). Figure 1.6 shows a schematic physical representation of spherical harmonics of a star oscillating with a given value of l and m. Extensive details on the pulsation modes and frequencies are given in Sect. 2.2.

A variety of both ground–based and space missions have been able to observe stars with solar–like oscillations, for instance, the GOLF instrument (Global Oscillation Low Frequencies; Gabriel et al. 1997, Gelly et al. 2002) aboard the SoHO space craft (Solar and Heliospheric Observatory) dedicated to the observation of the Sun, the French–led CoRoT (Convection, Rotation, and planetary Transits; Baglin et al. 2006), NASA's *Kepler* space telescope (Borucki et al., 2010), and the recently launched NASA's TESS (Transiting Exoplanet Survey Satellite; Ricker et al. 2015). Solar–like oscillations are also expected to be observed by the future ESA's PLATO (PLAnetary Transits and Oscillations of stars; Rauer et al. 2014) mission. Apart from photometric observations, solar–like oscillations are also detectable through spectroscopic observations since they cause stellar surface variations yielding doppler shifts of the absorption lines in the stellar spectrum (e.g., Beck et al. 2015). The precision of seismic data is essential for inferring highly precise stellar parameters such as; radius and mass. For this to be achieved when ground–based observations are employed, uninterrupted continuous observations are required, which can only be attained through setting up a network of ground–based telescopes. Examples of such networks dedicated to the observation of the Sun include BiSON (Birmingham Solar Oscillations Network; Chaplin et al. 1996); and GONG (Global oscillation Network Group; Harvey et al. 1996). A network of ground–based telescopes have also been dedicated to observing other stars, for instance, de Meulenaer et al. (2010) analysed seismic data of α Centauri A obtained using a group of telescopes in Chile and Australia, namely, with the CORALIE fiber–fed échelle spectrograph, mounted on the 12–metre Euler Swiss telescope at ESO La Silla Observatory (Bouchy and Carrier, 2002), the University College London Echelle Spectrograph (UCLES) at the 3.9–metre Anglo–Australian Telescope (AAT) at Siding

Spring Observatory in Australia (Butler et al., 1996), and the UV–Visual Echelle Spectrograph (UVES) on the Very Large Telescope (VLT) in Chile.

1.2.3 Other mechanisms

Other proposed stellar pulsation driving mechanisms are briefly highlighted below:

— The ϵ mechanism is believed to be caused by global oscillations that are driven by the variations in the energy generation rate in the core of the star (e.g., Rosseland and Randers 1938, Cox and Smith 1981, Aerts et al. 2010). It is believed that this mechanism occurs in very massive evolved stars but no cases of any pulsating stars have been reported to have oscillations facilitated by only the ϵ mechanism.

— A pulsation mechanism similar to the κ mechanism described in Sect. 1.2.1 is convective blocking/driving. This involves radiation flux from the stellar interior being blocked at the base of a convective zone for some time during compression and released during the expansion phase. Examples of stars with pulsations thought to be partly driven in this way not only include white dwarfs like DA and DB (see Fig. 1.3) but also γ Doradus (Xiong and Deng, 2007, Guzik et al., 2000, Balona, 2010, 2018).

1.3 Pulsation time scales

It is important to understand the properties of stellar oscillations in order to comprehend their origin and nature. To achieve this, it is essential to explore the different time scales of stellar oscillations. When the pressure gradients and gravitational forces holding the star in hydrostatic equilibrium are suddenly disrupted by some dynamical process, the time it takes the star to recover its equilibrium state is given by the dynamical time scale ($\tau_{\rm dyn}$) defined as:

$$\tau_{\rm dyn} = \frac{\text{Characteristic radius } (R)}{\text{Characteristic Velocity } (V_{\rm esc})} \ , \tag{1.19}$$

$$\tau_{\rm dyn} = \left(\frac{R^3}{2GM}\right)^{-1/2} \ , \tag{1.20}$$

where G is the gravitational constant and M is the stellar mass. I note that the characteristic velocity (or escape velocity) in equation 1.20 is given by

$$V_{\rm esc} = \left(\frac{2GM}{R}\right) \ . \tag{1.21}$$

If $\overline{\rho}$ is the mean density of the star, equation 1.20 can be expressed as

$$\tau_{\rm dyn} = \frac{1}{\sqrt{G\overline{\rho}}} \ . \tag{1.22}$$

In general, $\tau_{\rm dyn}$ is indicative of the pulsation period. From equation 1.22, once the pulsation period is known, the mean density of the star can be estimated. Furthermore, in the Sun and Sun–like oscillators, pressure modes cause them to deviate from their equilibrium state as described in Sect. 1.2.2.

Depending on the evolutionary state of a star, the time it takes to exhaust its nuclear fuel when nuclear fusion is its main energy generation source is referred to as the nuclear time scale ($\tau_{\rm nuc}$). This is expressed as

$$\tau_{\rm nuc} = \frac{XqMc^2}{L} \ , \tag{1.23}$$

where L is the stellar luminosity, q is the fraction of fuel (or stellar mass) in the stellar core available to take part in nuclear burning, X is the mass fraction to be converted into energy during nuclear fusion (in case of hydrogen burning, and $X \simeq 0.7$). For the case of the Sun, one estimates a total nuclear time scale of approximately 10 billion years.

When nuclear reactions stop at any stage of stellar evolution, the time needed for a star to radiate all its thermal energy is defined as the thermal time scale (or Kelvin–Helmholtz time scale, $\tau_{\rm KH}$). This is expressed as

$$\tau_{\rm KH} = \frac{U}{L} \ , \tag{1.24}$$

where the thermal energy (U) is approximately equal to the gravitational energy. Equation 1.24 can be re–written as

$$\tau_{\rm KH} = \frac{< c_{\rm p} T_{\rm eff} > M}{L} \ , \tag{1.25}$$

where $c_{\rm p}$ is the heat capacity of a gas at constant pressure and $T_{\rm eff}$ is the effective temperature. $\tau_{\rm KH}$ is a vital time scale which can be used to estimate the time needed for a star to contract before it ignites nuclear fusion and hence can be used to estimate the pre–main sequence life time.

Chapter 2

Theory of stellar structure and stellar pulsations

It is essential to note here that only solar–type stars in the mass range [0.7 – 1.25] $M_{\odot}$ are studied in this thesis, i.e., mostly main–sequence and a few subgiant stars. In a nutshell, stars on the main–sequence phase spend most of their life time converting core hydrogen to helium and energy being given off as a bi–product of the nuclear reaction. Once the core hydrogen in main–sequence stars is completely depleted, hydrogen shell burning is ignited. The star now starts its evolution on the "subgiant stage". Figure 2.1 shows a modern H–R diagram generated using *Gaia* DR2 data (Gaia Collaboration et al., 2016), with several stellar evolution stages clearly visible. For a detailed review of all the different stages of stellar evolution, i.e., from birth to the giant phases, refer to Kippenhahn and Weigert (1990), Hilditch (1992), Prialnik (2009), Kippenhahn et al. (2012), Nsamba et al. (2014) and MacDonald (2015).

In this chapter, attention is directed towards the description of the equations governing stellar structure while highlighting the assumptions made during stellar model construction. I also state the shortcomings arising from these assumptions so as to showcase the imperfections involved in stellar modelling routines. In addition, I highlight how the one–dimensional stellar evolution code MESA (Modules for Experiments in Stellar Astrophysics) used in this thesis finds solutions to the equations of stellar structure. This chapter closes with the description of the theory of stellar oscillations with emphasis on model adiabatic oscillation frequencies adopted in the optimisation procedures as seismic constraints. I note that no discussions are presented regarding the analysis and interpretation of asteroseismic data. Please refer to Campante (2012) and references therein for a thorough discussion. This chapter is based on Cox (1980), Unno et al. (1989), Prialnik (2000), Christensen-Dalsgaard (2002), Hansen et al. (2004),

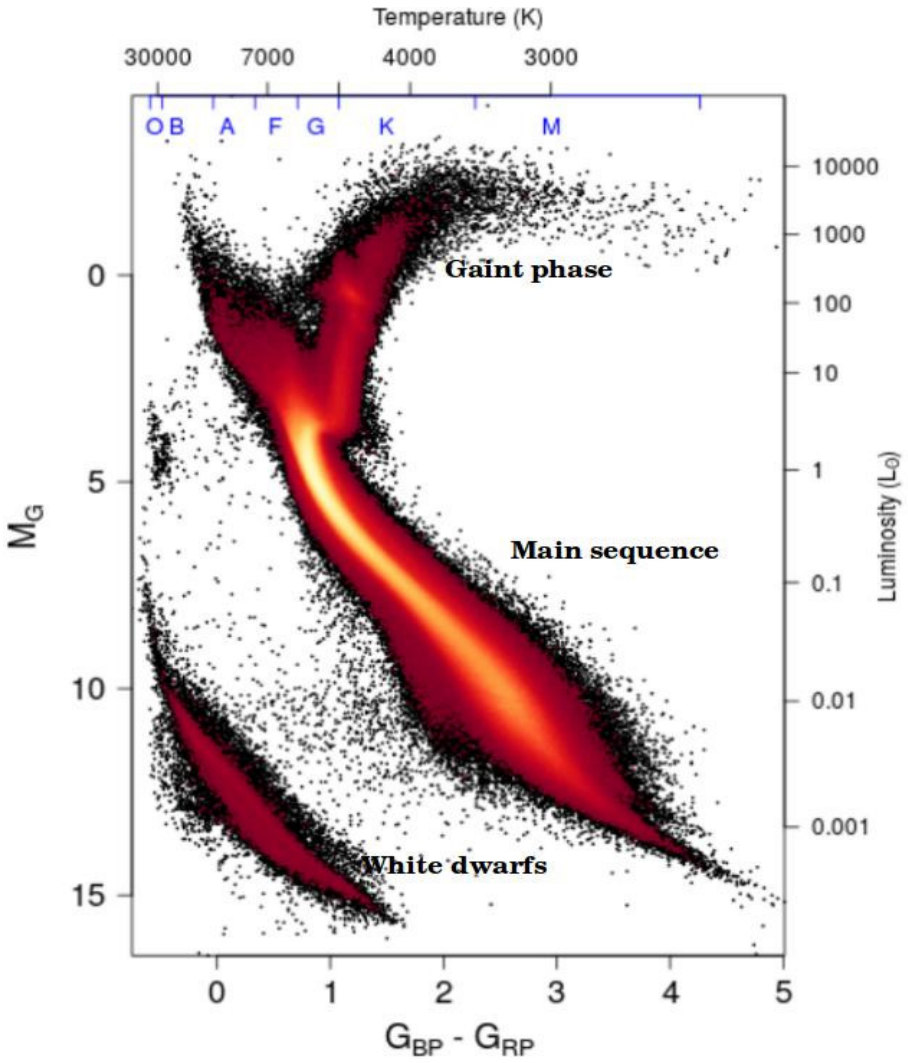

Figure 2.1: H–R diagram compiled using Gaia DR2 data. The effective temperature and luminosity for main–sequence stars are indicated at the top and on the right axis, respectively. The colour code denotes density of stars (Gaia Collaboration et al., 2016). The bottom x–axis shows the Gaia DR2 photometric colour. The left y–axis shows the G magnitude. Figure taken from Gaia Collaboration et al. (2016).

Aerts et al. (2010), Pols (2011), Paxton et al. (2011, 2013, 2015), Kippenhahn et al. (2012), Townsend and Teitler (2013), and Di Mauro (2016).

2.1 Stellar structure

The crucial need to understand the observed stellar properties led to the exploration of the underlying physical processes taking place in deep stellar interiors. The basic

theory enabling the description of the structure and evolution of stars is based on several assumptions which aid in the formulation of the stellar structure equations. It is assumed that the star is:

(1) A fluid: This assumption allows one to make use of the equation of fluid dynamics when describing stars (Collins, 1989). It is successful in describing the deep stellar interiors but fails beyond the stellar photosphere since different particle species separate above this region.

(2) Self–gravitating: This assumes gravity as the only important external force in the fluid equations, thus allows one to ignore electric and magnetic fields. In practice, for instance for the Sun and stars with convective cores, there is strong evidence for existence of a magnetic field in such stars. However, I neglected their effects because their impact on the stellar structure may not be significant.

(3) Spherically symmetric: This allows for the description of the stellar structure using only a radial coordinate or any other quantity such as mass or pressure. In addition, any mechanism which can distort the star and also create additional mixing due to fluid instabilities such as rotation is ignored. Despite the fact that stars do rotate, the rotation may be so slow that its impact on the stellar structure is negligible, e.g., the Sun. I note that, for all the target stars considered in this thesis, the effects of stellar rotation are ignored.

(4) Stable on dynamical timescales: This sets the possibility of neglecting net velocities and accelerations in the star. This thesis is based on stellar pulsations that arise due to variations in the dynamical stability of the star, although stellar evolution timescales occur on a timescale much longer than the dynamical timescale.

(5) Single isolated objects: In this thesis, I ignore all the effects of stellar companionship such as mass transfer and tidal interactions.

(6) Stable stellar mass: Since this thesis explores mainly main–sequence stars, and considers item (5) above, I therefore assume that stars do not vary their stellar mass. However, I note that stars in more evolved stages such as red giants may undergo mass loss, e.g., Miglio et al. (2012).

Taking all the above assumptions into consideration, I define the fundamental equations governing stellar structure, while relating these equations to how the stellar evolution code (MESA; Paxton et al. 2011, 2013, 2015) employed in this thesis handles them.

MESA is a one–dimensional stellar evolution code with various modules designed to handle a number of stellar physics applications. Each module is designed to handle specific aspects of stellar physics, such as: nuclear reactions, atmosphere, equation of state, and atomic diffusion among others; while other modules handle the numerical components, such as: interpolation data sets, matrix operations etc. During the research work in this thesis, I intensively employ a module "star" which calls other relevant modules during stellar simulations. It is worth noting that MESA is an open source code written in the FORTRAN programming language, open for contributions and scrutiny from the astrophysics community — making MESA a powerful tool for stellar astrophysics.

The solutions to the set of equations of stellar structure described in Sects. 2.1.1, 2.1.2, and 2.1.3 can not be found analytically because they are non–linear differential

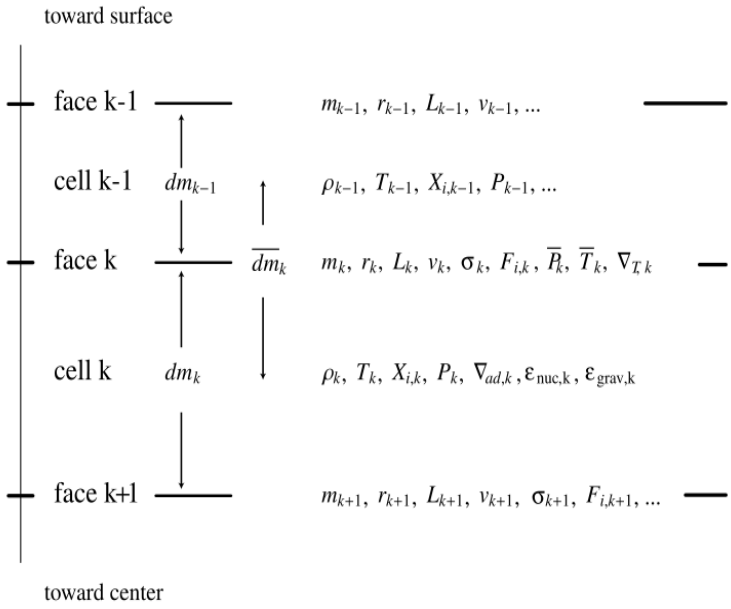

Figure 2.2: Illustration of the cell division according to the MESA "star" module. The cells $k-1$, k, and a few corresponding cell parameters are indicated. The boundary cell k variables include density, ρ_k, temperature, T_k, mass fraction, $X_{i,k}$, etc. Between the different cells, examples of variables that are mass–averaged are shown. Figure taken from Paxton et al. (2011).

equations, thus numerical approaches offer the answer. The MESA module "star" is designed and implemented based on a Henyey–like code (e.g., Kippenhahn et al. 2012) with analytic Jacobians, automatic mesh refinement, and adaptive time–step control to yield solutions to the equations of stellar structure. MESA solves the differential equations describing stellar structure by first establishing the number of grid points

describing the cell boundaries and evaluates the finite differences between adjacent cell points (see Fig. 2.2). Figure 2.2 shows a schematic illustration of the cell division. I note that the cells are normally numbered from 1 at the surface to a maximum value in the center, which MESA determines depending on the criteria defined by the user. Care has to be taken when defining the number of model cells because this can sufficiently affect the results (i.e., model parameters). For instance, if the core is under–resolved, the central temperature is derived as the mean of the large region in the core, and this may yield a temperature value which is not sufficient enough to trigger nuclear fusion of particular chemical elements. *In my modelling routines, I found* $\sim$ *2000 model cells to be sufficient in yielding consistent results.* I note that one has to strike a balance so that models generated from MESA do not have too many cells thus increasing the model computation time, and not too few cells resulting in low accuracy.

At the innermost cell (i.e., related to the center of the star), the cell parameters such as luminosity, radius, and velocity are equal to zero, yielding the central boundary conditions. It is worth noting that MESA reformulates the equations describing stellar structure by adopting the mass, m, of the outermost boundary of the cell as an independent variable. I have therefore expressed the equations of stellar structure as a function of m rather than the radius, r. This is because the stellar radius undergoes significant changes during stellar evolution. Since I do not consider any mass loss or accretion when modelling the stars studied in this thesis, it is sufficient to use m as an independent variable. Refer to Paxton et al. (2011) for details on cases when model mass variations are considered. Another vital component of stellar evolution regards defining the "timestep" between evolution models. This is defined as the amount of time required to elapse so as to allow the computation of time–derivatives (e.g., Paxton et al. 2011, Renzo 2014). The timestep should also be set with care because it should be able to facilitate for sufficient model evolution in a reasonable time. I mostly determine this parameter in my model computations based on the rate of change in the central hydrogen abundance ($X_{\rm c}$). I found this to be sufficient for the stars studied in this thesis, this being mainly because they are mostly main–sequence stars and $X_{\rm c}$ is in such case an efficient indicator of their evolution. There are other additional controls available in MESA which one can use to control the timestep, such as; maximum change in effective temperature, maximum change in central density, maximum change in surface luminosity, maximum change in age, etc.

The following sections highlight the equations governing stellar structure. I relate these equations to how they are reformulated in MESA during their implementation with the aim of minimising the round–off errors and improving the numerical stability

(Paxton et al., 2011). I note that no extensive details on the derivation of these are given because this is only intended to aid the reader understand the essential properties of stellar evolution.

2.1.1 Mass conservation

Considering a shell containing a mass, dm, at a radius, r, with a thickness/width, dr, and having a local density, $\rho(r)$, the mass $m(r)$ of the shell is defined as

$$m(r) = \int_0^r 4\pi r^2 \rho \mathrm{d}r \ . \tag{2.1}$$

Differentiating the equation gives

$$\frac{\mathrm{d}m}{\mathrm{d}r} = 4\pi r^2 \rho \ . \tag{2.2}$$

Expressing equation 2.2 in terms of dm becomes

$$\frac{\mathrm{d}r}{\mathrm{d}m} = \frac{1}{4\pi r^2 \rho} \ . \tag{2.3}$$

This is the *first stellar structure equation*. Relating this equation to its implementation in MESA, one has to consider a cell, for instance cell k shown in Fig. 2.2. The density (ρ_k) of cell k evolves following the expression

$$\rho_k = \frac{\mathrm{d}m_k}{(4/3)\pi(r_k^3 - r_{k+1}^3)} \ , \tag{2.4}$$

where m_k and r_k are the mass and radius of cell k, respectively. r_{k+1} is the radius of cell $k+1$. Rearranging equation 2.4 and taking the natural logarithm, the mass conservation equation or continuity equation is expressed as

$$\ln(r_k) = \frac{1}{3}\ln\left[r_{k+1}^3 + \frac{3}{4\pi}\frac{\mathrm{d}m_k}{\rho_k}\right] \ . \tag{2.5}$$

2.1.2 Momentum conservation

Based on the assumption that stars do not vary on a dynamical scale, this requires an equilibrium state between the gravitational force and pressure force to be attained. This state of balance is called hydrostatic equilibrium. Consider a parcel of gas of cylindrical form at a distance, r, with a thickness, dr, having a surface area, dS, and

mass, dm. The force responsible for the downward motion is gravity. This is given as

$$F_{\rm g} = -g{\rm d}m \ , \tag{2.6}$$

where g is the gravitational acceleration at a distance, r, and is defined as

$$g = \frac{Gm}{r^2} \ , \tag{2.7}$$

where G is the gravitational constant. Thus equation 2.6 becomes

$$F_{\rm g} = -\frac{Gm}{r^2}{\rm d}m \ . \tag{2.8}$$

The net force on the element arising due to differences in pressure at a distance r and $r + {\rm d}r$ is given by

$$F_{\rm p} = P(r){\rm dS} - P(r + {\rm d}r){\rm dS} \ , \tag{2.9}$$

where $P(r){\rm dS}$ is the force acting at a distance r, and $P(r + {\rm d}r){\rm dS}$ is the force at $r + {\rm d}r$. Equation 2.9 simplifies to

$$F_{\rm p} = -\frac{{\rm d}P}{{\rm d}r}{\rm d}r{\rm dS} \ , \tag{2.10}$$

where the mass element, ${\rm d}m = \rho {\rm d}r{\rm dS}$. Following Newton's second law of motion, the resultant force, F, acting on the gas element is given as

$$F = F_{\rm g} + F_{\rm p} \ , \tag{2.11}$$

$$F = -\frac{Gm}{r^2}{\rm d}m - \frac{{\rm d}P}{{\rm d}r}{\rm d}r{\rm dS} \ . \tag{2.12}$$

For hydrostatic equilibrium to hold, the net force, $F = 0$,

$$0 = -\frac{Gm\rho {\rm d}r{\rm dS}}{r^2} - \frac{{\rm d}P}{{\rm d}r}{\rm d}r{\rm dS} \ , \tag{2.13}$$

$$\frac{{\rm d}P}{{\rm d}r} = -\frac{Gm}{r^2}\rho \ . \tag{2.14}$$

Taking mass as the dependent variable gives

$$\frac{{\rm d}P}{{\rm d}m} = -\frac{Gm}{4\pi r^4} \ . \tag{2.15}$$

This is the *second stellar structure equation*. Taking cell k as a reference (see Fig. 2.2), the hydrostatic equilibrium equation in MESA is expressed as

$$\frac{P_{k-1} - P_k}{0.5(\mathrm{d}m_{k-1} - \mathrm{d}m_k)} = \left[\left(\frac{\mathrm{d}P}{\mathrm{d}m}\right)_{\text{hydrostatic at } k} + \left(\frac{\mathrm{d}P}{\mathrm{d}m}\right)_{\text{dynamic at } k}\right] , \tag{2.16}$$

$$\frac{P_{k-1} - P_k}{0.5(\mathrm{d}m_{k-1} - \mathrm{d}m_k)} = -\frac{Gm_k}{4\pi r_k^4} - \frac{a_k}{4\pi r_k^2} , \tag{2.17}$$

where P_k is the pressure at cell k, and a_k is the Lagrangian acceleration defined as

$$a_k \backsimeq \frac{\mathrm{d}\nu_k}{\mathrm{d}t} , \quad \text{and} \quad \nu_k \backsimeq r_k \frac{\mathrm{dln}(r_k)}{\mathrm{d}t} , \tag{2.18}$$

where ν_k is the velocity of the cell k. The hydrodynamical component (i.e., second term of equation 2.17) is usually very small and may be set to zero if not used.

2.1.3 Energy conservation

This involves a balance between the energy generated in the stellar interior and the energy lost. For the main–sequence stars considered in this thesis, most of the heat is generated through nuclear energy. I denote the rate at which nuclear energy is generated per unit mass, per second as ϵ_{nuc}. Energy is also absorbed and released through expansion and contraction, respectively. This is attributed to gravitational energy, ϵ_{g}, expressed as

$$\epsilon_{\text{g}} = -T\frac{\partial S}{\partial t} , \tag{2.19}$$

where S is the specific entropy of the gas and T is the local temperature. In practice, my computations of ϵ_{g} involve use of an equation of state which is specified externally. Furthermore, some energetic neutrinos that escape any kind of interactions in the deep stellar structure are given off into space and thus heat is lost. The rate at which neutrinos take away energy from the star per unit mass is denoted as ϵ_{ν}. In practice, different prescriptions can be used to specify the neutrino energy loss rates, e.g., according to Itoh et al. (1996).

Consider the rate at which energy flows in and out of the shell of radius, r, and the local luminosity, l. Then

$$l = 4\pi r^2 F , \tag{2.20}$$

where F is the radial energy flux. The *third equation of stellar evolution* is given as

$$\frac{\mathrm{d}l}{\mathrm{d}m} = \epsilon_{\mathrm{nuc}} - \epsilon_{\nu} + \epsilon_{\mathrm{g}} \ . \tag{2.21}$$

Considering cell k in Fig. 2.2, the energy conservation is expressed as

$$l_k - l_{k+1} = \mathrm{d}m_k \left[\epsilon_{\mathrm{nuc}} - \epsilon_{\nu} + \epsilon_{\mathrm{g}}\right] \ . \tag{2.22}$$

MESA has the capacity to interpolate different nuclear reaction tables for the parameter ϵ_{nuc}. I specified the nuclear reaction tables based on the specific objectives under investigation. The commonly used nuclear reaction tables are from NACRE (Nuclear Astrophysics Compilation of Reaction Rates) collaboration (Angulo et al., 1999) and JINA REACLIB (Joint Institute for Nuclear Astrophysics Reaction Library) version 2.2 (Cyburt et al., 2010). ϵ_{ν} represents the thermal neutrino losses relevant for late evolved stages in massive stars. Refer to equation 12 in Paxton et al. (2011) for the details of MESA's implementation of ϵ_{g}.

2.1.4 Energy transport

In stars, there are three ways through which energy/heat can be transported. These include: radiation, convection, and conduction. Among these mechanisms of energy transport in stars, conduction is the least efficient mechanism. This requires very high densities in order for heat to be transferred through jostling of particles against each other. This process is known as "thermal conductivity". In the modelling routines, it is possible to interpolate conductive opacity tables. The two main energy transport processes are then

(i) Radiation: This is a dominant energy transport process in regions of the star where convection is inefficient. It involves energy transport through photons and this process can be thought of as a "diffusive process". Consider l_{ph}, the distance over which the intensity of the radiation beam decreases by a certain factor, to be expressed as

$$l_{\mathrm{ph}} = \frac{1}{\kappa\rho} \ , \tag{2.23}$$

where κ is the opacity and ρ is the density. The radiative conductivity, Q_{rad}, can be generated from the expression

$$Q_{\mathrm{rad}} = \frac{4}{3}\frac{acT^3}{\kappa\rho} \ , \tag{2.24}$$

where a is the radiative constant, c is the speed of light, and G is the gravitational constant. The radiative energy flux may then be defined as

$$E_{\text{flux}} = -Q_{\text{rad}} \nabla_{\text{T}} \ , \tag{2.25}$$

where ∇_{T} is the temperature gradient. Substituting equation 2.24 into equation 2.25, gives

$$E_{\text{flux}} = -\frac{4}{3} \frac{acT^3}{\kappa\rho} \nabla_{\text{T}} \ . \tag{2.26}$$

E_{flux} is similar to equation 2.20, thus equation 2.26 becomes

$$\frac{\mathrm{d}T}{\mathrm{d}r} = -\frac{3\kappa\rho}{16\pi acT^3} \frac{l}{r^2} \ . \tag{2.27}$$

Substituting equation 2.3 in equation 2.27 then gives

$$\frac{\mathrm{d}T}{\mathrm{d}m} = -\frac{3}{64\pi^2 ac} \frac{\kappa l}{r^4 T^3} \ . \tag{2.28}$$

This is the *fourth stellar structure equation*, and corresponds to the temperature gradient required to transport a luminosity, l. Using equation 2.15 and following the chain rule

$$\frac{\mathrm{d}T}{\mathrm{d}m} = \frac{\mathrm{d}P}{\mathrm{d}m} \frac{\mathrm{d}T}{\mathrm{d}P} \ , \tag{2.29}$$

and leads to,

$$\frac{\mathrm{d}T}{\mathrm{d}m} = -\frac{GmT}{4\pi r^4 P} \frac{\mathrm{dlog}T}{\mathrm{dlog}P} \ . \tag{2.30}$$

Taking $\nabla = \mathrm{dlog}T/\mathrm{dlog}P$, equation 2.30 becomes

$$\frac{\mathrm{d}T}{\mathrm{d}m} = -\frac{GmT}{4\pi r^4 P} \nabla \ . \tag{2.31}$$

The radiative temperature gradient is defined as

$$\nabla_{\text{rad}} = \left(\frac{\mathrm{dlog}T}{\mathrm{dlog}P} \right)_{\text{rad}} \ , \tag{2.32}$$

$$\nabla_{\text{rad}} = -\frac{3}{16\pi acG} \frac{klP}{mT^4} \ . \tag{2.33}$$

Equation 2.33 describes the logarithmic variation of temperature with depth (expressed in terms of pressure) in case radiation is the mechanism behind energy transport. Expressing equation 2.31 in connection with its implementation in

MESA, and again referring to cell k shown in Fig. 2.2, gives

$$\frac{T_{k-1} - T_k}{0.5(\mathrm{d}m_{k-1} - \mathrm{d}m_k)} = -\left(\frac{Gm_k}{4\pi r_k^4}\right) \nabla_{T,k} \frac{< T_k >}{< P_k >} \ , \tag{2.34}$$

where $< T_k >$ and $< P_k >$ are the average values of T and P between the two adjacent cells. Substituting equation 2.17 in equation 2.34 gives

$$\frac{T_{k-1} - T_k}{0.5(\mathrm{d}m_{k-1} - \mathrm{d}m_k)} = \nabla_{T,k} \left(\frac{\mathrm{d}P}{\mathrm{d}m}\right)_{\text{hydrostatic at } k} \frac{< T_k >}{< P_k >} \ . \tag{2.35}$$

(ii) Convection: When the temperature gradient in equation 2.33 is too steep, energy transfer through the radiation mechanism fails (Schwarzschild, 1958). Let us consider a parcel/bubble of gas inside the star and assume a small variation in the temperature of the parcel compared to its surroundings, and also assume a temperature equilibrium. If the parcel temperature rises above its surroundings, its density decreases, thus becoming lighter than its surroundings and driven upwards by the buoyancy force. The parcel of gas will travel until when the pressure equilibrium is broken (or it becomes unstable due to turbulence) thus dissolving in the surrounding gas. This is commonly referred to as "convective instability".

Schwarzschild's criterion states that convection is activated once the radiative temperature gradient exceeds the adiabatic temperature gradient (∇). Thus the criterion for instability is expressed as

$$\nabla_{\text{rad}} > \nabla_{\text{ad}} \ . \tag{2.36}$$

The adiabatic temperature gradient is defined as

$$\nabla_{\text{ad}} = \left(\frac{\mathrm{d}\log T}{\mathrm{d}\log P}\right)_{\text{ad}} \ . \tag{2.37}$$

Ledoux's criterion (Ledoux, 1947) for instability takes into account the mean molecular weight (μ) giving

$$\nabla_{\text{rad}} > \nabla_{\text{ad}} + \nabla_{\mu} \ , \tag{2.38}$$

where

$$\nabla_{\mu} = \left(\frac{\mathrm{d}\log T}{\mathrm{d}\log P} \right)_{\mu} \ . \tag{2.39}$$

I note that with the addition of ∇_{μ} to the Schwarzschild's criterion, the effect of Ledoux's criterion is towards stability.

In stellar modelling routines, the amount of heat transported by convection is usually estimated using the "mixing length theory" (Böhm-Vitense, 1958). This is an approximation of some characteristic distance a parcel of gas can travel without mixing with its surroundings. The mixing length model was first proposed by Ludwig Prandtl in 1925 (Prandtl and Angew, 1925). The mixing length, l_{m}, is considered to be proportional to the pressure scale height, H_{p}, such that

$$l_{\mathrm{m}} = \alpha_{\mathrm{mlt}} H_{\mathrm{p}} \ , \tag{2.40}$$

where α_{mlt} is a constant parameter. H_{p} is defined as the radial distance over which the pressure varies by an e-folding factor such that

$$H_{\mathrm{p}} = \left| \frac{\mathrm{d}r}{\mathrm{d}\ln P} \right| \approx \frac{P}{\rho g} \ , \tag{2.41}$$

where g is gravity and ρ is density. The mixing length parameter, α_{mlt}, is usually set through solar calibration based on the physics adopted in the stellar evolution code. The obtained solar calibrated value of α_{mlt} is then adopted as a fixed value in modelling other stars (e.g., Silva Aguirre et al. 2015, Joyce and Chaboyer 2018). Rosenthal et al. (1999) demonstrated using 3D convection simulations aimed at calibrating α_{mlt} that it varies significantly along the main–sequence phase and decreases with increasing mass. It is for this reason that I vary α_{mlt} when constructing stellar evolution grids. Usually α_{mlt} may be set to vary from 1.4 to 2.5. Furthermore, Rosenthal et al. (1999) also shows that stars ascend the giant branch with a relatively constant value of α_{mlt}. Treatment of convection according to equation 2.40 is still far from being a perfect theory in describing convection. One of the main setbacks is that it allows for circumstances where convective velocity of a parcel is non–zero yet convection acceleration goes to zero at the convective boundary. This results into parcels penetrating into convectively stable regions, thus extending the convective region boundary. This process is called "convective overshoot". This has significant effects on the lifetime of main–sequence stars with convective cores. Convective core overshoot drags

fuel (hydrogen in the case of main–sequence stars) into the core which extends the star's lifetime on the main–sequence phase. Furthermore, convective core overshoot has been shown to be a important process in models with masses above 1.1 $M_{\odot}$. It has been illustrated that the sizes of convective cores are larger than those predicted by models that adopt the pure Schwarzschild's criterion in defining convective core sizes (e.g., Maeder 1974, Bucaro et al. 1991, Chiosi et al. 1992, VandenBerg et al. 2007). In practice, stellar evolution codes may treat this convective overshoot extension ($l_{\rm ov}$) as

$$l_{\rm ov} = \alpha_{\rm ov} H_{\rm p} \ , \tag{2.42}$$

where $\alpha_{\rm ov}$ is a dimensionless constant that may be calibrated against observations. I implement core overshoot in models with convective cores following the exponential diffusive overshoot expression of Herwig (2000) given as

$$D_{\rm c} = E_0 \exp\left(\frac{-2z}{l_{\rm ov}}\right) \ , \tag{2.43}$$

where $D_{\rm c}$ is the diffusion coefficient in the overshoot region and E_0 is the diffusion coefficient in the convectively unstable region near the boundary determined based on the mixing length theory. $l_{\rm ov}$ is defined following equation 2.42, and z is the distance from the edge of the convective zone. The mixing length theory according to Böhm-Vitense (1958) is fairly successful in describing convection in the deep stellar interiors where convective zones are assumed to be perfectly mixed and adiabatically stratified. However, in regions where convection is inefficient, such as the near surface layers of solar–type stars, the mixing length theory fails to describe convection.

In sum, MESA solves the equations of stellar structure described in Sects. 2.1.1, 2.1.2, and 2.1.3 for the structure parameters T, l, P, r, ρ etc., and composition parameters like mass fractions of different elements. It interpolates the equation of state expressed in terms of tables of ρ –T in order to perform the integration of the stellar equations. MESA employs the Newton–Raphson approach given as (Paxton et al., 2011)

$$0 = \vec{F}(\vec{y}) = \vec{F}(\vec{y_i} + \delta\vec{y_i}) = \vec{F}(\vec{y_i}) + \left[\frac{{\rm d}\vec{F}}{{\rm d}\vec{y}}\right]_i \delta\vec{y_i} + O(\delta\vec{y_i}^2) \ , \tag{2.44}$$

where y_i is a trial solution based on the previous model parameters or initial guesses, $[{\rm d}\vec{F}/{\rm d}\vec{y}]_i$ is the Jacobian matrix calculated analytically (MESA modules determine

the output quantities and their associated partial derivatives with respect to the input quantities), $\vec{F}(\vec{y_i})$ is the residual, and $\delta\vec{y_i}$ is the correction. It is also worth noting that the MESA "star" module implements a Henyey–like code (Henyey et al., 1959) where the solutions to the stellar structure at a given evolution point are determined by considering the initial/trial solution, y_i, and varying all the parameters until the required degree of accuracy is achieved.

2.2 Theory of stellar pulsations

In this section, I provide an overview of the equations of linear adiabatic stellar oscillations. This is meant to set a platform that allows for the determination of stellar oscillation frequencies which aid in the exploration of the stellar interior structure. In addition, the equations of stellar oscillations are discussed extensively in the literature, such as in Unno et al. (1979), Cox (1980), Unno et al. (1989), Christensen-Dalsgaard (2002), Aerts et al. (2010). Furthermore, a comprehensive introduction to hydrodynamics with an interesting relation to stellar oscillations is discussed by Ledoux and Walraven (1958). I note that, oscillation frequencies for the different stellar models derived in this thesis were calculated using the GYRE oscillation code (Townsend and Teitler, 2013).

Let us consider a hydrodynamic system with physical quantities given as a function of position, $\vec{r}$, and time, t, such that pressure, density, and velocity are expressed as $p(\vec{r},\ \mathrm{t})$, $\rho(\vec{r},\ \mathrm{t})$, and $\mathrm{v}(\vec{r},\ \mathrm{t})$, respectively. The conservation laws of hydrodynamics include:

(i) Conservation of mass: This expresses the rate of change of mass in a given volume as

$$\frac{\partial \rho}{\partial t} + \nabla(\rho\vec{v}) = 0\ . \tag{2.45}$$

This is also known as the continuity equation.

(ii) Conservation of momentum: This states that the rate of change in linear momentum of a fluid element must be equal to the force exerted on it by its surroundings. This is given by

$$\rho\frac{d\vec{v}}{dt} = -\nabla p + \rho g + \vec{F}\ , \tag{2.46}$$

where $\vec{F}$ is the body force per unit mass. This includes other forces acting on the body apart from gravity, such as magnetic forces. Equation 2.46 is sometimes known as the equation of motion.

In addition to equation 2.46, the gravitational acceleration, $\vec{g}$, is expressed as the gradient of the gravitational potential, i.e.,

$$\vec{g} = -\nabla\Phi, \tag{2.47}$$

where Φ satisfies Poisson's equation following the expression

$$\nabla^2\Phi = 4\pi G\rho \ , \tag{2.48}$$

where G is the gravitational constant.

(iii) Conservation of energy: This arises from the first law of thermodynamics which states that; the change in the internal energy of the fluid must be equal to the heat supplied to the system minus the work done in expanding or compressing the fluid. It can be expressed mathematically as

$$\frac{\mathrm{d}q}{\mathrm{d}t} = \frac{\mathrm{d}E}{\mathrm{d}t} + p\frac{V}{\mathrm{d}t} \ , \tag{2.49}$$

where q is the heat supplied, E is the internal energy per unit mass, and V is the volume (i.e., $V = 1/\rho$). Equation 2.49 is sometimes given in terms of the following parameters

$$\frac{\mathrm{d}q}{\mathrm{d}t} = \frac{1}{\rho(\Gamma_3 - 1)}\left(\frac{\mathrm{d}p}{\mathrm{d}t} - \frac{\Gamma_1 p}{\rho}\frac{\mathrm{d}\rho}{\mathrm{d}t}\right) \ , \tag{2.50}$$

where Γ_1 and Γ_3 are adiabatic exponents defined by the adiabatic derivatives

$$\Gamma_1 = \left(\frac{\partial \ln p}{\partial \ln \rho}\right)_{\mathrm{ad}} \ , \ \Gamma_3 - 1 = \left(\frac{\partial \ln T}{\partial \ln \rho}\right)_{\mathrm{ad}} , \ \text{ and } \ \frac{\Gamma_2 - 1}{\Gamma_2} = \left(\frac{\partial \ln T}{\partial \ln p}\right)_{\mathrm{ad}} .$$

In order to derive the equations that describe stellar oscillations, one considers small perturbations of a static stellar structure, which creates variations in the physical quantities such as pressure, density, among others. Before describing the perturbation analysis of the above conservation laws, it is important that the following assumptions are put into consideration about the equilibrium state:

(i) It is static such that there are no velocities, i.e.,

$$\frac{\partial}{\partial t} = 0 \ .$$

This assumption does hold since the pulsation timescales are much smaller than the evolution timescale at least for the main–sequence stars studied in this thesis.

(ii) I consider no magnetic field or rotation and hence the equilibrium state is spherically symmetric.

In addition to the above assumptions, the following assumptions are made about the perturbations:

(iii) I consider perturbations to be adiabatic. This assumption fails near the surface because it assumes no energy change between the oscillations and the equilibrium structure.

(iv) Perturbations are assumed to be linear and small. Non–linear terms in the perturbations are ignored.

The perturbations are described in two frameworks, i.e., the Eulerian and Lagrangian perturbations. The Eulerian perturbation corresponds to the perturbation of a physical quantity at a given position, $\vec{r_0}$. The Lagrangian perturbation relates to time evolution of a physical quantity while following its motion. This is commonly denoted by the symbol, δ.

Consider f to be a physical quantity of a fluid such that

$$f = f_0 + f' \ , \tag{2.51}$$

where f' is the Eulerian perturbation. Then the Lagrangian perturbation is expressed as

$$\delta f = f' + \delta\vec{r}\nabla f_0 \ . \tag{2.52}$$

Please note that the subscript "0" denotes the equilibrium state of a chosen physical quantity, with $\delta\vec{r}$ the displacement, such that

$$\delta\vec{r} = \vec{r} - \vec{r_0} \ .$$

Also,

$$\vec{v} = \frac{\mathrm{d}\delta\vec{r}}{\mathrm{d}t} \approx \frac{\partial\delta\vec{r}}{\partial t} + (\vec{v}\cdot\nabla)\delta\vec{r} \ .$$

Since $(\vec{v}.\nabla)\delta\vec{r}$ is very small, then

$$\vec{v} = \frac{\mathrm{d}\delta\vec{r}}{\mathrm{d}t} \approx \frac{\partial\delta\vec{r}}{\partial t} \ . \tag{2.53}$$

Taking into account all of the above assumptions, the conservation equations can now be expressed in perturbed form.

2.2.1 Perturbed continuity equation

From equation 2.45, substituting for $\rho = \rho_0 + \rho'$ and $\vec{v}$ using equation 2.53 gives

$$\frac{\partial}{\partial t}\left(\rho_0 + \rho'\right) + \nabla \cdot (\rho_0 + \rho')\frac{\partial \delta\vec{r}}{\partial t} = 0 \ . \tag{2.54}$$

Considering the equilibrium structure to be static, equation 2.54 becomes

$$\frac{\partial \rho'}{\partial t} + \nabla \cdot \left(\rho_0 \frac{\partial \delta\vec{r}}{\partial t}\right) = 0 \ . \tag{2.55}$$

Integrating with respect to time,

$$\rho' + \nabla \cdot (\rho_0 \delta\vec{r}) = 0 \ . \tag{2.56}$$

Equation 2.56 gives the perturbed continuity equation and expanding it further gives

$$\rho' + \rho_0 \cdot \nabla\delta\vec{r} + \delta\vec{r} \cdot \nabla\rho_0 = 0 \ .$$

The term $(\delta\vec{r} \cdot \nabla\rho_0)$ is very small, thus the perturbed continuity equation in Lagrangian form is given by

$$\rho' - (\rho_0 \nabla\delta\vec{r}) = 0 \ . \tag{2.57}$$

2.2.2 Perturbed equation of motion

From equation 2.46, considering the assumption that the equilibrium state is spherically symmetric ($\vec{F} = 0$) and substituting for $\vec{g}$ from equation 2.47, gives

$$\rho \frac{\mathrm{d}\vec{v}}{\mathrm{d}t} = -\nabla p - \rho\nabla\Phi \ . \tag{2.58}$$

Considering $p = p_0 + p'$, $\Phi = \Phi_0 + \Phi'$, equation 2.58 becomes

$$\rho_0 \left(\frac{\partial \vec{v}}{\partial t} + \vec{v} \cdot \nabla\vec{v}\right) = -\nabla(p_0 + p') - (\rho_0 + \rho')\nabla(\Phi_0 + \Phi') \ . \tag{2.59}$$

Considering the assumptions stated in Sect. 2.2, equation 2.59 then reduces to

$$\rho_0 \frac{\partial}{\partial t}\left(\frac{\partial \delta\vec{r}}{\partial t}\right) = -\nabla p' - \rho'\nabla\Phi_0 - \rho_0\nabla\Phi' \ .$$

The perturbed equation of motion becomes

$$\rho_0 \frac{\partial^2 \delta\vec{r}}{\partial t^2} = -\nabla p' - \rho'\nabla\Phi_0 - \rho_0\nabla\Phi' \ . \tag{2.60}$$

The gravitational acceleration is related to the gravitational potential as expressed in equation 2.47, and the gravitational potential of the volume, V, of a star in equilibrium state takes an integral form given as

$$\Phi(r,\vec{t}) = -G\int_V \frac{\rho(\vec{r'},t)}{\mid r - r' \mid} dV \ . \tag{2.61}$$

The perturbed Poisson equation then takes the form

$$\nabla^2\Phi' = 4\pi G\rho' \ . \tag{2.62}$$

2.2.3 Perturbed energy equation

We express the energy equation as

$$\frac{\mathrm{d}p}{\mathrm{d}t} = \frac{\Gamma_1 p}{\rho}\frac{\mathrm{d}\rho}{\mathrm{d}t} \ . \tag{2.63}$$

This can also take the form

$$\frac{\partial p}{\partial t} + \vec{v}\cdot\nabla p = \frac{\Gamma_1 p}{\rho}\left(\frac{\partial \rho}{\partial t} + \vec{v}\cdot\nabla\rho\right) \ . \tag{2.64}$$

Considering adiabatic perturbations, and $\Gamma_1 = \Gamma_{1,0} + \Gamma_1'$, after substituting in equation 2.64 and eliminating small terms gives

$$\frac{\partial p'}{\partial t} + \frac{\partial \delta\vec{r}}{\partial t}\nabla\cdot p_0 = \frac{\Gamma_{1,0}p_0}{\rho_0}\left(\frac{\partial \rho'}{\partial t} + \vec{v}\cdot\nabla\rho_0\right) \ . \tag{2.65}$$

Substituting for $\vec{v}$,

$$\frac{\partial}{\partial t}\left(p' + \delta\vec{r}\cdot\nabla p_0\right) = \frac{\Gamma_{1,0}p_0}{\rho_0}\cdot\frac{\partial}{\partial t}\left(\rho' + \delta\vec{r}\cdot\nabla\rho_0\right) \ , \tag{2.66}$$

$$\frac{\partial}{\partial t}(\delta p) = \frac{\Gamma_{1,0} p_0}{\rho_0} \cdot \frac{\partial}{\partial t}(\delta \rho) \ . \tag{2.67}$$

Integrating with respect to time, and since $(\Gamma_{1,0} p_0)/\rho_0$ is independent of time, the perturbed energy equation takes the form

$$\delta p = \frac{\Gamma_{1,0} p_0}{\rho_0} \cdot \delta \rho \ . \tag{2.68}$$

Equations 2.57, 2.60, 2.62, and 2.68 are used to describe linear adiabatic perturbations of a spherical star. These equations can be solved with appropriate boundary conditions with variables $\rho', p', \Phi', \delta\vec{r}$. In a spherical (polar) coordinate system (r, θ, φ), the variables $\rho', p', \Phi', \delta\vec{r}$ are expressed as ξ, θ, φ, and t. The spatial harmonics are represented by $Y_l^m(\theta, \varphi)$, where l is the spherical harmonic degree describing the variation of the physical quantities in terms of co–latitude, θ, and m is the azimuthal order describing the variation of these quantities in longitude, φ. The angular variation of all physical quantities is described by these two numbers, i.e., $l, and m$. The general solution to the system of linear adiabatic equations in spherical coordinates takes the form:

$$f'(r, \theta, \varphi, t) = \mathrm{Re}\{f'(r) Y_l^m(\theta, \varphi) \exp(i\omega t)\} \ , \tag{2.69}$$

$$\xi_r(r, \theta, \varphi, t) = \mathrm{Re}\{\vec{\xi_r}(r) Y_l^m(\theta, \varphi) \exp(i\omega t)\} \ , \tag{2.70}$$

$$\xi_h(r, \theta, \varphi, t) = \mathrm{Re}\{\vec{\xi_h}(r) \nabla_h Y_l^m(\theta, \varphi) \exp(i\omega t)\} \ , \tag{2.71}$$

where the time dependence is expressed as $\exp(i\omega t)$ since the solutions searched for are periodic and f' is any perturbation of a physical quantity. ξ_r and ξ_h are the radial and horizontal displacements, respectively, ∇_h represents the horizontal gradient and ω is the angular oscillation frequency, which is real and yields an oscillatory solution in time (ω can be imaginary implying that the solution grows or decays). *I note that ω is real because of the assumption that the perturbations are adiabatic and thus the boundary conditions are fully reflective (i.e., no energy is lost through the boundary).* The solutions to the set of pulsation equations are attained by setting boundary conditions both at the centre and surface of the star. This results in an eigenvalue problem with solutions existing for only discrete values of frequency, $\omega_{l,n}$, where n is the radial order which is related to the radial structure of the different eigenfunctions that exist for the same mode degree, l. I recall here that spherical symmetry is assumed for the equilibrium state, therefore the equations are independent of the azimuthal order, m. The equations of stellar pulsations present a numerical root finding problem. This is the genesis of numerous seismic codes currently available.

Stellar pulsation codes have been employed to provide full solutions to the pulsation equations taking into account the associated boundary conditions in a reliably fast, robust, maximum use of all available computational resources such as cluster nodes, and requiring minimal interruption such as hand–tuning. Examples of seismic codes include: the Aarhus adiabatic oscillation package (ADIPLS; Christensen-Dalsgaard 2008), Porto Oscillation Code (POSC; Monteiro 2008), Granada oscillation code (GraCo; Moya and Garrido 2008), GYRE (Townsend and Teitler, 2013), among others. Monteiro (2009) gives a comprehensive overview of a variety of seismic code commonly used and the most notable difference lies in the numerical schemes (such as relaxation schemes, shooting schemes) employed in each codes so as to determine the model oscillation frequencies. In this thesis, I use the seismic code GYRE (Townsend and Teitler, 2013) to calculate the eigenfrequencies of an input stellar model generated using MESA. GYRE has the capacity to address both adiabatic and non–adiabatic pulsation problems and is currently undergoing further development so that it handles the effects of rotation. I note that no comparisons between GYRE and other seismic tools were carried out in this thesis, however, Townsend and Teitler (2013) reports a good agreement between GYRE and other oscillation codes. For instance, they found differences between GYRE and GraCo frequencies for the "M4k" model generated by Moya et al. (2008) to be $\lesssim$ 4 nHz and $\lesssim$ 14 nHz for the radial modes and $l = 3$ modes, respectively, across the frequency range $20 \leq \nu \leq 2500$ μHz. GYRE employs a numerical root finding scheme known as "Magnus Multiple Shooting" (see Townsend and Teitler 2013) to evaluate the discriminant function at a discrete sequence of frequencies. The set of eigenfrequencies exist where the discriminant function is zero. To determine these regions, GYRE carries out a scan across the frequency interval specified by the user, by first evaluating the discriminant function at n points distributed within this interval, yielding regions where the discriminant changes sign. The neighbouring points where the discriminant changes sign indicate that a root exists between these points. These points are then used as initial guesses to narrow down the exact points where the determinant is zero and thus eigenfrequencies are obtained. Extended GYRE mathematical details and numerical scheme implementations are described in Townsend and Teitler (2013).

The set of perturbed pulsation equations can be rewritten including two characteristic frequencies, i.e., the Lamb frequency, S_l, and the buoyancy frequency, N, respectively defined as

$$S_l^2 = \frac{l(l+1)}{r^2} c^2 \ , \tag{2.72}$$

where c is the adiabatic sound speed, and

$$N^2 = g\left(\frac{1}{\Gamma_{1,0}}\frac{\mathrm{dln}p}{\mathrm{d}r} - \frac{\mathrm{dln}\rho}{\mathrm{d}r}\right) \ . \tag{2.73}$$

The buoyancy frequency is only defined in stellar regions that are stable to convection, i.e., $N^2 > 0$. I employ this in distinguishing between main–sequence stellar models with and without convective cores. I now pay more attention to p modes, whose frequencies are considered as seismic observables in this thesis. For p modes, the radial modes, $l = 0$, propagate through the entire stellar structure — they act as a diagnostic of average information about the different sections of the star. Through inspection of the propagation depths of p modes for the different spherical degrees (see Fig. 2.3), as the spherical degree increases, the propagation depth decreases — higher degree modes carry information about the stellar surface. It is important to note here that theoretical oscillation frequencies of any degree can be calculated, however, ground–based and space–based observations are only able to yield frequencies for $l \lesssim 3$. This is because observation and measurement of oscillation frequencies of distant stars have essential limitations. As the oscillations approach and recede on the stellar surface, i.e., the star becomes brighter and fainter respectively, these patterns created by non–radial oscillations present challenges to resolve because only the total effect of oscillations both in radial velocity and photometry is measured. As a result oscillations with high spherical degree cancel out (or average out) and their observed amplitudes are also considerably reduced. This is commonly referred to as the "cancellation effect" or "geometric cancellation" (Dziembowski, 1977).

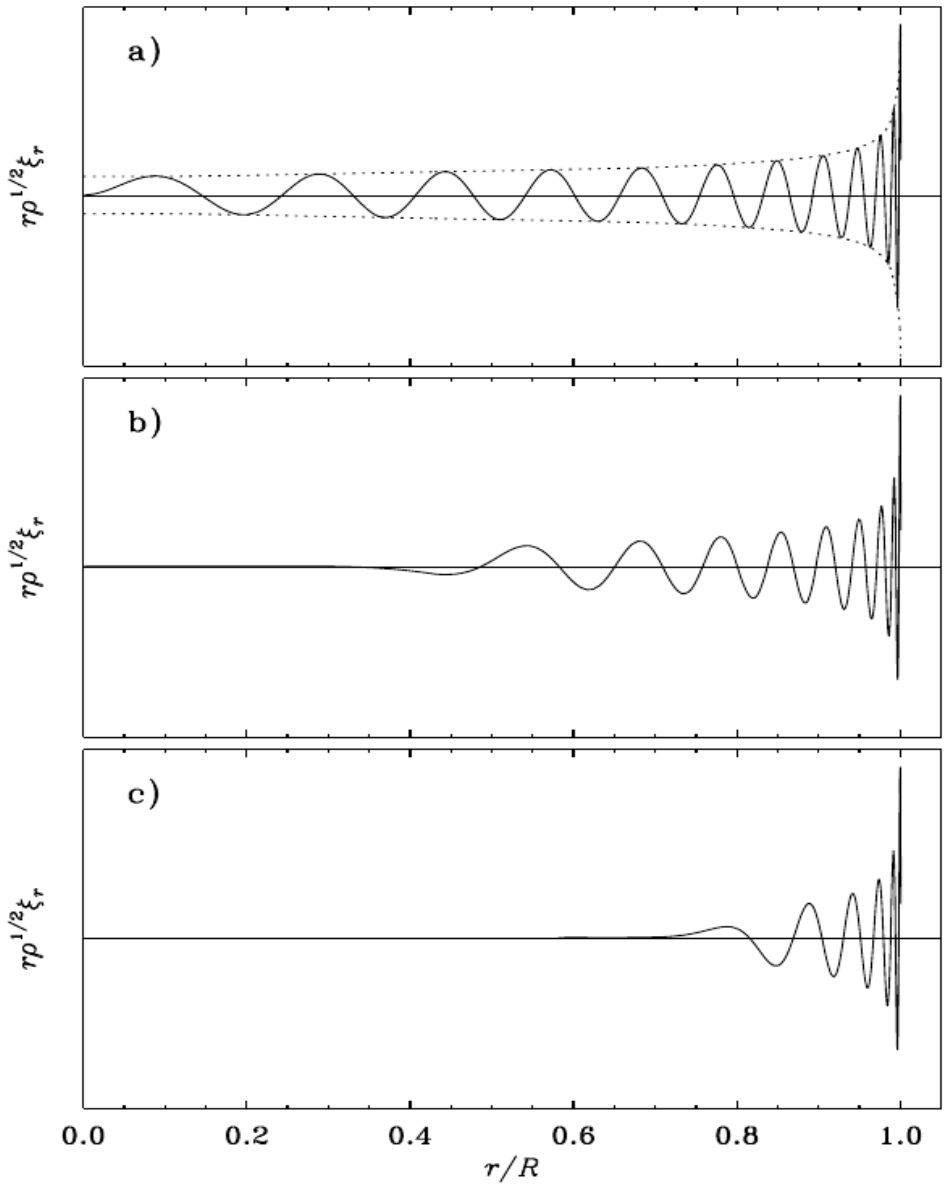

Figure 2.3: Energy density from the radial component of velocity ($r\rho^{1/2}\xi_r$) as a function of fractional radius (r/R) for selected p modes in a solar model. Top panel (a) shows an $l = 0$ mode, with $n = 23$, $\nu = 3310$ μHz. This mode propagates throughout the star. High–degree modes, such as the ones depicted in the middle and bottom panels, only probe the outer stellar structure. Panel (b) has $l = 20$, $n = 17$, $\nu = 3375$ μHz while panel (c) has $l = 60$, $n = 10$, $\nu = 3234$ μHz. Figure taken from Aerts et al. (2010).

Chapter 3

Stellar physics and stellar parameter derivation

Defining the structure of a stellar model in a particular evolutionary state not only involves solving the stellar structure equations described in Sect. 2 but also entails describing its internal physical processes, which essentially rely on the properties of stellar matter commonly known as "microphysics and macrophysics". Variation in the choice of a particular microphysics specification in stellar modelling routines may have limited impact on the stellar model parameters such as mean density, radius, mass, and age, but have a significant impact on the internal stellar structure. Such microphysics include: opacities, nuclear reactions, equation of state, and solar metallicity mixtures. Macrophysics choices have a substantial impact on the stellar model parameters and interior structure. These include: chemical transport processes such as, convection, semi–convection, convective overshooting, radiative acceleration, rotational mixing, among others. I note that, throughout this chapter, discussions are directed towards unveiling the model physics and other optimisation state–of–the–art challenges being addressed in this thesis. This chapter also includes a detailed application of the stellar evolution code, pulsation code, and optimisation tool employed in this thesis in modelling the Sun and the asteroseismic binary HD 176465.

3.1 Stellar model physics

The model physics explored in this thesis include: atomic diffusion, solar metallicity mixtures, opacities, and nuclear reaction rates. The discussions are directed towards highlighting how each model physics is treated during the modelling process and the

motivation for exploring its impact on both the stellar model parameters and interior structure.

3.1.1 Atomic diffusion

One of the essential chemical transport processes that occurs in radiative regions of stars is atomic (element/microscopic) diffusion. This is essentially enhanced by the fact that stars are self–gravitating spheres — and so develop temperature, pressure, and density (composition) gradients. Temperature gradients result in thermal diffusion which drives highly charged and more massive elements towards the centre of the star (i.e., hottest stellar region); gravity or pressure gradients cause gravitational settling — tends to concentrate heavier elements towards the centre of the star; and composition gradients result in chemical diffusion. In addition, hydrogen diffuses outwards while helium diffuses towards the stellar centre, because the rate of change of hydrogen mass fraction is equal and opposite to the rate of change of the helium mass fraction (Thoul et al., 1994). Furthermore, atomic diffusion includes contributions from radiation pressure and ionization of chemical elements of the stellar plasma. It is worth noting that atomic diffusion is only efficient in the stellar radiative regions and less efficient in convective regions because convection is a highly vigorous process that occurs on shorter timescales.

Chapman (1917a,b) made theoretical predictions of the occurrence of atomic diffusion in stars. Later, detailed studies were directed towards exploring its effects on solar models and other stars (e.g., Aller and Chapman 1960, Michaud 1970, Noerdlinger 1977, Fontaine and Michaud 1979, Vauclair and Vauclair 1982). Atomic diffusion is also known to have been first suggested as the cause for large scale chemical peculiarities in main–sequence and horizontal–branch stars (e.g., Michaud et al. 1976, 1983, 2008, Richer et al. 2000). Solar studies through helioseismology strongly support the existence of atomic diffusion in its interior (e.g., Christensen-Dalsgaard et al. 1993b, Basu and Antia 1994, Bahcall et al. 1995, Richard et al. 1996). Helioseismology studies show that it is essential to include atomic diffusion if the Sun's current age is to be determined with high accuracy and precision. Furthermore, the chemical composition gradients in the stellar radiative regions cause drastic changes in the expected initial chemical composition of solar models and their structure (e.g., Christensen-Dalsgaard 2002).

The stellar evolution code (MESA) employed in this thesis includes atomic diffusion implemented according to Thoul et al. (1994). This involves solving a set of fluid flow equations described by Burgers (1969). The equations of diffusion are described in detail in section 18 of Burgers (1969) and their implementation in MESA in section 9

of Paxton et al. (2015). Here, I highlight some important expressions:

$$\nabla p_s - \rho_s \vec{g} - \rho_s \vec{E} = \sum_{t \neq s} K_{st}(\vec{w}_t - \vec{w}_s) + \sum_{t \neq s} K_{st} z_{st} \frac{m_t \vec{r}_s - m_s \vec{r}_t}{m_s + m_t} \ , \tag{3.1}$$

$$\nabla p_s + \rho_s(\vec{g} - \vec{g}_{\mathrm{rad},s}) - \rho_s \vec{E} = \sum_{t \neq s} K_{st}(\vec{w}_t - \vec{w}_s) + \sum_{t \neq s} K_{st} z_{st} \frac{m_t \vec{r}_s - m_s \vec{r}_t}{m_s + m_t} \ , \tag{3.2}$$

where $\vec{g}$ is the gravitational acceleration, $\vec{E}$ is the quasi–static electric field, ρ_s is the average charge density of a particle of species s or t, $\vec{w}_t$ and $\vec{w}_s$ are the diffusion velocities of species s and t, respectively, m_s and m_t are the masses of species s and t, respectively, p_s is the pressure of species, s, and $\vec{g}_{\mathrm{rad},s}$ is the radiative acceleration on species, s. The description of the physics in the ideal gas of a particular kind of interactions is embedded in the friction coefficients K_{st} and z_{st}. Equation 3.2 includes a component of the radiative acceleration while equation 3.1 does not. Radiative acceleration is reported to have a negligible impact in stars within the same mass range as the Sun, i.e., below 1.1 $\mathrm{M}_\odot$. This is because radiative acceleration is systematically weak compared to gravitational settling or gravity in such stars (Turcotte et al., 1998, Dotter et al., 2017, Deal et al., 2018). MESA includes the radiative acceleration following Hu et al. (2011) as described in equation 3.2 and its impact on stars above 1.1 $\mathrm{M}_\odot$ has been partly addressed in Deal et al. (2018). *It is worth noting that my inclusion of atomic diffusion does not take into account radiative acceleration but considers all other components of diffusion such as thermal diffusion, ionisation, gravitational settling, and is therefore based on equation 3.1* .

Figure 3.1 illustrates the difference between two main–sequence evolutionary tracks constructed with and without atomic diffusion[1]. The evolutionary tracks were computed using MESA, with the initial metal mass fraction (Z_0), initial helium mass fraction (Y_0), and mixing length alpha parameter (α_{mlt}) of 0.018, 0.27, and 1.8, respectively. I note that the remaining model physics (such as nuclear reactions, equation of state, opacities, metallicity mixture options, among others) adopted in the construction of these evolutionary tracks is described in Nsamba et al. (2017). Close to the zero age main–sequence (ZAMS), the effective temperature and luminosity of two evolutionary tracks constructed with and without diffusion is the same. This is because 1 $\mathrm{M}_\odot$ ZAMS models are mostly convective and thus the impact of atomic diffusion is negligible in those models. By the time models attain a luminosity with $\log L/\mathrm{L}_\odot = 0.0$, a

[1]Note that I consider diffusion of hydrogen and gravitational settling of helium, oxygen, and iron.

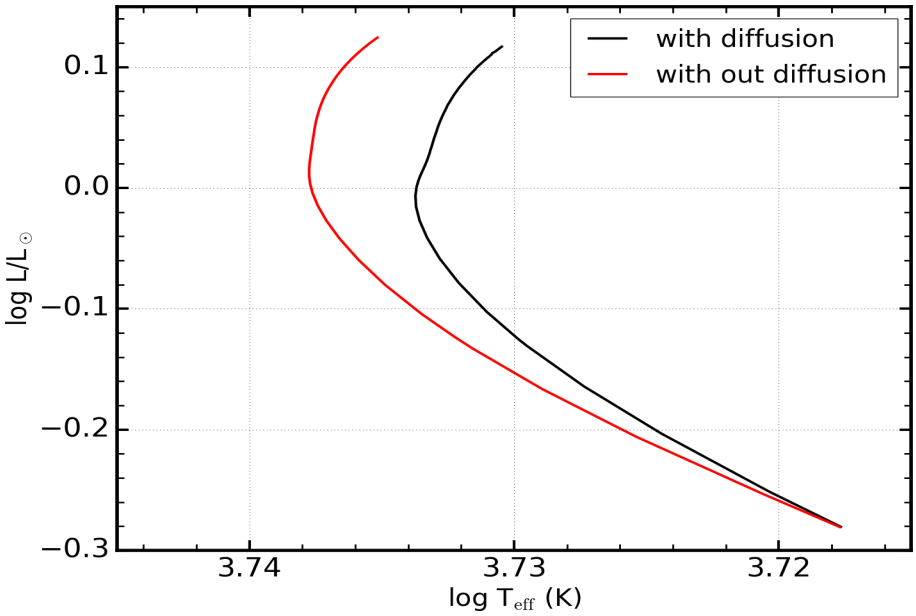

Figure 3.1: Main–sequence evolutionary tracks for 1 $M_\odot$ with and without diffusion.

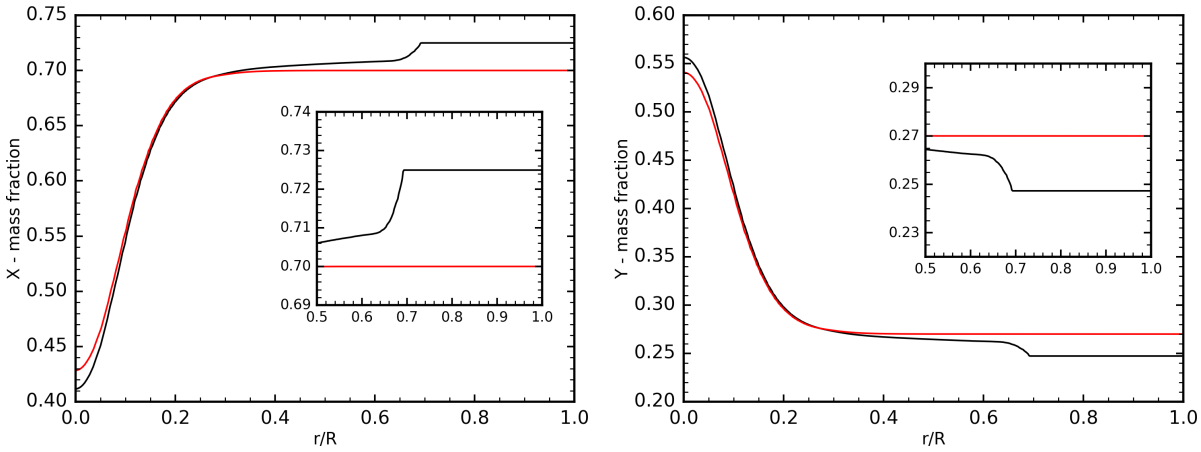

Figure 3.2: Hydrogen (X) and Helium (Y) mass fraction for 1 $M_\odot$ models with (black line) and without (red line) atomic diffusion as a function of the fractional change in radius. Each panel contains an inset showing the different profiles near the base of the convection zone.

significant difference in the effective temperature is visible, with models having atomic diffusion cooler than models without atomic diffusion (see Fig. 3.1).

Figure 3.2 shows the X and Y mass fraction profiles of 1 $M_\odot$ models at approximately 5 Gyr generated with and without atomic diffusion as part of the chemical transport physics taking place in their interiors. In the outer convective envelope of both models, the hydrogen and helium abundances are uniform because convection enhances a fully mixed region (see left and right panels of Fig. 3.2). For the model with atomic diffusion,

this extends from the surface to the base of the convection zone situated at a radius r = 0.70 R (see insets in Fig. 3.2). Gravitational settling causes surface helium settling, which reduces the surface helium abundance as shown in the right panel of Fig. 3.2. Nuclear fusion reduces the amount of hydrogen abundance in the interior part of the star. In addition, as the surface helium settles towards the core of the model, hydrogen diffuses towards the star surface (see left panel of Fig. 3.2). This is known to enhance a faster evolution along the main–sequence since a model runs out of its fuel (hydrogen) much faster compared to when atomic diffusion is neglected. It is for this reason that I include atomic diffusion when modelling low–mass stars (i.e., below 1.1 $M_{\odot}$).

In standard stellar modelling routines, atomic diffusion is not always included. This motivates the exploration of the systematic uncertainties on the derived stellar parameters (namely, mean density, radius, mass, and age) associated with the inclusion of atomic diffusion in models of low–mass solar–type stars.

Inclusion of atomic diffusion in stars with masses above 1.1 $M_{\odot}$, i.e., stars with convective cores, still presents modelling challenges. As the size of the convective envelope decreases, atomic diffusion drains the surface layers of their heavy elements and helium, resulting into differences between model surface abundances and observations (e.g., Stancliffe et al. 2016, Goupil 2018). It is for this reason that some stellar evolutionary grids (such as the Geneva grid; Mowlavi et al. 2012) and most stellar modellers (e.g., Silva Aguirre et al. 2015, 2017, Verma et al. 2019) ignore atomic diffusion. It is thought that adding radiative acceleration to the modelling routine will hinder the over settling of heavy elements, although surface helium depletion still remains a problem (Goupil, 2018).

3.1.2 Composition mixtures

Chemical abundances are one of the vital inputs that have to be specified in stellar evolution calculations. These include: hydrogen mass fraction (X), helium mass fraction (Y), and heavy element mass fraction (Z). These values are specified by the user in stellar evolution codes ensuring that

$$X + Y + Z = 1 \ . \tag{3.3}$$

The iron abundance, [Fe/H], obtained through observation can be transformed into an estimate of the heavy–element mass fraction needed during stellar evolution calculations,

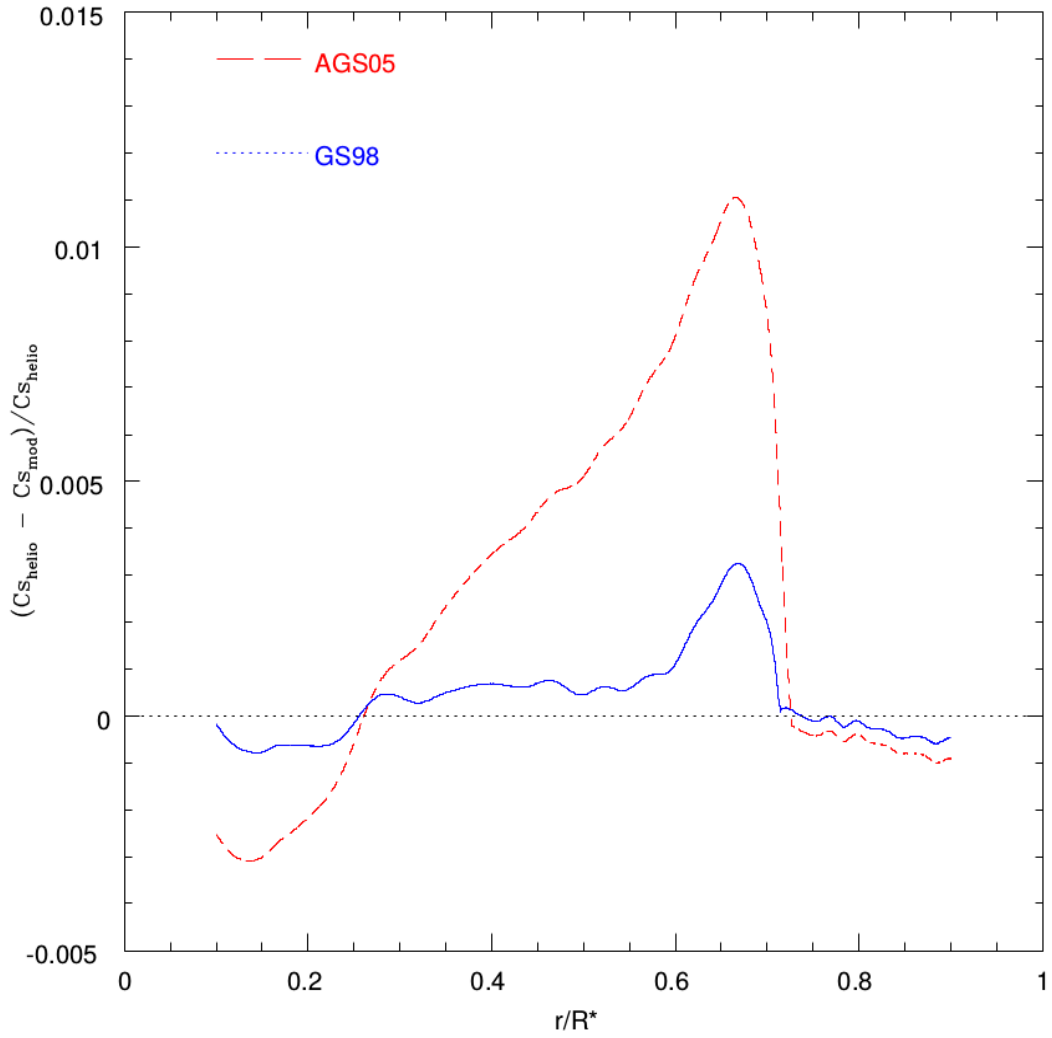

Figure 3.3: Dashed curves show the inferred sound speed profiles for different composition mixtures used in creating a solar model. The dotted black horizontal line represents a condition of agreement between the sound speed from helioseismology and models constructed with different compositions. Figure taken from Delahaye and Pinsonneault (2006).

following the expression

$$[\mathrm{Fe/H}] = \log\left(\frac{Z}{X}\right)_{\mathrm{star}} - \log\left(\frac{Z}{X}\right)_{\odot} . \tag{3.4}$$

I note that the abundances in equation 3.4 are surface abundances of the star and the Sun. Z represents heavier elements except helium. Equation 3.4 requires a solar reference value to be known for the conversion to be possible. Unfortunately, significant discrepancies exist in the absolute element abundances derived through the analysis of

the solar photospheric spectrum and meteorites, thus solar composition mixtures are still questionable to–date despite the various studies in the literature that have been dedicated to this subject (e.g., Anders and Grevesse 1989, Grevesse and Sauval 1998, Lodders 2003, Grevesse et al. 2007, Asplund et al. 2005, 2009). Anders and Grevesse (1989) and Grevesse and Sauval (1998) report surface solar values of Z of 0.0202 and 0.0170, respectively. These two mixtures yield a relatively good agreement with inferences from helioseismology. Figure 3.3 shows a good agreement between the sound speed profile predicted using helioseismology and that from the solar model with a composition of Grevesse and Sauval (1998). New sets of solar abundance measurements from Asplund et al. (2005) and Asplund et al. (2009) yield lower surface solar values of Z of 0.0122 and 0.0134, respectively. Figure 3.3 indicates large differences between the inferred sound speed profile from helioseismology and the solar model with the Asplund et al. (2005) composition.

The choice of solar chemical composition adopted in stellar modelling procedures is based on personal preference since no consensus has been reached to–date. In this thesis, I explore the impact of varying solar metallicity mixtures on the stellar parameters (namely, mean density, radius, mass, and age) of low–mass solar–type stars derived using forward modelling techniques. Furthermore, using α Centauri A as a reference, I explore the impact of varying metallicity mixtures in stellar modelling on determining the nature of its core.

It is worth noting that, depending on the metallicity mixtures adopted in the stellar evolution code, one has to ensure that they use the corresponding appropriate opacity tables so as to establish consistency. This is very important in regions where energy is transported by radiation as described using equation 2.33. In stellar evolution codes, opacities are given in table form as a function of temperature, density, and composition. The opacity tables commonly used in stellar evolution codes are from OPAL tables (Iglesias and Rogers, 1996) and OP tables (Badnell et al., 2005). These may be supplemented with more accurate low–temperature opacity tables, e.g., Ferguson et al. (2005).

With a set of preferred initial heavy element mass fraction ($Z_{\rm int}$) values, a stellar modeller has to establish a way to determine the initial helium mass fraction ($Y_{\rm int}$) values, so that values of the initial hydrogen mass fraction ($X_{\rm int}$) are determined based on equation 3.3. This presents one of the major current problems in stellar modelling. Among the different element abundances, helium abundance measurements in the Sun and solar–type stars are one of the poorly constrained ingredients in stellar modelling.

This is attributed to the fact that helium lines are not detectable in the spectra of stars with temperatures below 10,000 K. There are three ways stellar modellers overcome this. These include:

(i) supplying random possible values of Y to the stellar evolution code while ensuring that equation 3.3 is satisfied. The possible Y values range from the primordial big bang nucleosynthesis (BBN) value (i.e., $Y_{\rm BBN} \sim 0.2484$) to about 0.34. This approach, however, increases the number of variables used in constructing stellar grids and are hence costly in terms of time spent when constructing large stellar grids. Nevertheless, sub–$Y_{\rm BBN}$ values have been employed to explore if there are possibilities of generating optimal solutions with such initial helium mass fractions (e.g., Bonaca et al. 2012, Lebreton and Goupil 2014, Metcalfe et al. 2014, Silva Aguirre et al. 2017). Figure 3.4 shows the optimal initial helium mass

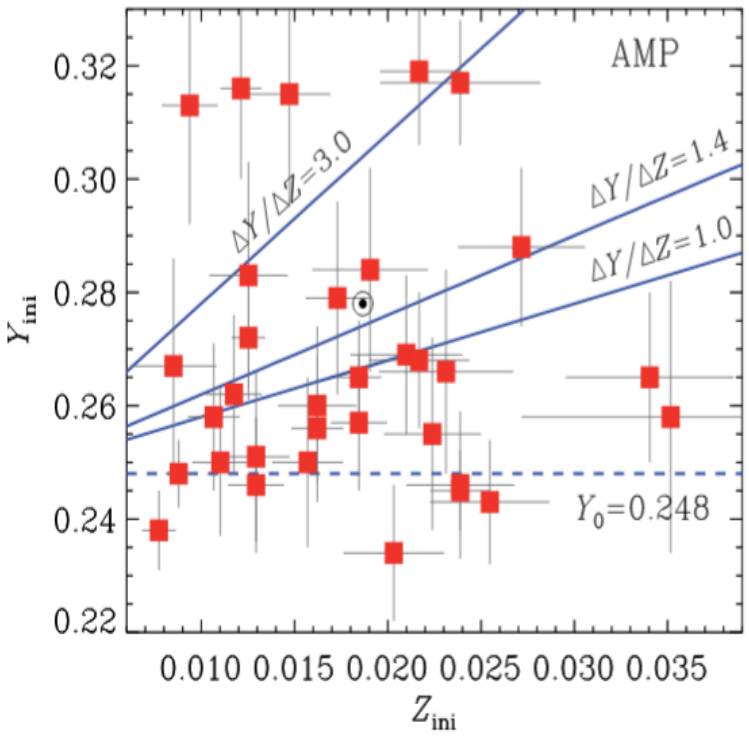

Figure 3.4: Initial metallicity versus initial helium abundance obtained using the Asteroseismic Modeling Portal (AMP; Metcalfe et al. 2009). Red squares represent 33 *Kepler* planet–candidate host stars, the solar symbol depicts the initial solar abundance from Serenelli and Basu (2010), the horizontal dashed line shows the primordial helium abundance value, while solid lines represent the different Galactic enrichment laws. Figure taken from Silva Aguirre et al. (2015).

fraction values obtained for a sample of planet–candidate host stars. A handful

of stars have initial helium mass fraction below the primordial $Y_{\rm BBN}$ value. This still currently presents a challenge to our understanding of why such values below the BBN threshold are possible.

(ii) determining Y through solar calibrations. This mainly involves varying Z, Y, and $\alpha_{\rm mlt}$, until a model is obtained that satisfies the observed oscillation frequencies, effective temperature, metallicity, luminosity, and radius at the current solar age. The optimal value of Y yielded by the solar model is then adopted in modelling other stars (e.g., Pietrinferni et al. 2004). This is advantageous because it reduces the number of free variables, thus one spends less time generating stellar models. However, it is not feasible to assume that all stars had the same initial Y as the Sun.

(iii) a more viable option is based on the "Galactic chemical evolution law", which is expressed as (Peimbert and Torres-Peimbert, 1976):

$$\frac{\Delta Y}{\Delta Z} = \frac{Y - Y_0}{Z - Z_0}, \tag{3.5}$$

where Y_0 and Z_0 are Big Bang Nucleosynthesis values, i.e., $Z = 0$ and $Y = 0.2484$. The absolute value of $\Delta Y/\Delta Z$ has been a cause of concern for over a decade. Jimenez et al. (2003) reported $\Delta Y/\Delta Z = 2.1 \pm 0.4$ using observations of nearby K dwarfs and a set of isochrones. Similar results were found by Casagrande et al. (2007) using a set of Padova isochrones and observations of nearby K dwarf stars (i.e., $\Delta Y/\Delta Z = 2.1 \pm 0.9$). Balser (2006) published $\Delta Y/\Delta Z = 1.6$, obtained using metal–poor Galaxy H II regions, Magellanic cloud H II regions, and M17 abundances while taking into account the effects of temperature fluctuations. Interestingly, when using only the Galaxy H II region S206 and M17, Balser (2006) found $\Delta Y/\Delta Z = 1.41 \pm 0.62$, a value reported to be consistent with that from standard chemical evolution models. Depending on the choice of solar composition, Serenelli and Basu (2010) reported the initial helium abundance of the Sun to be in agreement with a slope of $1.7 \leq \Delta Y/\Delta Z \leq 2.2$. In general, acceptable values of the helium enrichment ratio are within the range $1 \leq \Delta Y/\Delta Z \leq 3$. *In this thesis, I employ equation 3.5 to determine the initial helium values when constructing stellar grids. The values of* $\Delta Y/\Delta Z$ *are chosen ensuring that they lie within the accepted range.*

Therefore, the treatment of the initial helium mass fraction in stellar evolution grids is a potential source of systematic uncertainties on stellar properties derived using

forward modelling techniques. To quantify the systematic uncertainties arising from the choice of the helium to heavy element ratio adopted in establishing the relationship between Y and Z, I constructed two stellar grids with the same physics but only varying in the choice of $\Delta Y/\Delta Z$ (i.e., 1.4 and 2.0 for grid A and B, respectively). I generated the corresponding model frequencies using GYRE. Considering a sample of 66 *Kepler* Legacy stars (Silva Aguirre et al., 2017, Lund et al., 2017), Mr. Nuno Moedas (a master's student at the University of Porto) applied AIMS (discussed in Sect. 3.2.5) and determined the systematic uncertainties on the inferred stellar parameters. Figure 3.5

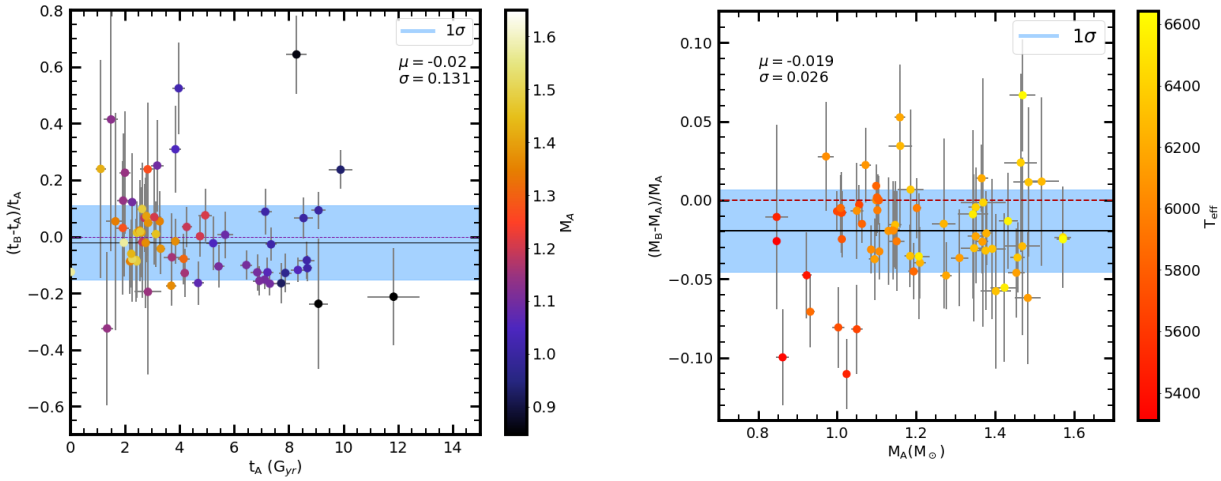

Figure 3.5: Fractional differences in stellar age (left panel) and stellar mass (right panel) as a function of stellar age and stellar mass, respectively. The subscripts denote the stellar parameters from the two grids, A and B. The blue region shows the scatter (σ) and the bias is represented by the red dotted line. See text for details.

shows the preliminary results for the fractional differences in the optimal stellar age and mass from the two grids. A scatter of $\sim 2.6\%$ and $\sim 13\%$ in mass and age, respectively, was found. The preliminary findings show that the systematic uncertainties in mass are consistent with findings of Valle et al. (2014), which were based on synthetic data of about 10,000 artificial stars, yielding systematic uncertainties in mass of 2.3% arising from a variation of ± 1 in $\Delta Y/\Delta Z$. Lebreton and Goupil (2014) carried out a detailed study of characterising CoRoT's exoplanet host HD 52265 and reported a scatter of about 5 % in mass arising from the treatment of the initial helium mass fraction. This value is higher than that found by Nuno and Valle et al. (2014), probably because of the difference in the target sample size.

3.1.3 Nuclear reactions

The nuclear reaction processes through which chemical elements in stellar interiors are transformed depend on the stellar mass and evolution stage. Low–mass stars (i.e., below 1.1 $M_{\odot}$) have relatively low temperatures which favour the proton–proton (pp) chain (e.g., Kippenhahn et al. 2012), while high–mass stars (i.e., above 1.1 $M_{\odot}$) have high temperatures which favour the Carbon–Nitrogen–Oxygen cycle (CNO). In addition, the rates of nuclear energy generation (ϵ) in the pp chain and CNO cycle are given as

$$\epsilon_{\rm pp} \propto T^4 \ , \tag{3.6}$$

$$\epsilon_{\rm CNO} \propto T^{18} \ , \tag{3.7}$$

where $T \simeq 4 \times 10^6$ K for the pp chain and $T \geq 16 \times 10^6$ K for the CNO cycle (e.g., Reid and Hawley 2005). This also indicates that ϵ is extremely dependent on the stellar interior conditions, with the CNO cycle being dominant in stars with convective cores and with the pp chain dominating in stars with radiative cores.

During the conversion of hydrogen to helium, the pp chain has three network reactions, namely, ppI, ppII, and ppIII, among which ppI is the most dominant since it simply requires the reaction of two protons to form deuterium, i.e.,

$$^1\mathrm{H} + ^1\mathrm{H} \longrightarrow {}^2\mathrm{H} + e^+ + \nu$$

$$^2\mathrm{H} + ^1\mathrm{H} \longrightarrow {}^3\mathrm{He} + \gamma$$

$$^3\mathrm{He} + ^3\mathrm{He} \longrightarrow {}^4\mathrm{He} + ^1\mathrm{H} + ^1\mathrm{H} \ ,$$

where e^+ is a positron (i.e., a subatomic particle with the same mass as an electron and a numerically equal but positive charge), γ is a gamma ray (very high energy photon), and ν is a neutrino. Please refer to Pols (2011), Kippenhahn et al. (2012) for the chemical reaction equations of ppII and ppIII. The CNO cycle converts hydrogen into helium via a sequence of nuclear reactions given as:

$$^{12}\mathrm{C} + ^1\mathrm{H} \longrightarrow {}^{13}\mathrm{N} + \gamma$$

$$^{13}\mathrm{N} \longrightarrow {}^{13}\mathrm{C} + e^+ + \nu$$

$$^{13}\mathrm{C} + ^1\mathrm{H} \longrightarrow {}^{14}\mathrm{N} + \gamma$$

$$^{14}\mathrm{N} + ^1\mathrm{H} \longrightarrow {}^{15}\mathrm{O} + \gamma$$

$$^{15}\mathrm{O} \longrightarrow {}^{15}\mathrm{N} + e^{+} + \nu$$

$$^{15}\mathrm{N} + {}^{1}\mathrm{H} \longrightarrow {}^{12}\mathrm{C} + {}^{4}\mathrm{He}\ .$$

In stellar evolution codes (based on my experience with the MESA evolution code), reaction rates are supplied in table form and interpolated. A vital reaction that has a significant influence on the existence of a convective core in a stellar model is the $^{14}\mathrm{N}(p,\gamma)^{15}\mathrm{O}$ reaction. In stars in which the CNO cycle is the main energy production process, this reaction determines their evolutionary timescales. Furthermore, a reduction in this reaction results in a reduction in the total energy generation rate. This is because the $^{14}\mathrm{N}(p,\gamma)^{15}\mathrm{O}$ reaction has a relatively significant contribution to the total energy generated, i.e., $\sim$ 7.3 MeV (e.g., Bazot et al. 2016). A number of nuclear reaction rates are available in the literature with significant differences in the $^{14}\mathrm{N}(p,\gamma)^{15}\mathrm{O}$ reaction. These include: the NACRE (Nuclear Astrophysics Compilation of Reaction Rates; Angulo et al. 1999) collaboration, newer NACRE reaction rates provided by Adelberger et al. (2011) which yield a lower $^{14}\mathrm{N}(p,\gamma)^{15}\mathrm{O}$ reaction rate compared to Angulo et al. (1999), LUNA reaction rates (Formicola et al., 2003, 2004) which employ the $^{14}\mathrm{N}(p,\gamma)^{15}\mathrm{O}$ reaction by Imbriani et al. (2005), and JINA REACLIB (Joint Institute for Nuclear Astrophysics Reaction Library) version 2.2 (Cyburt et al., 2010) which also employs the $^{14}\mathrm{N}(p,\gamma)^{15}\mathrm{O}$ reaction by Imbriani et al. (2005). The difference in $^{14}\mathrm{N}(p,\gamma)^{15}\mathrm{O}$ reaction rates provided by the different nuclear reaction rate libraries highly affect the average collision rate for this reaction, with a lower collision rate greatly reducing the chances of a stellar model developing a convective core or having convection has a major energy transport process in its core (e.g., Magic et al. 2010).

It is worth noting that there is a transition region between 1.1 $\mathrm{M}_{\odot}$ and 1.15 $\mathrm{M}_{\odot}$ for models constructed at solar metallicities across which convective cores develop while on the main–sequence. Therefore, the choice of nuclear reaction rates has a significant influence on triggering the onset of the CNO cycle as the dominant energy production process, favouring the existence of a convective core in models with masses in the range 1.1 - 1.15 $\mathrm{M}_{\odot}$. α Centauri A has been of interest to stellar modellers for decades, mainly because it has been reported to have a dynamical mass within this transition region (Pourbaix et al., 2002, Pourbaix and Boffin, 2016, Kervella et al., 2017) — a potential benchmark for testing the impact of model physics for stars within this transition region.

In this thesis, I explored the physics that could affect the chances of a star (in particular α Centauri A) developing a convective core. The contribution from nuclear reaction rates is discussed in Chapter 5.

3.2 Determination of stellar parameters

Apart from being applied in exploring the stellar interior physics, asteroseismology of solar–type stars yields precise fundamental stellar parameters such as the mean density, radius, mass, age, and surface gravity (e.g., Miglio and Montalbán 2005, Metcalfe et al. 2012, 2014, Mathur et al. 2012, Silva Aguirre et al. 2013, Lebreton and Goupil 2014, Silva Aguirre et al. 2015, Davies et al. 2016). Asteroseismic techniques are also currently being employed in the characterisation of exoplanet–hosts and their planetary systems. For instance, when an independent effective temperature is known, a precise stellar radius can be derived and adopted in determining the absolute planetary sizes from transit photometry (Huber et al. 2013, Benomar et al. 2014, Marcy et al. 2014, Campante et al. 2016). The planetary mass can be estimated for bright systems when radial–velocity observations are combined with transit data. Asteroseismology also provides the stellar mass which can be adopted to infer the planetary mass according to $M_{\rm p} \propto M^{2/3}$ (e.g. Perryman, 2014, Campante et al., 2017). Last but not least, stellar ages from asteroseismology can potentially be used to assess the dynamical stability of planetary systems and to establish their relative chronology. In this section, I describe the different asteroseismic approaches employed in deriving stellar parameters, with emphasis directed towards the method used in this thesis.

3.2.1 Asteroseismic scaling relations

The acoustic modes (p modes) follow a distinct pattern (see top panel of Fig. 3.6) described by the asymptotic relation given in equation 1.7. Two essential global asteroseismic parameters contain information required in the determination of stellar parameters. These are, the large separation ($\Delta\nu$) and the frequency of maximum power ($\nu_{\rm max}$). The large separation is referred to as the separation between modes of the same spherical degree (l) and consecutive radial order (Ulrich, 1986). This is expressed as

$$\Delta\nu = \nu_{n,l} - \nu_{n-1,l} \ . \tag{3.8}$$

This is illustrated in the bottom panel of Fig. 3.6. The large separation is also a measure of the inverse sound speed travel time across a stellar diameter (see equation 1.9). Further, it also scales as the square root of the mean density as shown in equation 1.10. Expressing $\Delta\nu$ in terms of stellar mass, M, and radius, R, gives (Ulrich, 1970, Tassoul, 1980, Kjeldsen and Bedding, 1995):

$$\Delta\nu \propto \sqrt{\frac{M}{R^3}} \ . \tag{3.9}$$

The top panel of figure 3.6 shows the power spectrum of the Sun with a fitted Gaussian whose centroid yields the frequency of maximum power ($\nu_{\rm max}$). I note that all solar–like oscillators have oscillations with a comb–like structure and bell–shaped power excess located above the granulation profile. Oscillation frequencies higher than a particular threshold value (known as the acoustic cut–off frequency, $\nu_{\rm ac}$) are no longer trapped and propagate as running waves into the upper atmosphere of the star. The acoustic cut–off frequency is given as (Lamb, 1932)

$$\nu_{\rm ac} \propto \frac{c}{H_{\rm p}} \ , \tag{3.10}$$

where c is the sound speed and $H_{\rm p}$ is the pressure scale height of the atmosphere. $\nu_{\rm max}$ approximately scales with the acoustic cut–off frequency (Brown et al. 1991, Kjeldsen and Bedding 1995), which is suggested to scale as the stellar surface gravity, g, and effective temperature, $T_{\rm eff}$, (Brown et al., 1991, Kjeldsen et al., 2005), i.e.,

$$\nu_{\rm ac} \propto \nu_{\rm max} \propto g T_{\rm eff}^{-1/2} \ . \tag{3.11}$$

The relation shown in equation 3.11 has been tested in different asteroseismic studies and shown to hold reasonably well (e.g., Chaplin and Miglio 2013, Coelho et al. 2015 and references therein). Combining equation 3.9 and equation 3.11, and taking into account the solar values for the seismic parameters, $\Delta\nu_{\odot} = 135.1$ μHz and $\nu_{\rm max,\odot} = 3090$ μHz (Chaplin et al., 2014) as a reference, yields the following asteroseismic scaling relations (e.g., Kjeldsen and Bedding 1995):

$$\frac{R}{\rm R_{\odot}} \approx \left(\frac{\nu_{\rm max}}{\nu_{\rm max,\odot}}\right)\left(\frac{\Delta\nu}{\Delta\nu_{\odot}}\right)^{-2}\left(\frac{T_{\rm eff}}{T_{\rm eff,\odot}}\right)^{1/2} \ , \tag{3.12}$$

and

$$\frac{M}{\rm M_{\odot}} \approx \left(\frac{\nu_{\rm max}}{\nu_{\rm max,\odot}}\right)^{3}\left(\frac{\Delta\nu}{\Delta\nu_{\odot}}\right)^{-4}\left(\frac{T_{\rm eff}}{T_{\rm eff,\odot}}\right)^{3/2} \ . \tag{3.13}$$

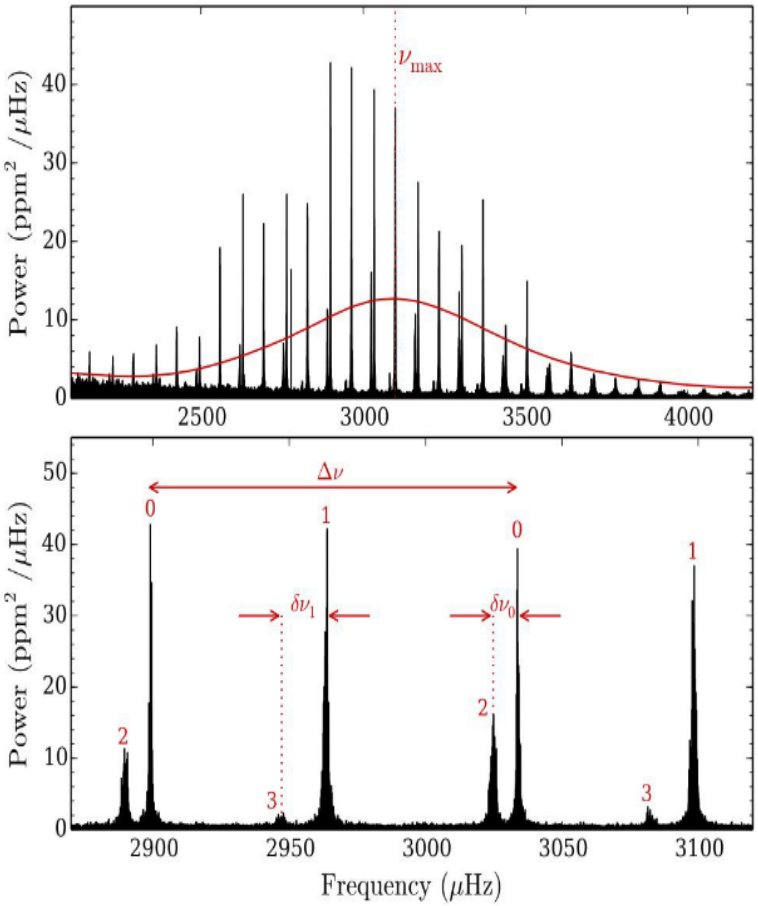

Figure 3.6: Fourier spectrum of the Sun based on data from VIRGO/SPM on the SOHO satellite (Fröhlich et al., 1995, Jiménez et al., 2002). Top panel: Bell–shaped signature of the p mode oscillations. The red line represents a Gaussian fit to the oscillations envelope whose centroid corresponds to ν_{max}. Bottom panel: Close–up of the top panel showing the different spherical degrees, large separation, $\Delta\nu$, and the small separations, i.e., $\delta\nu_1$ and $\delta\nu_0$. Figure taken from Bedding and Kjeldsen (2003).

When T_{eff} is available, the asteroseismic scaling relations yield model independent stellar masses and radii (e.g., Stello et al. 2008, Silva Aguirre et al. 2011b). Furthermore, direct estimates of the surface gravity and stellar mean density can be derived from equation 3.9 and equation 3.11, respectively. This approach of determining stellar parameters is sometimes known as the "direct method". The asteroseismic scaling relations have been prominently adopted in estimating stellar parameters of large catalogues, e.g., Chaplin et al. (2014). Scaling relations are advantageous in that the global asteroseismic parameters are measurable even in situations of low signal–to–noise data or in cases of short–cadence data. The setback of using scaling relations is that they do not provide any information on the interior stellar physics such as mixing

processes like convection, semi–convection, convective overshooting etc. In order to have a handle on stellar interior physics, one has to resort to stellar models as described in Sect. 3.2.2 and Sect. 3.2.3.

3.2.2 Grid–based modelling

The asteroseismic scaling relations shown in equation 3.12 and equation 3.13 can be employed to translate a grid of stellar model properties (namely, radius, mass, and effective temperature) into the expected values of model asteroseismic parameters, i.e., $\Delta\nu$ and $\nu_{\rm max}$. These model asteroseismic parameters are compared to those from observations. In a nutshell, a grid–based modelling approach involves a search among a pre–computed grid of stellar evolution models to generate a set of models whose asteroseismic parameters and/or classical (atmospheric) parameters such as luminosity, metallicity, and effective temperature match the observed stellar parameters within the specified observational uncertainties. This approach has been widely employed in asteroseismic studies, e.g., Basu et al. (2010), Miglio et al. (2012), Huber et al. (2013), Chaplin et al. (2014), Casagrande et al. (2014), Lundkvist et al. (2014), Coelho et al. (2015), among others.

The use of stellar evolution models in grid–based modelling allows one to infer stellar interior physics, helping to take a step forward towards our understanding of the physical processes taking place in stellar interiors. Although grid–based modelling has been widely used in estimating stellar parameters, the robustness of the asteroseismic scaling relations have been questioned and therefore put to test in various studies, with comparisons to the properties determined from interferometric measurements, parallaxes, and binaries, e.g., Huber et al. (2012), White et al. (2013), Coelho et al. (2015). Furthermore, although the $\Delta\nu$ relation in equation 3.8 is based on a firm theoretical foundation, the scaling relation for $\nu_{\rm max}$ remains mostly an empirical relation and its detailed understanding still needs further exploration (Brown et al., 1991, Kjeldsen and Bedding, 1995, Chaplin and Miglio, 2013). Coelho et al. (2015) carried out a detailed test of the $\nu_{\rm max}$ scaling relation in equation 3.11 for a set of main–sequence and subgiant stars observed by the NASA *Kepler* mission. They reported that the $\nu_{\rm max}$ scaling holds at the level of 1.5% in the temperature range of 5400 K to 7000 K. Chaplin et al. (2014) reported that the inferred stellar radius and mass through grid–based modelling hold to levels of about 4% and 10%, respectively. For more evolved stellar evolution phases, e.g., the red–giant phase, scaling relations are reported to perform even worse compared to main–sequence stars. For instance, it is possible to have stars at the hydrogen–shell burning and helium–core burning

phases with the same mass and radius (i.e., same mean density) but different large separation (this is attributed to differences in the sound–speed profile in the outer layers) —, implying a different relation for equation 3.9 (refer to Miglio et al. 2012 for details). Despite the fact that grid–based modelling relying on the asteroseismic scaling relations yields seemingly robust stellar parameters, the quest for detailed insights and exploration of stellar physics are currently the research direction taken by the majority of stellar modellers. This requires additional information from observations as discussed in Sect. 3.2.3.

3.2.3 à la carte modelling

This approach is also referred to as "boutique modelling", which typically means using stellar evolution models to make asteroseismic inferences on a star by star case. This approach involves matching a grid of stellar evolution model properties, i.e., seismic and classical parameters, to the observed stellar parameters. The seismic parameters employed in this approach are usually the individual oscillation frequencies, ν, which contain essential information about the stellar interior structure. This approach of stellar modelling not only yields highly precise stellar parameters, but it also paves the way for stellar model physics to be tested — and its description in stellar evolution codes improved. Silva Aguirre et al. (2015) reported the median statistical uncertainties for the stellar parameters of a sample of *Kepler* exoplanet–host stars derived by means of à la carte modelling to be 1.2% in radius, 1.7% in density, 3.3% in mass, and 4.4% in age. Furthermore, a variety of studies have employed this approach of stellar modelling and explored stellar physics, e.g., Metcalfe et al. (2009), Gruberbauer et al. (2012), Silva Aguirre et al. (2015), Verma et al. (2019), among others.

In order to explore the implication of stellar physics on the inferred stellar parameters highly precise sets of observables are required, therefore, à la carte modelling is mainly applied for stars with high signal–to–noise observations. In this thesis, the majority of the sample stars adopted are part of the *Kepler* Legacy sample (Lund et al., 2017) with at least 12 months of observations. I stress that the à la carte modelling employed in this thesis is similar to the grid–based modelling approach described in Sect. 3.2.2 which employs $\nu_{\rm max}$ and $\Delta\nu$ as seismic observables, but instead individual oscillation frequencies are adopted as seismic observables. Furthermore, the seismic constraints in this thesis are complemented with spectroscopic constraints (namely effective temperature and metallicity) and interferometric radius measurements when available. The combination of these observables presents an opportunity of tightly constraining stellar models, setting a platform for examining the impact of the adopted

model physics on the derived stellar parameters. *A setback of using individual oscillation frequencies as seismic observables is due to the known offset between observed and model oscillation frequencies. This is caused by a number of reasons, which are detailed in Sect. 3.2.4.*

3.2.4 Surface effect and correction methods

The major hindrances to directly comparing observed oscillation frequencies to theoretical model frequencies is the systematic difference that exists between observations and models attributed to the improper modelling of the near–surface layers. Figure 3.7 shows the frequency shifts produced by a number of neglected or poorly described physical processes known as the "surface effect". It is evident that the largest discrepancies occur at high frequencies, which are more prone to surface effects. The contributions to the surface effect include:

— The adiabatic approximation assumption made during the computation of oscillation frequencies, which does not hold in the near–surface layers.

— The treatment of convection based on the standard prescription of Böhm-Vitense (1958) is valid in the deep stellar interior convective zone where convection is efficient, however, this implementation of convection does not work very well in the near–surface super–adiabatic layers. Furthermore, the description of the interaction between stellar oscillations and convection is still not properly understood.

— In addition, the implementation of very simple stellar atmosphere models and uncertainties in microphysics inputs such as low–temperature opacities create limitations on modelling the near–surface layers.

— I also assume the stellar structure to be spherically symmetric implying that magnetic fields and rotational forces that could alter the stellar structure equilibrium state are not considered.

All these accumulate into to the frequency differences shown in figure 3.7. To correct for these systematic differences between the observed and theoretical frequencies, various formulations have been devised. I give a brief description of these methods and I refer the reader to the respective cited works for the details of these surface correction methods.

(i) Kjeldsen et al. (2008) proposed the first empirical correction for the offset between the observed and theoretical frequencies. They found these differences to be well

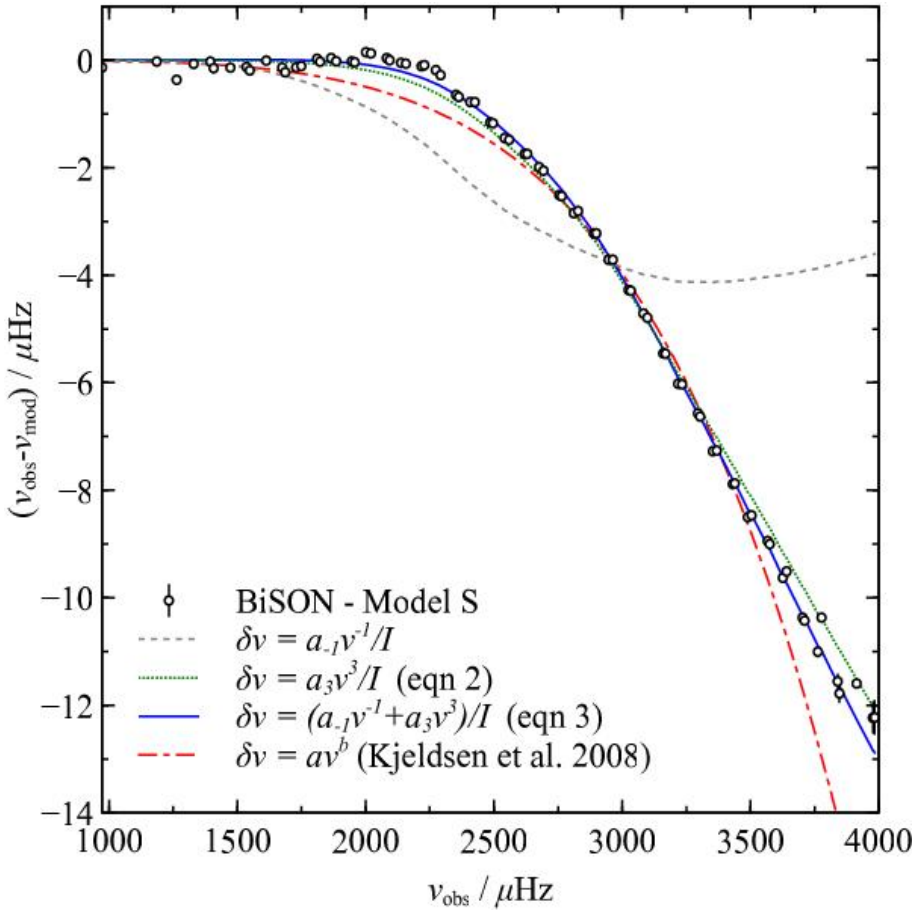

Figure 3.7: Differences between observed and theoretical mode frequencies for the Sun. Solar model S is from Christensen-Dalsgaard et al. (1996). The different empirical surface correction relations are indicated in different colours in the legend. Figure taken from Ball and Gizon (2014). See text for details.

described/fitted by a power law:

$$\delta\nu = a\left(\frac{\nu_{\mathrm{obs}(n)}}{\nu_0}\right)^b , \tag{3.14}$$

where $\delta\nu$ is the frequency difference, a and b are parameters to be determined, ν_0 is the reference frequency which is usually ν_{max}, and ν_{obs} corresponds to the observed frequencies. This was developed based on the Sun and found to be successful in correcting the frequency offset in other stars such as α Centauri A and B, and β Hyi (see Kjeldsen et al. 2008 for details). I note that there is no physical justification given by Kjeldsen et al. (2008) as to why the frequency differences are described by a power law function.

(ii) Ball and Gizon (2014) proposed two empirical corrections based on the description of the functional form of frequency shift/differences suggested by Gough (1990). It is proposed that a change in the description of convection would cause a perturbation which may modify the pressure scale height, causing a frequency shift proportional to ν^{-1}/I, where I is the mode inertia. This is commonly referred to as the inverse term (or first term) and is expressed as (Ball and Gizon, 2014)

$$\delta\nu = a_1 \frac{\nu^{-1}}{I} \ , \tag{3.15}$$

where a_1 is a parameter to be determined. In addition, the sound speed is modified by perturbations caused by a magnetic field yielding frequency shifts proportional to ν^3/I (Gough, 1990, Goldreich et al., 1991). This is commonly referred to as the cubic term/second term, expressed as (Ball and Gizon, 2014)

$$\delta\nu = a_3 \frac{\nu^3}{I} \ , \tag{3.16}$$

where a_3 is a parameter to be determined. The combination of the inverse term and the cubic term yields a combined surface term expressed as (Ball and Gizon, 2014)

$$\delta\nu = \frac{1}{I}\left(a_1\nu^{-1} + a_3\nu^3\right) \ . \tag{3.17}$$

The normalised mode inertia (I) is defined as (Aerts et al., 2010):

$$I = \frac{4\pi \int_0^R \left[|\xi_r(r)|^2 + l(l+1)|\xi_h(r)|^2\right] \rho r^2 dr}{M\left[|\xi_r(R)|^2 + l(l+1)|\xi_h(R)|^2\right]} \ , \tag{3.18}$$

where ξ_r and ξ_h are the radial and horizontal components of the displacement eigenvector. M is the total mass, l is the spherical degree, ρ is the unperturbed stellar density, and R is the photospheric radius.

(iii) Sonoi et al. (2015) analysed frequency differences between patched models (i.e., models whose outer–layers are replaced with 3D hydrodynamical simulation layers) and standard models. They carried out an extensive testing of the empirical correction suggested by Kjeldsen et al. (2008) shown in equation 3.14 and found the fitting coefficients to the frequency differences to vary significantly across the H–R diagram — equation 3.14 should not be calibrated against the Sun but constrained through realistic physical modelling such as 3D hydrodynamical simulations. Furthermore, as the frequency exceeds $\nu_{\rm max}$, the profile of the

frequency differences becomes less steep confirming that the power law suggested by Kjeldsen et al. (2008) is not suitable in the high–frequency regime. Sonoi et al. (2015) suggested a modified Lorentzian correction which was found to be successful in fitting the frequency differences across the whole frequency range, with a formulation expressed as

$$\delta\nu = S_0 \left[1 - \frac{1}{(1+\nu_s)^{S_1}} \right] , \tag{3.19}$$

where S_0 and S_1 are parameters to be fitted, $\nu_s = \nu_{\rm model}/\nu_{\rm max}$. I also note that equation 3.19 reduces to equation 3.14 at the low–frequency limit.

Apart from the empirical corrections to the frequency differences suggested above, Roxburgh and Vorontsov (2003) proposed frequency ratios that effectively suppress most of the contributions from the poorly modelled surface layers and allow for a direct comparison of theoretical model frequencies and observed frequencies:

$$r_{02}(n) = \frac{\delta_{02}(n)}{\Delta\nu_1(n)} , \tag{3.20}$$

$$r_{01}(n) = \frac{\delta_{01}(n)}{\Delta\nu_1(n)}, \quad r_{10}(n) = \frac{\delta_{10}(n)}{\Delta\nu_0(n+1)} , \tag{3.21}$$

where $\delta_{02}(n) = \nu_{n,0} - \nu_{n-1,2}$ is the small frequency separation, $\delta_{01}(n)$ and $\delta_{10}(n)$ are similar small frequency separations defined as

$$\delta_{01}(n) = \frac{1}{8}(\nu_{n-1,0} - 4\nu_{n-1,1} + 6\nu_{n,0} - 4\nu_{n,1} + \nu_{n+1,0}) , \tag{3.22}$$

$$\delta_{10}(n) = -\frac{1}{8}(\nu_{n-1,1} - 4\nu_{n,0} + 6\nu_{n,1} - 4\nu_{n+1,0} + \nu_{n+1,1}) . \tag{3.23}$$

These are known to constrain stellar interiors, thus yielding precise stellar ages compared to adopting other sets of observables.

In this thesis, I explore the systematic uncertainties on the derived stellar parameters (namely, mean density, radius, mass, and age) arising from the variations in the different surface correction routines adopted during the optimisation process.

3.2.5 Asteroseismic Inference on a Massive Scale (AIMS)

An essential aspect of asteroseismic forward modelling inference deals with the comparison of stellar observations with stellar model parameters. A number of seismic optimisation tools have been developed by different asteroseismology teams so as to handle large amounts of data from space missions such as NASA's *Kepler*, NASA's TESS, and the future ESA's PLATO, in a fast, robust, and stable manner. Furthermore, seismic tools are designed to take into account all the information available in the individual oscillations, e.g., acoustic glitches[2] (Verma et al., 2017). A majority of the seismic optimisation tools rely on a Bayesian approach or on machine learning techniques to find a representative set of models, e.g., Bazot et al. (2008), Gruberbauer et al. (2012), Silva Aguirre et al. (2015), and Bellinger et al. (2016). Most of the seismic tools rely on a pre–computed grid of stellar models, e.g., Silva Aguirre et al. (2015), and thus are computationally faster compared to those that carry out on–the–fly model calculations with a Markov chain Monte Carlo (MCMC) algorithm, e.g., Bazot et al. (2008).

In this thesis, a new seismic optimisation tool — Asteroseismic Inference on a Massive Scale (AIMS; Lund and Reese 2018, Rendle et al. 2019) — is employed to fit the different sets of observables such as individual oscillation frequencies, supplemented with classical constraints, and interferometric constraints. This optimisation tool is based on Bayesian techniques to find probability distribution functions (PDFs) of various stellar parameters, such as radius, mass, age, central hydrogen abundance, among others. AIMS is based on a pre–defined grid of stellar models to generate a subsample of models that are representative of a set of classical and asteroseismic constraints. AIMS uses a Markov chain Monte Carlo (MCMC) algorithm based on Foreman-Mackey et al. (2013) together with interpolation based on a Delaunay tessellation of the stellar grid. In a nutshell, the MCMC algorithm is employed to generate samples based on the distribution of interest, i.e., $p(A|O)$ shown in equation 3.24. In order to increase the efficiency of the grid parameter space exploration and enhance faster convergence, AIMS initialises the grid search in the region having a set of models with the highest posterior probability.

[2] A glitch is the abrupt variation in the sound speed due to a sharp change in the stellar internal structure. Regions where the sound speed may undergo a sharp variation include: the base of the convective zone, the helium second ionization zone, among others.

With A representing different stellar parameters and O various asteroseismic and classical observables, from Bayes's theorem one has (e.g., Gregory 2005):

$$p(A|O) \propto p(O|A)\, p(A) \ , \tag{3.24}$$

where $p(A)$ represents my prior assumptions. I assign uniform prior distributions to parameters defining the stellar model grid such as mass, initial metal mass fraction, mixing length parameter, among others. The likelihood of obtaining a set of observables given a set of model parameters is expressed as

$$p(O|A) = \frac{1}{(2\pi)^{\frac{1}{2}}\sqrt{|C|}} \exp(-\chi^2/2) \ , \tag{3.25}$$

where C is the covariance matrix of the observed parameters (see, e.g., the book by Gregory 2005). Unless otherwise specified, in most cases, I assumed Gaussian distributed errors on the sets of observables (i.e., individual oscillation frequencies, effective temperature, metallicity, and interferometric radius when available). The χ^2 for a set of independent variables is defined as

$$\chi^2 = \sum_{i=1}^{N} \left(\frac{O_i - \theta_i}{\sigma_i} \right)^2 \ , \tag{3.26}$$

where O_i, θ_i, and σ_i are the observed value, modelled value, and the associated observed uncertainties, respectively. In cases where frequency ratios are used, correlations will be introduced that are a function of frequency. This is taken into consideration in the likelihood function (see equation 3.25) and, in this case, the χ^2 of each model is given by (e.g., Gregory 2005)

$$\chi^2 = (O - \theta)^T C^{-1} (O - \theta) \ . \tag{3.27}$$

I stress that the frequency ratios used in this thesis were calculated internally by AIMS. The frequency ratios were complemented with the large frequency separation calculated from $l = 0$ modes. I note that the different stellar parameters and their uncertainties are finally obtained from the statistical mean and standard deviation of the generated posterior PDFs.

The interpolation routine and tests regarding the accuracy of the interpolation have been extensively carried out in Rendle et al. (2019) and discussed in the complementary AIMS documentation[3]. I briefly highlight them here. In order to inspect the properties

[3]https://github.com/benrendle/AIMS

of regions between models, AIMS carries out the interpolation process in two steps, namely: (i) interpolation between evolutionary tracks and (ii) interpolation along the evolutionary tracks. The interpolation along the evolutionary tracks involves linear interpolation in age between the two closest models, while excluding points outside the grid. I note that AIMS does not carry out extrapolation. The determined coefficients are adopted to interpolate the models by linearly combining the global model parameters density, ρ, effective temperature, $T_{\rm eff}$, initial metal mass fraction, Z_0, initial hydrogen mass fraction, X_0, and mass, M. I note that the radius, R, and luminosity, L, are determined based on the interpolated parameters following the expressions

$$R = \left(\frac{3M}{4\pi\rho}\right)^{1/3} , \tag{3.28}$$

$$L = 4\pi\sigma R^2 T_{\rm eff}^4 , \tag{3.29}$$

where σ is the Stefan–Boltzmann law. In addition, the model non–dimensional frequencies, $\omega/\sqrt{GM/R^3}$, with the same n and l are interpolated linearly. M and R are the interpolated mass and radius. Interpolation between evolutionary tracks relies on a multidimensional Delaunay tessellation of the grid parameters (such as mass, metallicity, mixing length parameter etc) excluding model age. AIMS handles interpolation between evolutionary tracks by first creating a new tessellation from half of the evolutionary tracks chosen randomly, and then interpolates to the remaining tracks. I note that the evolutionary tracks which fall outside the new tessellation are not included in the interpolation process.

3.2.6 Application: Modelling the Sun and the asteroseismic binary HD 176465

I demonstrate here the fitting capability of AIMS by applying it — using seismic and classical constraints (i.e., effective temperature, $T_{\rm eff}$, and metallicity, [Fe/H]) — to the Sun and the asteroseismic binary HD 176465. Our Sun is a star with well known stellar parameters and displays a rich spectrum of stochastic oscillation modes, and is thus used as benchmark for testing asteroseismic tools. I compare the solar results obtained when using AIMS with those obtained from different pipelines presented in Silva Aguirre et al. (2017). Furthermore, I demonstrate the ability of using AIMS to derive stellar parameters for stars other than the Sun — specifically the asteroseismic binary HD 176465 — and compare the results to those obtained using other asteroseismic pipelines in White et al. (2017). *I note that my findings when modelling the asteroseismic binary*

HD 176465 were published in a conference proceedings in the EPJ Web of Conferences in 2017, volume 160, page 05010.

As mentioned earlier, AIMS requires a pre–calculated grid of stellar models and their corresponding oscillation frequencies, which I generated using MESA and GYRE, respectively. I evolved evolutionary tracks from the pre–main–sequence (PMS) and kept only stellar models starting from the zero–age main–sequence (ZAMS), which I define as the region along the evolutionary tracks where the nuclear luminosity is approximately 99% of its total luminosity. The evolutionary tracks were terminated when they reached 10 Gyr. The stellar grid varied in mass, $M \in [0.7 - 1.2]$ $M_\odot$ in steps of 0.05 $M_\odot$, $Z \in [0.004 - 0.04]$ in steps of 0.002, and $\alpha_{\rm mlt} \in [1.4 - 3.0]$ in steps of 0.2. Diffusion of hydrogen and gravitational settling of heavy elements were included based on the description of Thoul et al. (1994).

The general input physics used in the grid includes: Nuclear reaction rates obtained from JINA REACLIB version 2.2 (Cyburt et al., 2010) with specific rates for $^{12}C(\alpha,\gamma)^{16}O$ and $^{14}N(p,\gamma)^{15}O$ described by Kunz et al. (2002) and Imbriani et al. (2005), respectively. At high temperatures, OPAL tables (Iglesias and Rogers, 1996) were used to cater for opacities while tables from Ferguson et al. (2005) were used at lower temperatures. All the grids used the 2005 updated version of the OPAL equation of state (Rogers and Nayfonov, 2002). The surface boundary of stellar models was described using the standard Grey–Eddington atmosphere[4]. I employed the solar metallicity mixtures of Grevesse and Sauval (1998) with the surface solar metal mass fraction ($Z_\odot$) of 0.0169. The model oscillation frequencies for the spherical degrees, l = 0, 1, 2, and 3 were computed using GYRE (Townsend and Teitler, 2013). I note that the surface effect was corrected using the combined surface correction recipe of Ball and Gizon (2014) described in Sect. 3.2.3. The observed oscillation frequencies

Table 3.1: Solar properties determined using AIMS (shown in boldface) and different pipelines.

Tools	Mass ($M_\odot$)	Radius ($R_\odot$)	Age (Myr)	Density (g cm^{-3})
AIMS	**1.006 ± 0.011**	**1.001 ± 0.004**	**4861 ± 276**	**1.411 ± 0.003**
ASTFIT	0.986 ± 0.023	0.994 ± 0.008	4686 ± 393	1.411 ± 0.003
BASTA	$0.978^{+0.039}_{-0.030}$	$0.993^{+0.012}_{-0.012}$	4852^{+1181}_{-1069}	$1.411^{+0.021}_{-0.022}$
C2kSMO	1.021 ± 0.003	1.006 ± 0.010	4331± 85	1.412 ± 0.048
GOE	0.997 ± 0.006	0.995 ± 0.018	4859 ± 128	1.412 ± 0.002
YMCM	$1.037^{+0.031}_{-0.047}$	$1.012^{+0.005}_{-0.005}$	5297^{+350}_{-350}	$1.406^{+0.001}_{-0.001}$

[4]This integrates the atmosphere structure from the photosphere down to an optical depth of 10^{-4}.

and the classical constraints for the Sun and the asteroseismic binary HD 176465 were obtained from Lund et al. (2017) and White et al. (2017), respectively.

Table 3.1 shows the derived solar parameters obtained by the different seismic tools subject to the same sets of observables. I note that the tools in table 3.1 use different optimisation techniques and rely on stellar models with a variety of physics, which are described in detail in Silva Aguirre et al. (2017). Figure 3.9 shows the posterior PDFs

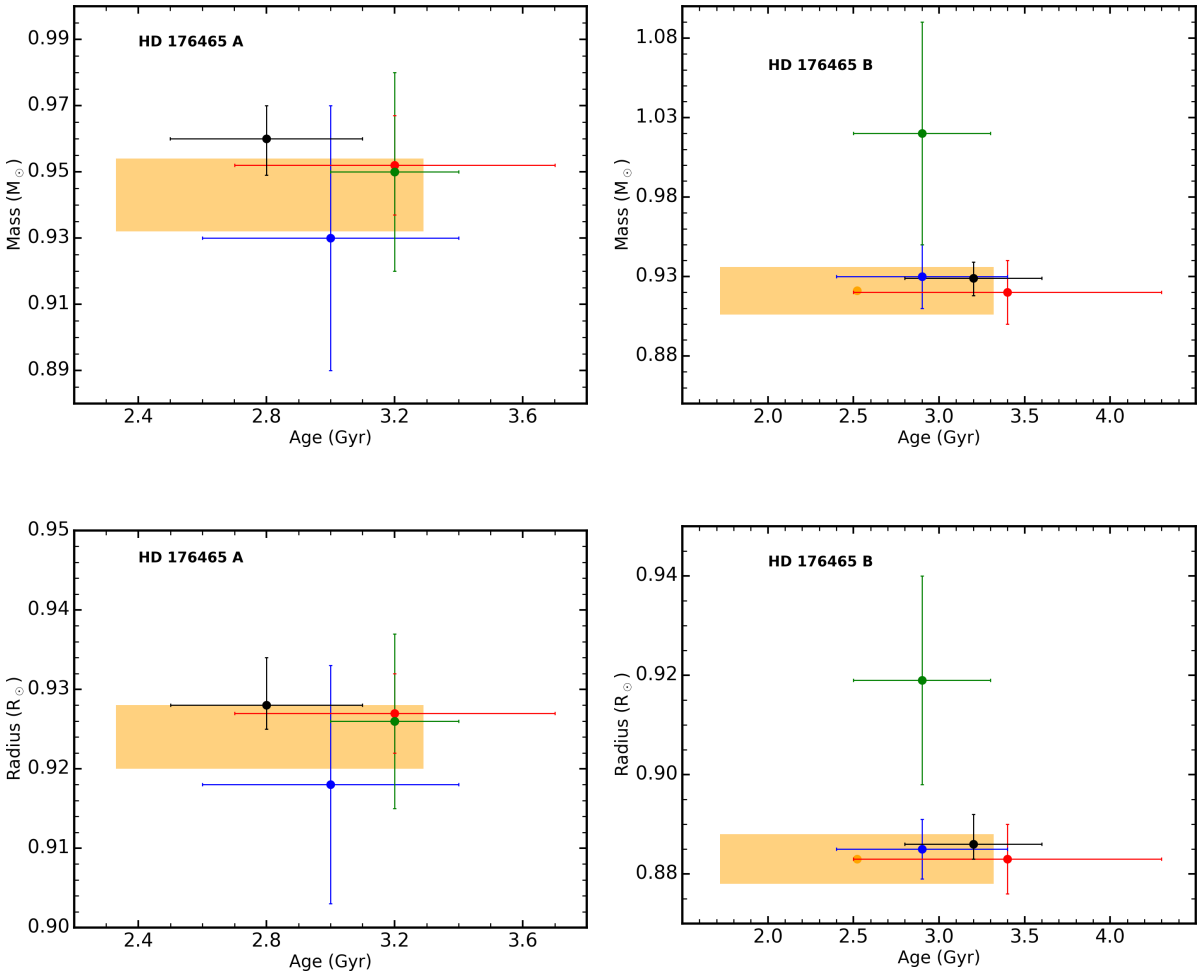

Figure 3.8: Comparison of stellar parameters derived using different astroseismic tools for the asteroseismic binary HD 176465. Top panel and bottom panel show the derived stellar mass and radius, respectively. Orange blocks correspond to 1σ–errors. ASTFIT results are shown in red, AMP in blue, MESA in green, and BASTA in black.

of the derived solar parameters generated using AIMS. The results obtained using AIMS are in agreement with those obtained from other seismic tools. Table 3.1 also shows that results from YMCM and C2kSMO yield large masses compared to other tools. In addition, YMCM yields a high value of the solar age mainly because atomic diffusion

was neglected in the stellar evolutionary models used. The stellar masses of HD 176465 A and HD 176465 B derived using AIMS are 0.943 ± 0.011 $M_{\odot}$ and 0.921 ± 0.015 $M_{\odot}$ with radii of 0.924 ± 0.004 $R_{\odot}$ and 0.883 ± 0.005 $R_{\odot}$, respectively. Figure 3.8 shows the comparison of these results to those derived using other asteroseismic tools applied in White et al. (2017). In general, results from the different asteroseismic tools are in agreement, however, those derived using the optimisation module in MESA yield higher mass and radius compared to other tools for HD 176465 B (see Fig. 3.8). The details of the fitting processes and model physics used in the different tools are discussed in detail in White et al. (2017). Interestingly, all different asteroseismic tools yield ages for both stars that agree within the uncertainties even though they were modelled as single stars without any restrictions to converge to the same age — satisfying the assumption of these stars being formed at approximately the same time. Furthermore, the metal mass fraction (Z) of HD 176465 A and HD 176465 B was found to be 0.012 ± 0.001 and 0.011 ± 0.001, respectively, — satisfying the assumption that these stars formed from the same molecular cloud. I note that some disagreements in the derived stellar parameters obtained using different asteroseismic tools exist. These are attributed to the difference in model physics and the optimisation techniques employed by the different tools. The systematic uncertainties arising from the different tools were handled in Silva Aguirre et al. (2015) and therefore are not addressed in this thesis.

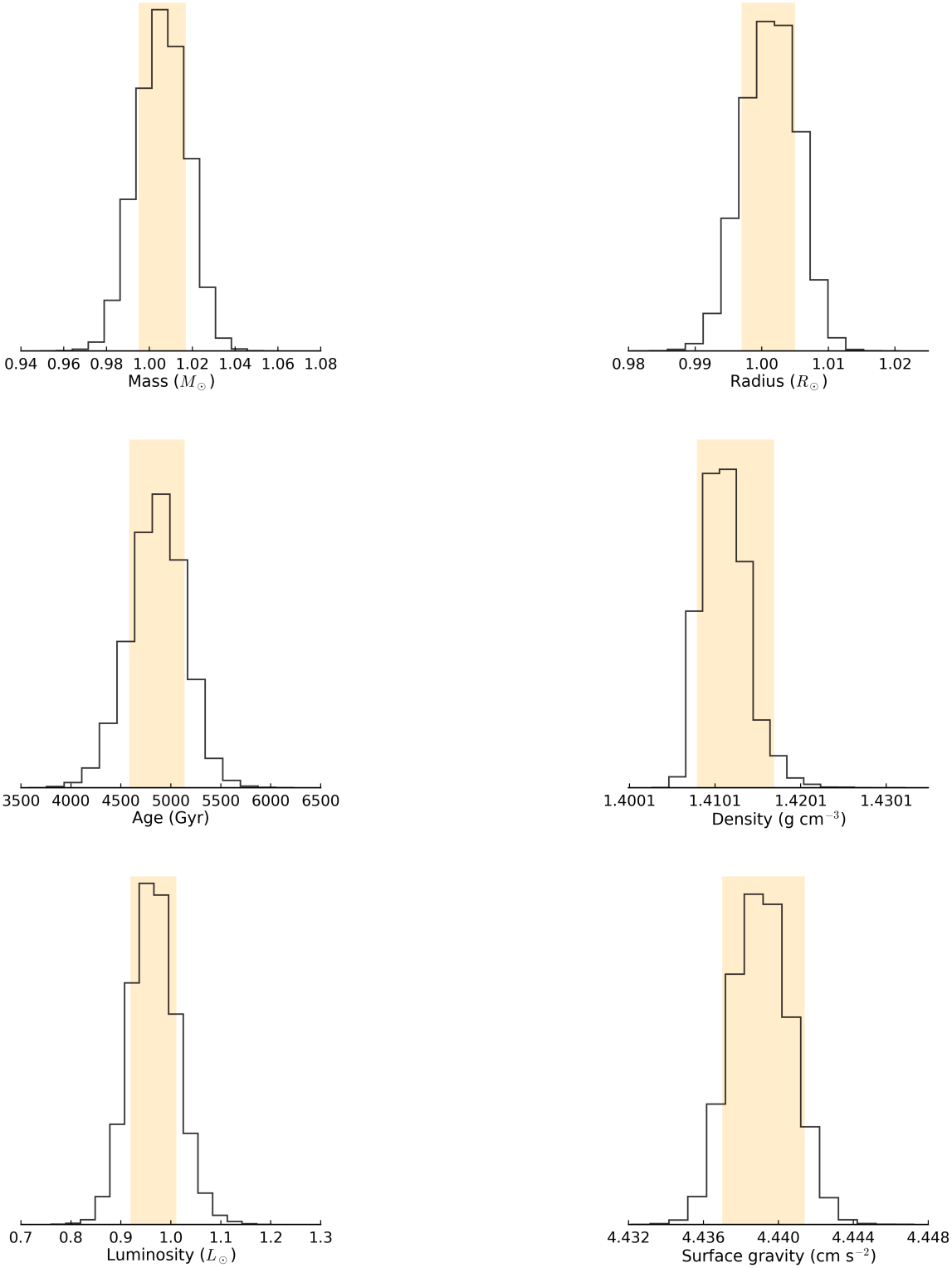

Figure 3.9: Posterior probability distributions of the solar parameters. The yellow bars show the 1–σ errors on the derived parameters.

Chapter 4

Internal systematics arising from input physics and surface correction methods

The content presented in this chapter was published in April of 2018 in *Monthly Notices of the Royal Astronomical Society*, volume 477, pages 5052–5063. This was authored by B. Nsamba, T. L. Campante, M. J. P. F. G. Monteiro, M. S. Cunha, B.M. Rendle, D. R. Reese, and K. Verma. The research work was carried out by me and was based on the objectives of this thesis. The text was written by myself with a substantial contribution from my fellow coauthors.

4.1 Chapter synopsis

Asteroseismic forward modelling techniques are being used to determine fundamental properties (e.g., mass, radius, and age) of solar–type stars. The need to take into account all possible sources of error is of paramount importance towards a robust determination of stellar properties. This study presents a sample of 34 solar–type stars for which high signal–to–noise asteroseismic data are available from multi–year *Kepler* photometry. We explore the internal systematics on the stellar properties, that is, associated with the uncertainty in the input physics used to construct the stellar models. In particular, we explore the systematics arising from: (i) the inclusion of the diffusion of helium and heavy elements; and (ii) the uncertainty in solar metallicity mixture. We also assess the systematics arising from (iii) different surface correction methods used in optimisation/fitting procedures. The systematics arising from comparing results

of models with and without diffusion are found to be 0.5%, 0.8%, 2.1%, and 16% in mean density, radius, mass, and age, respectively. The internal systematics in age are significantly larger than the statistical uncertainties. We find the internal systematics resulting from the uncertainty in solar metallicity mixture to be 0.7% in mean density, 0.5% in radius, 1.4% in mass, and 6.7% in age. The surface correction method by Sonoi et al. and Ball and Gizon's two–term correction produce the lowest internal systematics among the different correction methods, namely, ∼1%, ∼1%, ∼2%, and ∼8% in mean density, radius, mass, and age, respectively. Stellar masses obtained using the surface correction methods by Kjeldsen et al. and Ball and Gizon's one–term correction are systematically higher than those obtained using frequency ratios.

4.2 Introduction

Our knowledge of the underlying physical processes taking place in deep stellar interiors is of great importance for the accurate characterization of stars and classification of stellar populations. The treatment and choice of the essential model input physics such as solar metallicity mixture (Grevesse and Sauval, 1998, Asplund et al., 2009, Lodders and Palme, 2009), initial helium abundance (Chiosi and Matteucci, 1982, Casagrande et al., 2007), as well as the different mixing processes like convection, semi–convection, convective overshooting (Monteiro et al., 1996, Christensen-Dalsgaard et al., 2011, Deheuvels and Michel, 2011, Piau et al., 2011, Silva Aguirre et al., 2011a, Trampedach and Stein, 2011), microscopic diffusion, radiative acceleration, and rotational mixing (Thoul et al., 1994, Turcotte et al., 1998, Maeder and Meynet, 2000) have a direct impact on the derived stellar parameters such as mass, radius, and age.

Photometric observations by NASA's *Kepler* space telescope (Borucki et al., 2010) led to the characterization of several hundred solar–type stars using asteroseismology. The recently launched NASA's TESS (Ricker et al., 2015) mission is expected to detect oscillations in up to 10,000 solar–type stars with low temporal resolution, whereas the future ESA's PLATO (Rauer et al., 2014) mission is expected to reach ∼80,000 solar–type stars with detected oscillations based on multi–year observations. With this in mind, efforts are being directed towards increasing the precision of asteroseismic inferences by matching the observed oscillation frequencies (or their combinations) to the corresponding frequencies (or their combinations) obtained from the stellar evolutionary models (Miglio and Montalbán, 2005, Metcalfe et al., 2012, 2014, Silva Aguirre et al., 2013, 2015, Davies et al., 2016). This approach is known to improve the precision of derived stellar parameters over forward modelling methods that only

consider global oscillation parameters, (i.e., the frequency of maximum oscillation power, $\nu_{\rm max}$, and the large frequency separation, $\Delta\nu$; Mathur et al., 2012, Lebreton and Goupil, 2014). It nevertheless yields stellar parameters that are model–dependent and therefore sensitive to the input physics used in the models. For instance, the estimated stellar ages are sensitive to different transport processes such as microscopic diffusion, convection and overshooting, which need to be parameterized. Consequently, the treatment of the input physics becomes a source of uncertainty that cannot be easily accounted for.

Silva Aguirre et al. (2015) compared stellar properties of 33 *Kepler* planet–candidate host stars derived using a variety of stellar evolutionary codes and optimisation/fitting methods, yielding internal systematics of ∼1% in radius and density, ∼2% in mass, and ∼7% in age. In order to avoid internal systematics arising from the adoption of a variety of evolution and optimisation tools, we employ the same tools in all computations performed in this work, — we aim at exploring systematic effects arising from specific choices of the input physics used in models of solar–type stars. In particular, we explore internal systematics[1] arising from the inclusion of diffusion in model grids and changes in element abundances. Inclusion of atomic diffusion in stellar models and its impact on the derived stellar parameters has been the subject of a number of studies over the past decades (Aller and Chapman, 1960, VandenBerg et al., 2002, Dotter et al., 2017). This is mainly because atomic diffusion has been revealed to occur in the Sun and other stars (Guzik and Cox, 1993, Christensen-Dalsgaard et al., 1993b, Korn et al., 2007). We also explore the internal systematics arising from the uncertainty in the solar metallicity mixture. Different solar metallicity mixtures (e.g., Grevesse and Sauval, 1998, Asplund et al., 2009) are being adopted in stellar modelling tools despite differences in the absolute element abundances (Miglio and Montalbán, 2005, Serenelli and Basu, 2010, Silva Aguirre et al., 2015, 2017). This hence becomes a potential source of uncertainty in the derived stellar parameters. Furthermore, we assess the internal systematics arising from commonly used surface correction methods. Ball and Gizon (2017) investigated the performance of different surface correction methods applied to evolved stars (i.e., subgiants and low–luminosity red giants) and established the total additional uncertainties in the derived radii, masses, and ages to be less than 1%, 2%, and 6%, respectively. Here, we assess the performance of different surface correction methods by comparing them with the use of frequency ratios, known to be less prone to near–surface effects (Roxburgh and Vorontsov, 2003).

[1]Hereafter, we describe the internal systematics as the scatter, σ, induced on the derived stellar parameters from differences in the input physics or the surface correction method.

4.3 Target Sample

Our sample consists of 34 solar–type oscillators which have been observed by the *Kepler* satellite. Of these, 32 stars are part of the 'LEGACY' sample (Lund et al., 2017, Silva Aguirre et al., 2017) with the remaining 2 stars being the components of the asteroseismic binary HD 176465 (White et al., 2017, Nsamba et al., 2017). These stars were observed in *Kepler* short–cadence mode ($\Delta t = 58.89\,\mathrm{s}$) for at least 12 months. The sample includes some of the highest signal–to–noise ratio, solar–like oscillators observed by *Kepler*. Details about light curve preparation, power spectrum calculation, the peak–bagging procedure and adopted individual oscillation frequencies are given in Lund et al. (2017).

The target sample is shown in an asteroseismic Hertzsprung–Russell diagram in Fig. 4.1. The adopted $\Delta\nu$ is from Lund et al. (2017), computed following a Gaussian–weighted linear fit to $l = 0$ mode frequencies expressed as a function of the radial order. Most of the stars in the target sample are more evolved than the Sun. Table 4.1 contains the atmospheric properties of the stars in our sample.

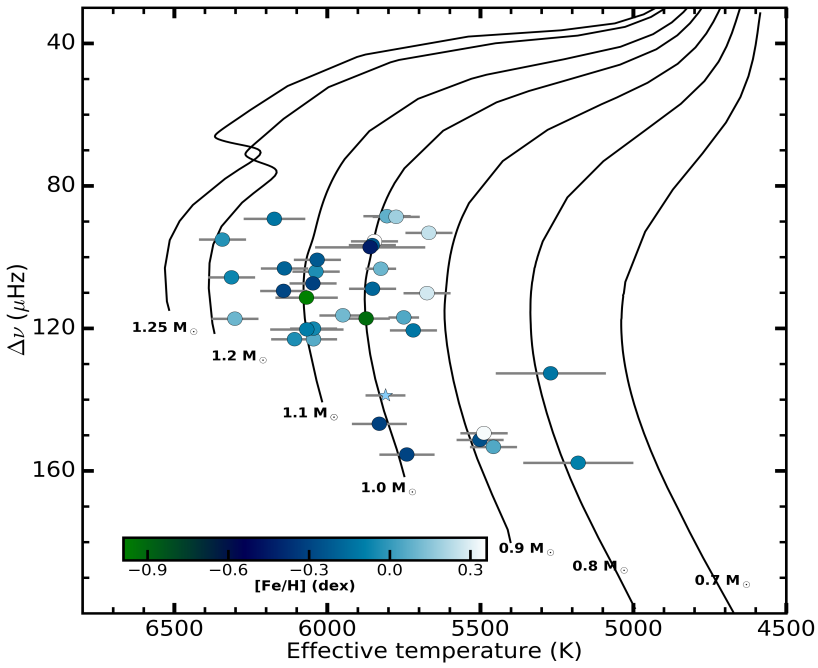

Figure 4.1: Target sample. Stellar evolutionary tracks were constructed at solar metallicity and range in mass from 0.7 to 1.25 $\mathrm{M}_{\odot}$. Stars are colour–coded according to their metallicities. The 'star' symbol corresponds to the position of the Sun.

Most of the spectroscopic parameters were retrieved from Lund et al. (2017). These classical constraints will complement the asteroseismic parameters in the optimisation procedure. The components of the binary HD 176465 (White et al., 2017) have effective temperatures 5830 ± 90 K (HD 176465 A) and 5740 ± 90 K (HD 176465 B), and similar metallicity (-0.30 ± 0.06 dex).

4.4 Grid construction

We used the 1D stellar evolution code MESA (Paxton et al., 2011, 2013, 2015) to generate grids of main sequence and subgiant stellar models. The evolutionary tracks were varied in mass, M, initial metal mass fraction, Z, and mixing length parameter, $\alpha_{\rm mlt}$ (Böhm-Vitense, 1958). The parameter ranges are: $M \in [0.70, 1.25]$ $M_\odot$ in steps of 0.05 $M_\odot$, $Z \in [0.006, 0.031]$ in steps of 0.001, and $\alpha_{\rm mlt} \in [1.3, 2.9]$ in steps of 0.1. In our grids, neither convective overshoot nor semi–convection was included. Stellar models with masses $\gtrapprox 1.1$ $M_\odot$ (at solar metallicity) are expected to have convective cores while on the main sequence and core overshoot may therefore be an important aspect to consider in the construction of a grid. Most of our target stars have masses below this mass limit. The impact of including core overshoot is beyond the scope of this study and it has not been included in our grids. In two of the grids (see Table 4.2), element diffusion was included according to Thoul et al. (1994) to allow for diffusion of hydrogen and gravitational settling of heavy elements (i.e., ^{4}He, ^{16}O, and ^{56}Fe). No radiative acceleration was included in the models.

Specifically, we used MESA version 7624, whose equation of state works with density, ρ, and temperature, T, as independent natural variables in a Helmholtz free energy formulation of thermodynamics. The basic input physics used in all of our grids includes the 2005 updated version of the OPAL equation of state (Rogers and Nayfonov, 2002). The stellar models used opacities from OPAL tables (Iglesias and Rogers, 1996) at high temperatures, whereas at lower temperatures tables from Ferguson et al. (2005) were used instead. Nuclear reaction rates were obtained from tables provided by the NACRE collaboration (Angulo et al., 1999). Specific rates for ^{14}N$(p,\gamma)^{15}$O were from Imbriani et al. (2005) and for ^{12}C$(\alpha,\gamma)^{16}$O from Kunz et al. (2002). The standard Grey–Eddington atmosphere was used to integrate the atmospheric structure from the photosphere to an optical depth of 10^{-4}. The initial helium mass fraction, Y, of our evolution models was determined using the helium–to–heavy metal enrichment law anchored to the big bang nucleosynthesis values of $Z_0 = 0.0$ and $Y_0 = 0.2484$ (Cyburt et al., 2010) . We therefore define the initial helium mass fraction based on

Table 4.1: Spectroscopic parameters of sample stars. The effective temperature ($T_{\rm eff}$) and metallicity ([Fe/H]) are adopted from [a]Casagrande et al. (2014), [b]Pinsonneault et al. (2012),[c]Pinsonneault et al. (2014), and [d]Ramírez et al. (2009) as indicated. The remaining parameters are from Lund et al. (2017).

KIC	$T_{\rm eff}$ (K)	[Fe/H] (dex)
3427720	6045 ± 77	-0.06 ± 0.10
3656476	5668 ± 77	0.25 ± 0.10
3735871	6107 ± 77	-0.04 ± 0.10
4914923	5805 ± 77	0.08 ± 0.10
5184732	5846 ± 77	0.36 ± 0.10
5950854	5853 ± 77	-0.23 ± 0.10
6106415	6037 ± 77	-0.04 ± 0.10
6116048	6033 ± 77	-0.23 ± 0.10
6225718	6313 ± 77	-0.07 ± 0.10
6603624	5674 ± 77	0.28 ± 0.10
7106245	6068 ± 102[a]	-0.99 ± 0.19[a]
7296438	5775 ± 77	0.19 ± 0.10
7871531	5501 ± 77	-0.26 ± 0.10
8006161	5488 ± 77	0.34 ± 0.10
8150065	6173 ± 101[a]	-0.13 ± 0.15[a]
8179536	6343 ± 77	-0.03 ± 0.10
8379927	6067 ± 120[b]	-0.10 ± 0.15[b]
8394589	6143 ± 77	-0.29 ± 0.10
8424992	5719 ± 77	-0.12 ± 0.10
8760414	5873 ± 77	-0.92 ± 0.10
9025370	5270 ± 180[c]	-0.12 ± 0.18[c]
9098294	5852 ± 77	-0.18 ± 0.10
9139151	6302 ± 77	0.10 ± 0.10
9410862	6047 ± 77	-0.31 ± 0.10
9955598	5457 ± 77	0.05 ± 0.10
9965715	5860 ± 180[c]	-0.44 ± 0.18[c]
10079226	5949 ± 77	0.11 ± 0.10
10644253	6045 ± 77	0.06 ± 0.10
10963065	6140 ± 77	-0.19 ± 0.10
11772920	5180 ± 180[c]	-0.09 ± 0.18[c]
12069424	5825 ± 50[d]	0.10 ± 0.03[d]
12069449	5750 ± 50[d]	0.05 ± 0.02[d]

equation 3.5. In order to avoid any systematics that could arise from variations in the treatment of the initial helium mass fraction, we set $\Delta Y/\Delta Z = 2$ (Chiosi and Matteucci, 1982, Casagrande et al., 2007) in all of our grids.

Table 4.2: Summary of adopted grids. No core overshoot was added to any grid.

Name	Mass Range ($M_\odot$)	Solar metallicity mixture	$\frac{\Delta Y}{\Delta Z}$	Diffusion
GS98sta	0.70 – 1.25	Grevesse and Sauval (1998)	2.0	Yes
GS98nod	0.70 – 1.25	Grevesse and Sauval (1998)	2.0	No
AGS09	0.70 – 1.25	Asplund et al. (2009)	2.0	Yes

The grids were evolved starting from the pre–main sequence (PMS) to the zero–age main sequence (ZAMS). We define the ZAMS as the point along the evolutionary track where the nuclear luminosity of the model yields 90% of the total luminosity. All PMS models were discarded since our target stars are more evolved. We then evolved the models from the ZAMS to the point along the evolutionary track where $\log \rho_c = 4.5$ (ρ_c is the central density). This approximately corresponds to the base of the red–giant branch. About 70 models were stored at different ages along each evolutionary track and a total of about 371,280 models for each grid. For each model, we used GYRE (Townsend and Teitler, 2013) in its adiabatic setting to generate theoretical oscillation frequencies. Pressure mode (p–mode) oscillation frequencies were computed for harmonic degrees $l = 0$, 1, 2, and 3 below the acoustic cut–off frequency.

It is worth noting that an offset is always seen between model and observed frequencies (Christensen-Dalsgaard et al., 1988, Dziembowski et al., 1988, Christensen-Dalsgaard and Thompson, 1997). This is due to an improper modelling of the near–surface layers as discussed in Sect. 3.2.3. The surface effect in our model frequencies was corrected using various surface correction methods (see Sect. 4.5.3) and implemented in the optimisation tool (as described in Sect. 3.2.5).

4.5 Results and Discussion

We discuss in detail the different input physics under investigation in Sects. 4.5.1 and 4.5.2. It should be noted that some inputs cannot be examined separately since their modification requires changing other inputs. For instance, modifications in the solar metallicity mixture require setting the corresponding appropriate opacities. Therefore, in such cases, the systematics found are from both sets of inputs. The two–term surface correction method by Ball and Gizon (2014) is used to obtain the results presented in Sects. 4.5.1 and 4.5.2. In Sect. 4.5.3, we used the GS98sta grid in the analysis of the

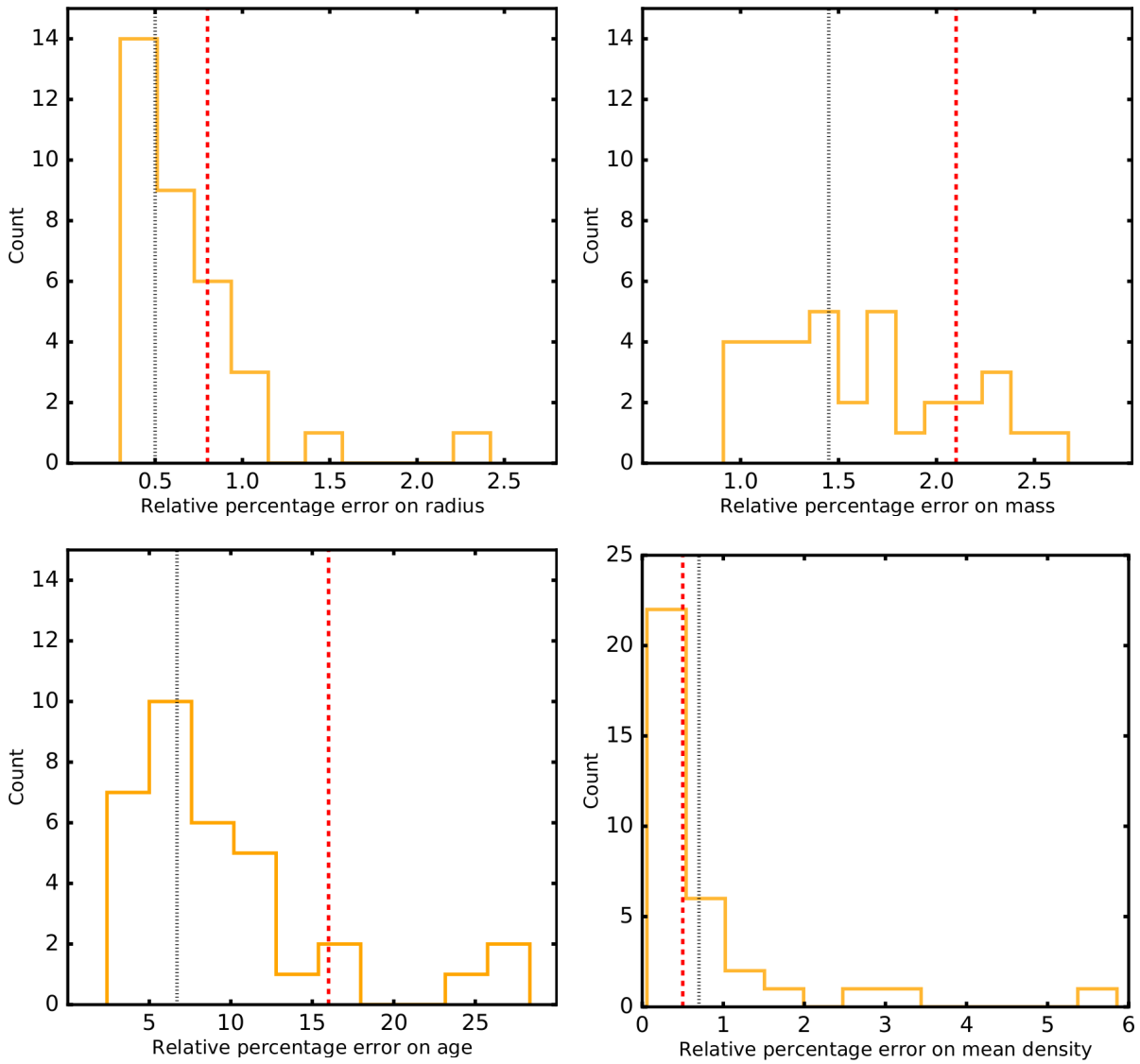

Figure 4.2: Statistical uncertainties and internal systematics. Histograms represent the distributions of statistical uncertainties when adopting the reference grid GS98sta. Black dotted lines represent internal systematic contributions from AGS09 (composition). Red dashed lines represent internal systematic contributions from GS98nod (diffusion).

internal systematics arising from using different frequency correction methods. The percentage median statistical uncertainties obtained when using the reference grid GS98sta are 0.3% in mean density, 0.6% in radius, 1.6% in mass, and 7.4% in age (see Fig. 4.2).

4.5.1 Diffusion

We switch on element diffusion in MESA, which includes chemical diffusion and gravitational settling (Paxton et al., 2011). MESA's diffusion module uses diffusion coefficients from Thoul et al. (1994) in order to solve Burger's equations when calculating particle diffusion and gravitational settling (see Sect. 3.1.1 for details). Figure 4.3 (left panel) shows that stellar ages derived using GS98nod are systematically larger than those derived using GS98sta. In our optimization process, we use the effective

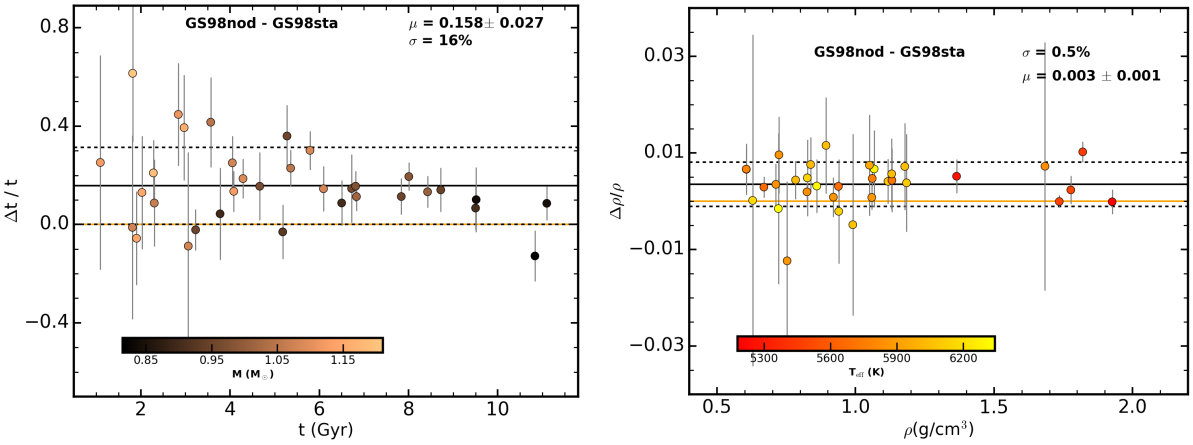

Figure 4.3: Fractional difference in age (left) and mean density (right) as a function of GS98sta stellar parameters. The colour–coding is with respect to stellar mass and effective temperature for the left and right panel, respectively. The solid black line indicates the bias (μ), while the scatter (σ) is represented by the dashed lines. The zero level is represented by the solid orange line.

temperature and metallicity as classical observables. Since element diffusion changes surface element abundances, our GS98sta grid will need to have best–fitting models with higher initial metal mass fractions so that the surface metal mass fractions can be comparable to the observed values at the stars' current ages. This implies the opacity in the cores of these models will be higher throughout their evolution, compared to the case of no diffusion. To avoid the associated decrease in luminosity, which is indirectly constrained by the effective temperature and seismic data, the best–fit models need to have higher mass, justifying their younger age. This is confirmed in Fig. 4.4 (left panel) where we show the fractional differences in the stellar mass. In turn, the strong constraints on the mean density imposed by the seismic data lead to an increase in the radius of the best fit models in our GS98sta grid, as shown in Fig. 4.4 (right panel). In summary, in order to satisfy the observables, models with diffusion need to have higher masses, hence also higher radii and younger ages.

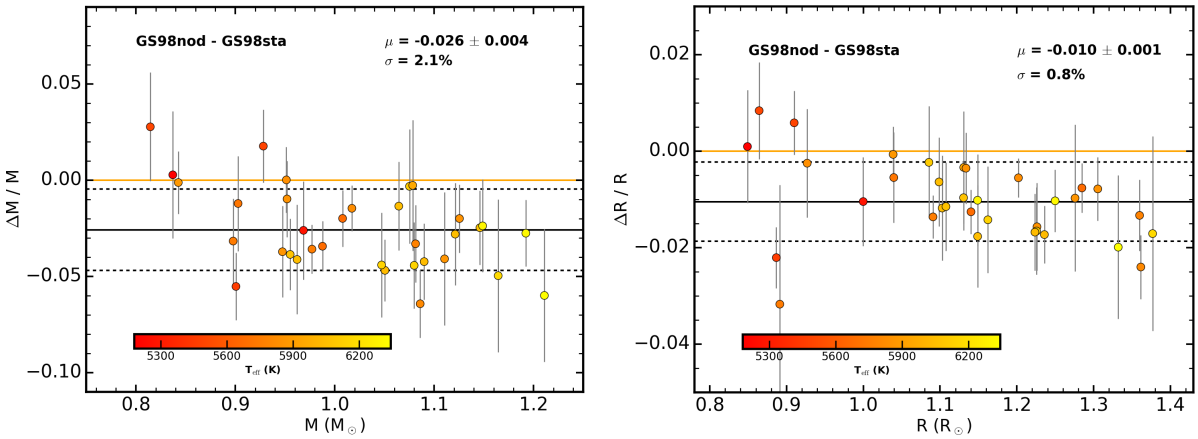

Figure 4.4: Fractional difference in mass (left) and radius (right) as a function of GS98sta stellar parameters. The zero level is represented by the solid orange line. The colour–coding is with respect to effective temperature. The solid black line indicates the bias (μ), while the scatter (σ) is represented by the dashed lines.

We explore internal systematics by comparing models with and without diffusion, resulting in 0.5%, 0.8%, 2.1%, and 16% in mean density, radius, mass, and age, respectively (see Figs. 4.3 and 4.4). The internal systematics in density, mass, and radius are comparable to their statistical uncertainties, while the internal systematics in age are significantly larger than the statistical uncertainties (See Fig. 4.2).

Furthermore, we inspect the data presented in Figs. 4.3 and 4.4 for the presence of linear correlations. We employ a correlation coefficient analysis developed in a Bayesian framework (Figueira et al., 2016). Using it we can estimate the posterior probability distribution of the correlation coefficient. Table 4.3 shows the results from such Bayesian test. At the 95% confidence level, there is a negative linear trend present for the radius and mass, with a hint of a similar trend being present for the age. The difference between the initial and current metal mass fraction, Z, of the

Table 4.3: Statistical summary of the posterior probability distribution of the correlation coefficient. C.I. denotes the confidence interval.

Parameter	Mean	Standard Deviation	95% C.I.
Mass	-0.433	0.135	[-0.69, -0.168]
Radius	-0.342	0.142	[-0.599, -0.049]
Age	-0.247	0.152	[-0.535, 0.047]

best–fitting models of GS98sta increases with increasing stellar mass. This suggests that gravitational settling has a larger impact on higher mass stars, explaining the trend with mass seen in Fig. 4.4.

4.5.2 Composition

Solar metallicity mixtures are one of the most important ingredients in stellar modelling. Here we focus on the most commonly used solar metallicity mixtures in constructing standard solar models, namely, those from Grevesse and Sauval (1998) and Asplund et al. (2009). We define [Fe/H] in all our calculations based on equation 3.4, with solar $Z_{\rm surface}$ values of 0.0134 and 0.0169 based on Asplund et al. and Grevesse and Sauval, respectively. In general, the solar metallicity mixture from AGS09 are lower than those from GS98sta. Basu and Antia (2004) demonstrate that the uncertainty in solar metallicity mixture result in differences in the sound speed in the stellar interiors (see Sect. 3.1.2).

We assess the internal systematics arising from the uncertainty in solar metallicity mixture. We find a good agreement in both the derived ages and densities with

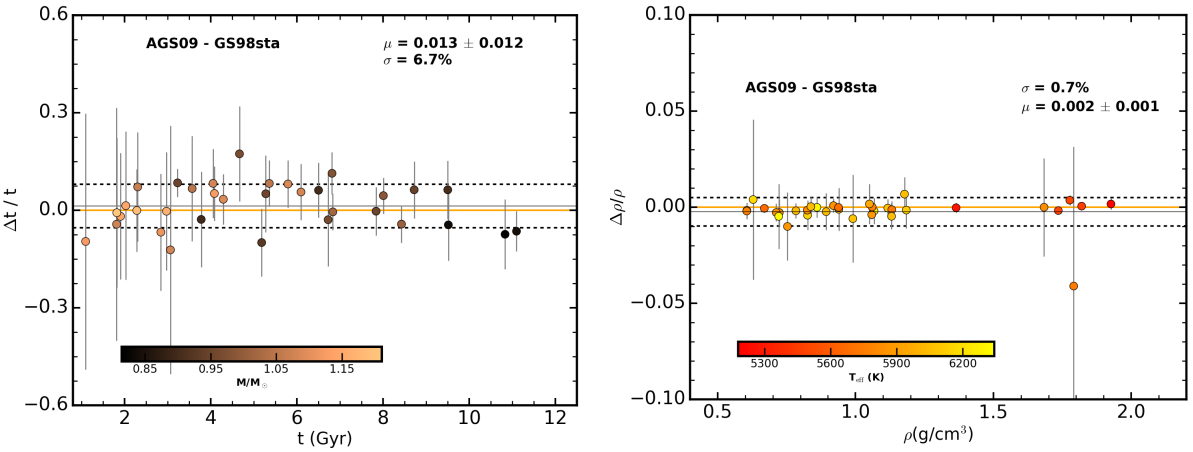

Figure 4.5: Fractional difference in age (left) and mean density (right) as a function of GS98sta stellar parameters. The colour–coding is with respect to stellar mass. The zero level is represented by the solid orange line. The solid black line indicates the bias (μ), while the scatter (σ) is represented by the dashed lines.

internal systematics of 6.7% (with a bias of 0.013 ± 0.012) and 0.7% (with a bias of 0.002 ± 0.001), respectively (see Fig. 4.5). Internal systematics in stellar ages are somewhat smaller than the statistical uncertainties (median of 7.4%) as shown in Fig. 4.2. Furthermore, we find internal systematics of 0.5% in radius and 1.4% in mass (see Fig. 4.6). Silva Aguirre et al. (2015) found systematic contributions arising from the uncertainty in solar metallicity mixture to be 0.3% in mean density and radius, 0.6% in mass and 3.3% in age. The internal systematics found in this work are approximately twice as large as those found by Silva Aguirre et al. (2015). The most probable cause for this discrepancy is in the treatment of the mixing length parameter

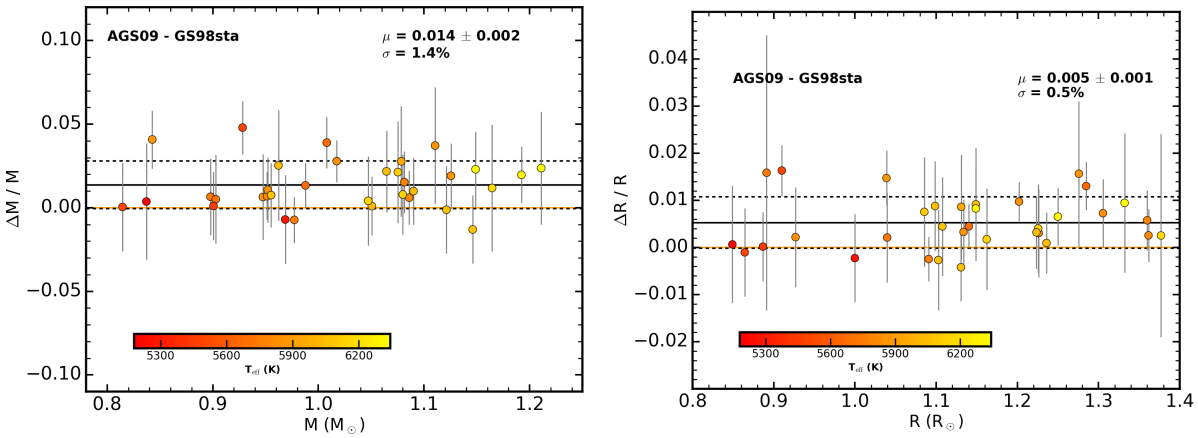

Figure 4.6: Fractional difference in mass (left) and radius (right) as a function of GS98sta stellar parameters. The zero level is represented by the solid orange line. The colour-coding is with respect to effective temperature. The solid black line indicates the bias (μ), while the scatter (σ) is represented by the dashed lines.

($\alpha_{\rm mlt}$). Here, we set $\alpha_{\rm mlt}$ as a free variable in all of our grids (see Sect. 4.4), while Silva Aguirre et al. (2015) used solar calibrated $\alpha_{\rm mlt}$ values. We note that the uncertainty in solar metallicity mixture will cause variations in solar calibrated values of $\alpha_{\rm mlt}$. Systematic uncertainties arising from grids varying in the treatment of $\alpha_{\rm mlt}$ were found to be 0.7%, 0.6%, 2.2%, and 9.0% in mean density, radius, mass, and age, respectively (Silva Aguirre et al., 2015). In addition, based on a grid of 3D convection simulations, $\alpha_{\rm mlt}$ has been shown to span a range of values on the main sequence (Trampedach et al., 2014). It is therefore advisable to use a range of $\alpha_{\rm mlt}$ values when constructing stellar grids for Sun–like stars.

4.5.3 Surface correction

To overcome the well–known systematic differences between model and observed oscillation frequencies (Sect. 3.2.3), several surface correction methods have been put forward (see Table 4.4). The function, f, used in the different surface correction methods is given by

$$f = \frac{\nu}{\nu_0} \quad , \tag{4.1}$$

where ν is the mode oscillation frequency and ν_0 a reference frequency. When using surface correction method proposed by Sonoi et al. (2015), the value of ν_0 is determined in AIMS by means of the scaling relation (Brown et al., 1991, Kjeldsen and Bedding,

1995):

$$\nu_0 = \left(\frac{M}{\mathrm{M}_\odot}\right)\left(\frac{R}{\mathrm{R}_\odot}\right)^{-2}\left(\frac{T_{\mathrm{eff}}}{T_{\mathrm{eff},\odot}}\right)^{-1/2}\nu_{\mathrm{max},\odot} \quad . \tag{4.2}$$

The adopted solar values are $\nu_{\mathrm{max},\odot} = 3104.0\ \mu\mathrm{Hz}$, $\mathrm{R}_\odot = 6.9599 \times 10^{10}\,\mathrm{cm}$, $\mathrm{M}_\odot = 1.98919 \times 10^{33}\,\mathrm{g}$, and $T_{\mathrm{eff},\odot} = 5777.0\,\mathrm{K}$ (Allen, 1976, Mamajek, 2012, Mosser et al., 2013). For other surface corrections, we used

$$\nu_0 = \frac{1}{2\pi}\sqrt{\frac{GM}{R}} \quad , \tag{4.3}$$

where G and R are the gravitational constant and model radius, respectively. This does not make a difference on the correction, but only affects the magnitude of the fitting coefficients (i.e., a and b).

Table 4.4: Summary of the different surface correction methods. a and b are best–fit parameters (see text for details), f is a function that depends on the mode frequency, I is the normalised mode inertia, and $\delta\nu$ is the offset between observed and model frequencies.

Name	Functions	b - value	Reference
KJ	$\delta\nu = af^b$	4.9	Kjeldsen et al. (2008)
BG1	$\delta\nu = af^3/I$	-	Ball and Gizon (2014)
BG2	$\delta\nu = (af^{-1} + bf^3)/I$	-	Ball and Gizon (2014)
Sonoi	$\delta\nu = a\left(1 - \frac{1}{1+f^b}\right)$	4.0	Sonoi et al. (2015)

Kjeldsen et al. (2008) proposed that the offset depends on a power of the mode frequency, whose exponent, b, they determined to be $b = 4.9$ (calibrated with respect to solar data). The same value has subsequently been adopted in the study of other stars (Thompson, 2004, Brandão et al., 2011, Van Eylen et al., 2012, Gruberbauer et al., 2013). Using Canuto–Goldman–Mazzitelli (CGM) modelling of convection, Deheuvels et al. (2014) determined a value of b to be 4.25 and adopted it in generating models using the Cesam2k evolutionary code. We adopted the former value of b in AIMS when using the surface correction of Kjeldsen et al. (2008), as shown in Table 4.4. We note that the scaling factor, r, related to the mean density and proposed by Kjeldsen et al. (2008), is not used in AIMS. The risk with rescaling the model is that one will need to change a number of variables (e.g., how is heat transport affected). It may be possible to rescale the acoustic variables consistently, but other variables may not remain consistent. Hence, for this reason the r–scaling is not implemented in AIMS. If there is a mismatch, then AIMS looks for another model where the mean density

is closer, rather than trying to rescale the model to the right mean density. Ball and Gizon (2014) proposed two functions (BG1 and BG2, see Table 4.4), both taking into account the mode inertia, I, while Sonoi et al. (2015) proposed a Lorentzian function (see Table 4.4 and Sect. 3.2.3) . *We note that we used the same set of observed frequencies for each star when applying the different surface correction methods during the optimisation process. This is because we aimed at carrying out a uniform analysis for all the different surface correction methods.*

We explore the internal systematics from adopting the different surface correction options by comparing the model parameters derived in each case with those obtained when using frequency ratios. Frequency ratios have been shown to be less affected by the poorly modelled surface layers and this permits direct comparison of observed oscillation frequencies with the theoretical oscillations frequencies without applying any surface correction routine (Roxburgh and Vorontsov 2003, Silva Aguirre et al. 2011a, 2015, 2017). Unfortunately, some information about the star is lost when one uses frequency ratios. For instance, since the stellar mean density scales with the frequencies, taking frequency ratios results into factoring out the mean density and thus making frequency ratios less sensitive to the mean density compared to direct comparison with oscillation frequencies (Roxburgh and Vorontsov, 2003). Despite this, frequency ratios have been reported to constrain stellar interiors, resulting in more precise asteroseismic stellar ages compared to the use of individual frequencies. In AIMS, we specified the frequency ratios r_{10} and r_{02}, defined in Sect. 3.2.3.

Hereafter, the surface correction method by Kjeldsen et al. (2008) is denoted by KJ, Sonoi et al. (2015) as Sonoi, Ball and Gizon (2014) one-term correction as BG1, and Ball and Gizon (2014) two–term correction as BG2 (See Table 4.4). Sonoi and BG2 lead to smaller internal systematics in mass: 2.0% and 1.7%, respectively (see Fig. 4.7). We find that the masses are overestimated when employing the corrections by KJ and BG1. KJ also yields internal systematics of 2.0% in mass, albeit affected by a larger bias of 0.029 ± 0.004. All surface correction routines yield similar internal systematics in radius, with BG1 leading to the largest bias (see Fig. 4.8). Both KJ and BG2 produce internal systematics in radius of 0.8%, while Sonoi yields 0.9%. Figure 4.9 shows that Sonoi and BG2 produce smaller internal systematics in age: 8.2% and 7.2%, respectively. KJ results in internal systematics of 10%, while BG1 yields the largest internal systematics (19.4%).

BG2 yields the least median reduced χ^2_ν in the model–to–observed frequency differences of 5.661. Sonoi and KJ yield comparable median reduced χ^2_ν of 15.846 and

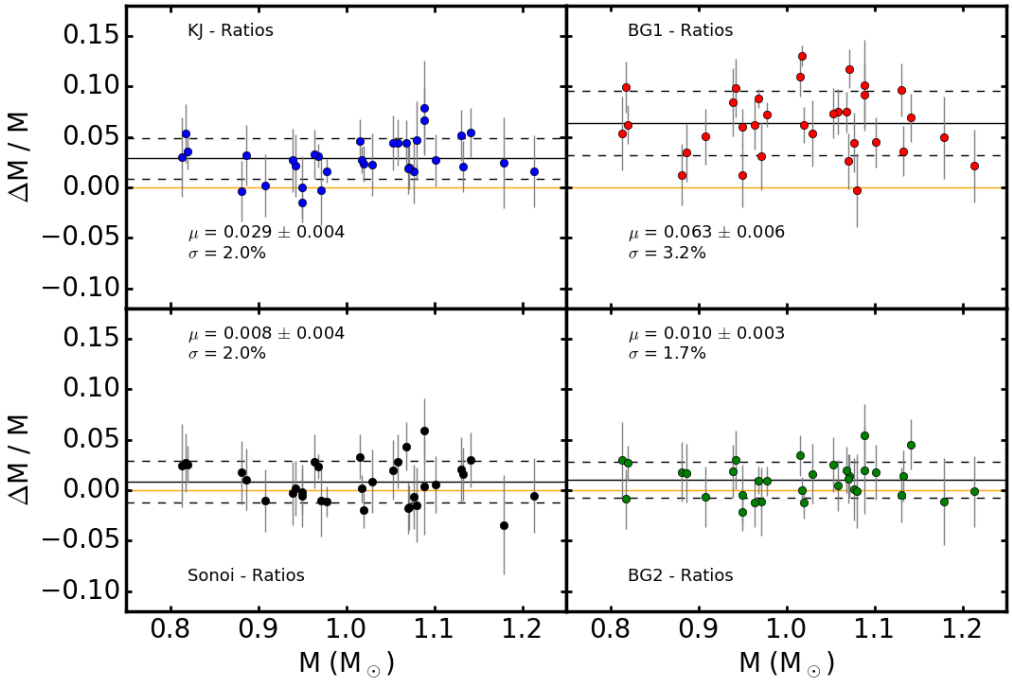

Figure 4.7: Fractional difference in mass as a function of GS98sta stellar masses. The zero level is represented by the solid orange line. The solid black line indicates the bias (μ), while the scatter (σ) is represented by the dashed lines.

15.958, respectively. BG1 gives median reduced χ^2_ν of 27.800. This in turn explains why the BG2 lead to the least internal systematics followed by Sonoi.

In Fig. 4.10, we consider BG2 results as the reference in the comparison with the different surface correction methods. This is because from Figs. 4.7, 4.8, and 4.9, BG2 yields the least internal systematics in mass, radius, and age, respectively. In addition, frequency ratios will provide a poor description of the near–surface layers. It can clearly be seen in Fig. 4.10 that some information about the mean density is lost when one uses frequency ratios. Since we used uncorrected model frequencies to compute the frequency ratios as well as the large frequency separation, the later includes a significant contribution from the surface effect. Assuming that the large frequency separation for the best–fitting model matched reasonably well with the observed separation, the "true" large separation for the model (excluding the surface effect contribution) is significantly underestimated, and hence the corresponding mean density. This is consistent with previous findings by Silva Aguirre et al. (2017). The internal systematics on the mean density arising from varying the surface correction methods are found to be less than 1.5%.

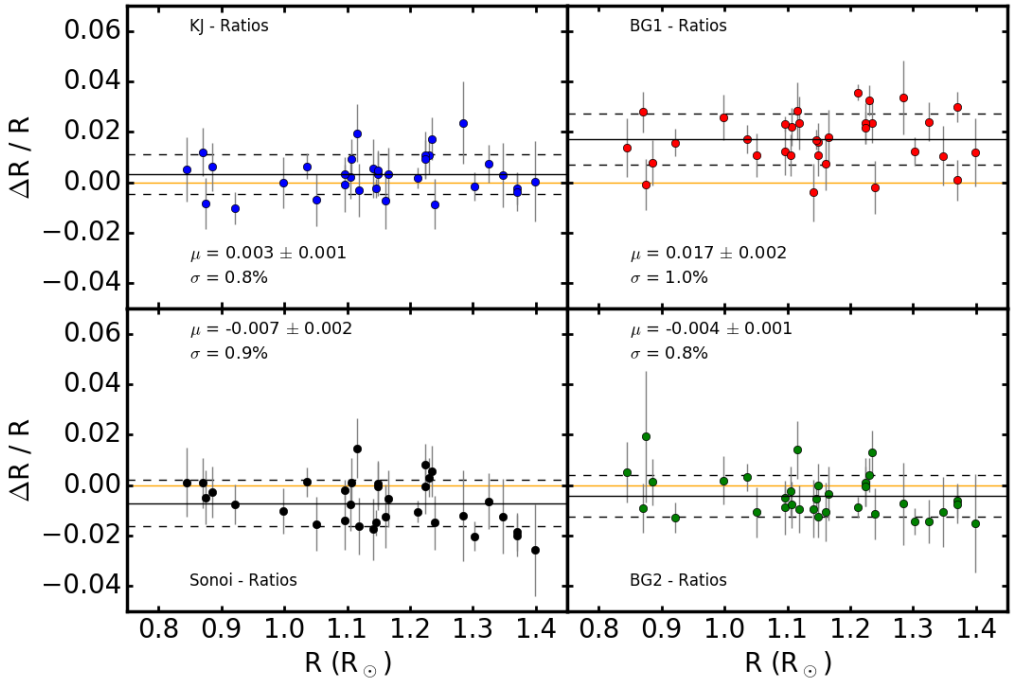

Figure 4.8: Fractional difference in radius as a function of GS98sta stellar radii. The solid black line indicates the bias (μ), while the scatter (σ) is represented by the dashed lines. The zero level is represented by the solid orange line.

We note that when one compares the observed frequencies with the uncorrected theoretical frequencies of the best–fit models obtained using the different surface correction methods, surface corrections should be expected to tend to zero only for low enough frequencies. This is because, assuming the shape of the surface correction does not match with the differences between the observed and "true model" frequencies, then the best–fitting model obtained by minimizing the differences between the observed and surface corrected model frequencies would show differences at the low frequency end. This arises from how the model frequencies evolve as the model itself evolves. It turns out that if the shape of the assumed surface correction is not correct, then one ends up with either under or over evolved model as best–fitting model (depending on whether assumed surface correction over corrects or under corrects). When only frequency ratios are used as seismic constraints, a much larger difference between the observed and uncorrected theoretical frequencies is obtained at the lower frequency end. This is expected since frequency ratios do not carry information about the surface layers. This has a stronger impact on the radius and density. It is for this reason we added the large separation calculated from $l = 0$ mode frequencies.

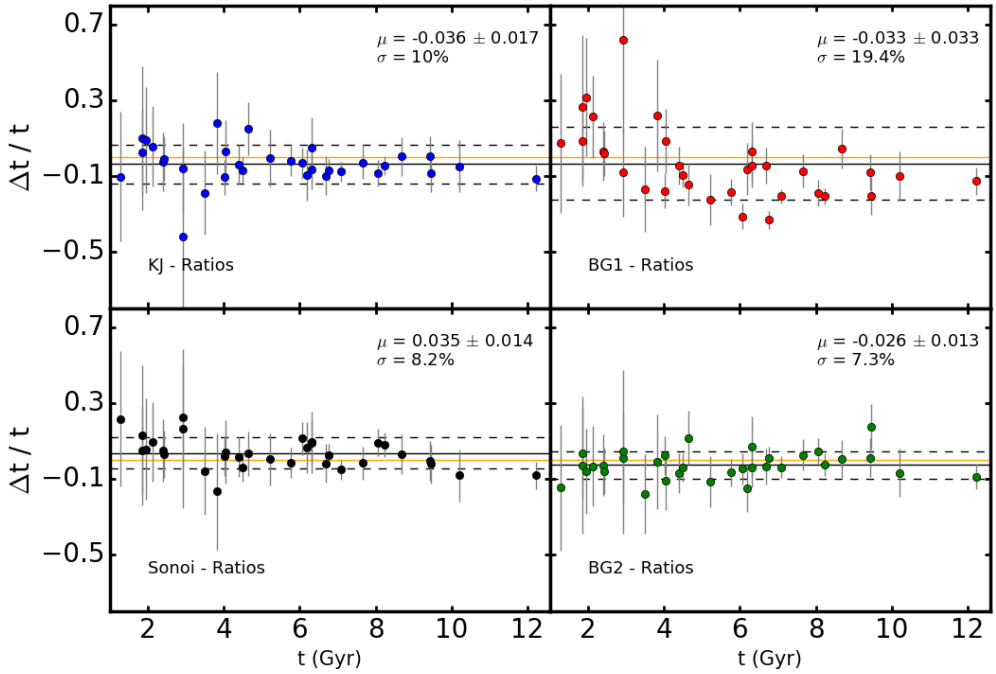

Figure 4.9: Fractional difference in age as a function of GS98sta stellar ages. The zero level is represented by the solid orange line. The solid black line indicates the bias (μ), while the scatter (σ) is represented by the dashed lines.

4.6 Summary

We investigated the internal systematics in mean density, radius, mass, and age arising from changes in particular physical aspects of stellar models. We did so based on the analysis of stellar model grids constructed as uniformly as possible and only varying the input physics being considered. However, internal systematics arising from the uncertainty in solar metallicity mixture will contain contributions from their respective opacities. Moreover, we also assessed the internal systematics arising from the use of different surface correction methods in forward modelling.

We found internal systematics from the uncertainty in solar metallicity mixture to be comparable to the statistical uncertainties. Specifically, we found internal systematics of 0.7%, 0.5%, 1.4%, and 6.7% in mean density, radius, mass, and age, respectively. Relative median statistical uncertainties from using our reference grid (GS98sta) are 0.3% in density, 0.6% in radius, 1.6% in mass, and 7.4% in age. Silva Aguirre et al. (2015) found systematic contributions arising the uncertainty in solar metallicity mixture to be 0.3% in density and radius, 0.6% in mass and 3.3% in age.

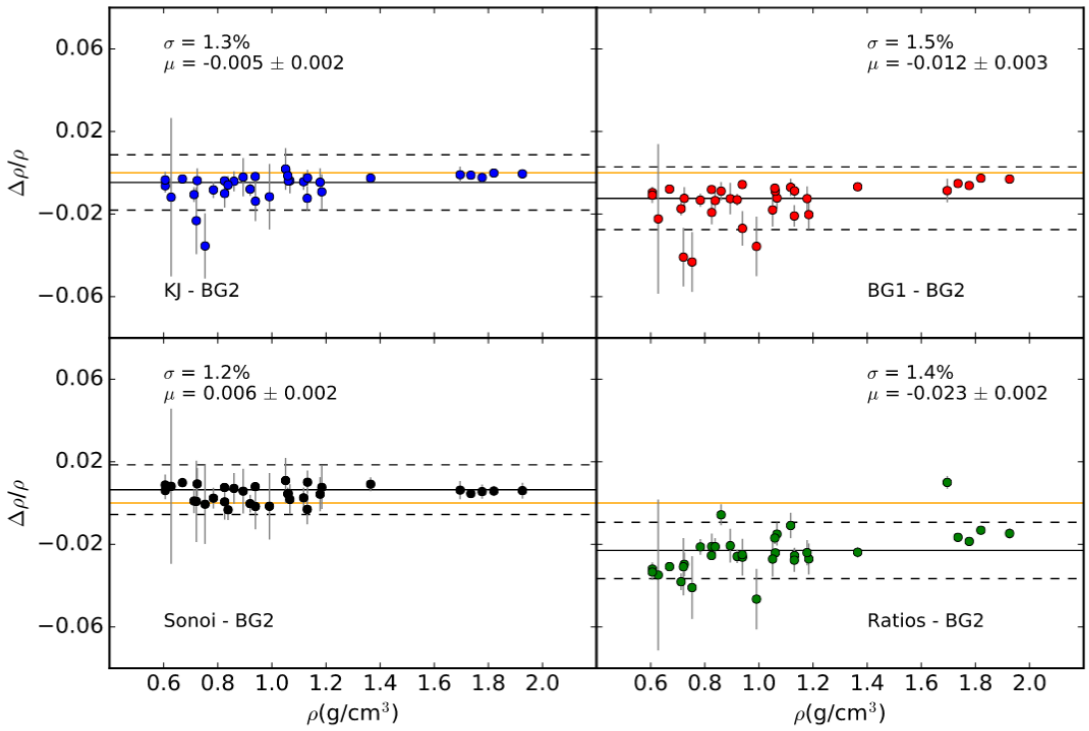

Figure 4.10: Fractional difference in stellar mean density as a function of GS98sta stellar mean density. The zero level is represented by the solid orange line. The solid black line indicates the bias (μ), while the scatter (σ) is represented by the dashed lines.

The internal systematics found in this work are approximately twice as large as those found by Silva Aguirre et al. (2015). The most probable cause for this difference is the fact that we treat the mixing length parameter, $\alpha_{\rm mlt}$ (see Sect. 4.5.2) as a free parameter.

Concerning the impact of diffusion, we have shown that the inclusion of diffusion in stellar grids of solar–type stars leads to models with significantly lower ages. This is consistent with previous findings (Silva Aguirre et al., 2015, Dotter et al., 2017). We found internal systematics of 0.5%, 0.8%, 2.1%, and 16% in mean density, radius, mass, and age, respectively. The internal systematics in age are significantly larger than the corresponding statistical uncertainties.

We assessed the impact of using different surface correction methods on the derived stellar parameters. We found the corrections by Sonoi and BG2 to yield the least internal systematics, namely, 0.9% and 0.8% in radius, 2.0% and 1.7% in mass, and 8.2% and 7.3% in age, respectively. These internal systematics are comparable to the statistical uncertainties. KJ performs satisfactorily for our sample (see discussion in

Sect. 4.5.3), while BG1 yields the largest internal systematics as well as the largest biases for stellar radius and mass. We found stellar masses to be overestimated when using the KJ and BG1 corrections.

Asteroseismology is proving to be particularly significant for the study of solar–type stars, in great part due to the exquisite data that have been made available by NASA's *Kepler* space telescope. The information contained in stellar oscillations allows the internal stellar structure to be constrained to unprecedented levels, while also allowing fundamental stellar properties (e.g., mass, radius, and age) to be precisely determined. Particular attention is being placed on calibrating the determination of age, due to the strong dependence this quantity has on stellar physics. This work therefore provides a valuable contribution to this communal effort by assessing the systematics on the derived stellar properties that arise from specific changes in the model input physics.

Chapter 5

α Centauri A as a potential stellar model calibrator: establishing the nature of its core

The content presented in this chapter was published in May of 2018 in *Monthly Notices of the Royal Astronomical Society*, volume 479, pages L55–L59. This was authored by B. Nsamba, M. J. P. F. G. Monteiro, T. L. Campante, M. S. Cunha, and S.G. Sousa. The research work was carried out by me and was based on the objectives of this thesis. I note that the spectroscopic analysis component was carried out by S. G. Sousa. The text was written by myself with a substantial contribution from my fellow coauthors.

5.1 Chapter synopsis

Understanding the physical process responsible for the transport of energy in the core of α Centauri A is of the utmost importance if this star is to be used in the calibration of stellar model physics. Adoption of different parallax measurements available in the literature results in differences in the interferometric radius constraints used in stellar modelling. Further, this is at the origin of the different dynamical mass measurements reported for this star. With the goal of reproducing the revised dynamical mass derived by Pourbaix and Boffin, we modelled the star using two stellar grids varying in the adopted nuclear reaction rates. Asteroseismic and spectroscopic observables were complemented with different interferometric radius constraints during the optimisation procedure. Our findings show that best–fit models reproducing the revised dynamical mass favour the existence of a convective core ($\gtrsim$ 70% of best–fit models), a result

that is robust against changes to the model physics. If this mass is accurate, then α Centauri A may be used to calibrate stellar model parameters in the presence of a convective core.

5.2 Introduction

Stellar physicists have for decades yearned for a star more massive than the Sun with a range of precisely measured observables, namely, spectroscopic parameters, an interferometric radius, asteroseismic properties, and a dynamical mass measurement. This stems from the fact that stellar model physics (e.g., mixing length parameter, treatment of the initial helium mass fraction, surface element abundances, etc.) is often calibrated based on the Sun and used in the modelling of other stars (e.g., Christensen-Dalsgaard 2009, Asplund et al. 2009, Bonaca et al. 2012, Vorontsov et al. 2013, Silva Aguirre et al. 2015, 2017). This is a reasonable approach for stars within the same mass range and with a similar metal content as the Sun. For more massive stars, however, this may not hold, since their internal structure significantly differs from that of the Sun.

α Centauri A presents a unique opportunity to improve our understanding of the underlying physical processes taking place in stars slightly more massive than the Sun. This is due to a number of reasons: (i) α Centauri A is one of the components of the closest binary system to the Sun, having well determined orbital parameters (Pourbaix and Boffin, 2016, Kervella et al., 2017)[1]. A dynamical mass measurement is available for both components of the binary (P02; P16; K16). (ii) Precise parallax measurements are available and have been used to yield a distance to the star (S99; K16). This distance has been combined with an interferometric measurement of the star's angular diameter to obtain its radius (K03; P16; K17). (iii) Spectroscopic parameters (e.g., effective temperature, metallicity etc.) are readily available. (iv) Several ground–based campaigns have been conducted in order to obtain asteroseismic data for this star (Bouchy and Carrier, 2002, Bedding et al., 2005, Bazot et al., 2007, de Meulenaer et al., 2010). The combination of the above set of observables has thus the potential to place tight constraints on the stellar modelling process and help generating best–fit

[1]Hereafter, we note Pourbaix et al. (2002) as P02, Kervella et al. (2003) as K03, Kervella et al. (2016) as K16, Pourbaix and Boffin (2016) as P16, Kervella et al. (2017) as K17, and Söderhjelm (1999) as S99.

models[2] that can be used in understanding the internal structure of α Centauri A with unprecedented precision.

The dynamical mass of α Centauri A is estimated to span the range [1.10, 1.13] $M_{\odot}$. Stellar models constructed at solar metallicity within this mass range may display a convective core while on the main sequence, making core overshoot a crucial process to be included in stellar model grids. For this reason, efforts have been made throughout the years to unveil the nature and core properties of α Centauri A using the above set of observables (Miglio and Montalbán, 2005, Bazot et al., 2016).

A radius measurement (with a precision of about 1%), when combined with spectroscopic and seismic constraints, has been shown to yield stellar masses with a precision of about 1% (Creevey et al., 2007). α Centauri A has been modelled by several teams, who adopted the interferometric radius of K03 (i.e., 1.224 $\pm$ 0.003 $R_{\odot}$) as well as complementary spectroscopic and seismic data (Thoul et al., 2003, Miglio and Montalbán, 2005, Bazot et al., 2016). They were able to reproduce the dynamical mass derived by P02. However, differences in the parallax measurements available in the literature inevitably lead to differences in the interferometric radius measurements. This also yields different dynamical mass measurements for the star (see Table 5.1).

P16 combined radial velocity data from HARPS (High Accuracy Radial velocity Planet Searcher) spanning a period of ten years with data obtained with the Coudé Echelle Spectrograph (CES), further complemented by visual observations (Pourbaix et al., 1999), to generate a revised parallax measurement. This revised parallax places the star at a slightly different distance compared to that measured by S99. This led to the revision of the dynamical mass of α Centauri A by P16. The interferometric radius was also revised by combining the new parallax with the angular diameter measurement from K03 (see Table 5.1). K16 also computed orbital parameters for α Centauri A by combining the same high precision radial velocity data set as P16 with their latest astrometric measurements. They found most of the orbital elements to be commensurate with those found by P16. However, they found a smaller semi–major axis, a, emerging from the new astrometry (see table 1 in K16). When a was combined with the high precision radial velocities, they obtained a parallax measurement similar to the one found by S99 but larger than that of P16 (see Table 5.1). Differences are also evident in the derived dynamical masses and interferometric radius measurements of P16 and K16.

[2]In this work, we refer to a set of models that reproduce a specific set of spectroscopic, seismic, and interferometric constraints as best–fit models.

Table 5.1: Stellar parameters from different literature sources. $\theta_{\rm LD}$ is the angular diameter. The sources for the parallax and angular diameter measurements used in deriving the dynamical mass and interferometric radius are indicated as superscripts. ^{a} denotes S99, ^{b} S99 and K03, ^{c} K03 and K16, ^{d} K16, ^{e} K03 and P16, ^{f} P16, and ^{g} K16 and K17.

Parameter	S99	P02	K03	P16	K16	K17
$\theta_{\rm LD}$ (mas)	–	–	8.511 ± 0.020	–	–	8.502 ± 0.038
Parallax (mas)	747.1 ± 1.2	–	–	743 ± 1.3	747.17 ± 0.61	–
Radius ($R_\odot$)	–	–	1.224 ± 0.003^b	1.231 ± 0.0036^e	1.2234 ± 0.0053^c	1.2234 ± 0.0053^g
Mass ($M_\odot$)	–	1.105 ± 0.0070^a	–	1.133 ± 0.0050^f	1.1055 ± 0.0039^d	–

With regard to the nature of the core of α Centauri A, no definitive answer has been reached yet. Miglio and Montalbán (2005) attribute this to the quality of the seismic data available by then (see Kjeldsen et al. 2004). Bazot et al. (2007) obtained a new set of seismic data using the HARPS spectrograph, having investigated the nature of the core of α Centauri A in Bazot et al. (2016). They found that approximately 40% of their best–fit models, which reproduce the dynamical mass derived by P02, possess convective cores. However, the authors point out that this number depends sensitively on the nuclear reaction rates adopted in their models. We note that they used the interferometric radius derived by K03 in their optimisation procedure.

de Meulenaer et al. (2010) have generated the state–of–the–art seismic data set for α Centauri A by combining the radial velocity time series obtained with three spectrographs in Chile and Australia (namely, CORALIE, UVES, and UCLES). Here, we adopt this data set and assess the occurrence of best–fit models with convective cores when trying to reproduce the dynamical masses derived by both P16 and K16.

5.3 Stellar Model Grids

We constructed two grids (A and B) of stellar models using MESA version 9793 (Paxton et al., 2015). These grids differ only in the adopted nuclear reaction rates (see Table 5.2 for details). Bazot et al. (2016) found the occurrence of models of α Centauri A with convective cores to vary mainly due to the choice of nuclear reaction rates, in particular that of the $^{14}\mathrm{N}(p,\gamma)^{15}\mathrm{O}$ reaction. This reaction rate is crucial for the CNO (carbon–nitrogen–oxygen) cycle and its variation is expected to significantly affect the chances of a model developing a convective core. We therefore varied the nuclear reaction rates in order to test the robustness of the occurrence of best–fit models with convective cores when using different observational constraints (see Sect. 5.4).

Table 5.2: Main features of the stellar model grids adopted in this work.

Grid	Reaction Rates	Core Overshoot	Diffusion
A	JINA REACLIB	Yes	Yes
B	NACRE	Yes	Yes

Grid A employs nuclear reaction rates from JINA REACLIB (Joint Institute for Nuclear Astrophysics Reaction Library) version 2.2 (Cyburt et al., 2010). It should be noted that grid A uses specific rates for $^{14}\mathrm{N}(p,\gamma)^{15}\mathrm{O}$ and $^{12}\mathrm{C}(\alpha,\gamma)^{16}\mathrm{O}$ described by Imbriani et al. (2005) and Kunz et al. (2002), respectively. Grid B employs nuclear reaction rates as obtained from tables provided by the NACRE (Nuclear Astrophysics

Compilation of Reaction Rates) collaboration (Angulo et al., 1999). Furthermore, element diffusion is a relevant transport process in low mass stars, i.e., below ∼1.2 $M_\odot$ (e.g., Nsamba et al. 2018b), and was therefore included in our model grids. Core overshoot becomes a vital process once a stellar model develops a convective core and was included in such models.

The version of MESA used in this work adopts the 2005 update of the OPAL equation of state (Rogers and Nayfonov, 2002). Opacities from OPAL tables (Iglesias and Rogers, 1996) were used at high temperatures while tables from Ferguson et al. (2005) were adopted at lower temperatures. We used the surface chemical abundances of Grevesse and Sauval (1998) with a solar metal mass fraction value of 0.0169. The standard Grey–Eddington atmosphere was used to describe the surface boundary (it integrates the atmosphere structure from the photosphere down to an optical depth of 10^{-4}). Convection was described using the mixing length theory (MLT; Böhm-Vitense, 1958) while element diffusion was implemented according to Thoul et al. (1994). Element diffusion includes gravitational settling and chemical diffusion. The helium–to–heavy metal enrichment relation was used to determine the helium mass fraction (Y). The ratio $\Delta Y/\Delta Z = 2$ (Chiosi and Matteucci, 1982) was used, while $Z_0 = 0.0$ and $Y_0 = 0.2484$ were set based on the big bang nucleosynthesis (Cyburt et al., 2003).

Evolutionary tracks are varied in mass, M, metal mass fraction, Z, mixing length parameter, $\alpha_{\rm mlt}$, and core overshoot parameter, f. We used the exponential diffusive overshoot recipe in MESA when describing core overshoot mixing (Herwig, 2000). Grid parameter ranges are: M ∈ [1.0, 1.2] $M_\odot$ in steps of 0.01 $M_\odot$, Z ∈ [0.023, 0.039] in steps of 0.001, $\alpha_{\rm mlt}$ ∈ [1.3, 2.5] in steps of 0.1, and f ∈ [0, 0.03] in steps of 0.005. We kept models starting from the ZAMS (zero–age main sequence to the end of the sub giant evolution stage. Using GYRE (Townsend and Teitler, 2013), we generated adiabatic oscillation frequencies for spherical degrees $l = 0$, 1, 2, and 3 for each model.

5.4 Observational Constraints and Optimisation Procedure

We downloaded a few high S/N, individually reduced HARPS observations of α Centauri A, which were combined to generate a final spectrum for subsequent analysis. Spectroscopic parameters (i.e., effective temperature, $T_{\rm eff}$, and metallicity, [Fe/H]) were derived based on the analysis of the equivalent widths of Fe I and Fe II lines measured with ARES (Sousa et al., 2007, 2015) and assuming LTE (Local Thermodynamical

Equilibrium). We used the MOOG code (Sneden, 1973) and a set of plane–parallel ATLAS9 model atmospheres (Kurucz, 1993) in our analysis, as described in Sousa et al. (2011). For more details on the combined ARES+MOOG method, we refer the reader to Sousa (2014). We obtained $T_{\rm eff} = 5832 \pm 62$ K and $[{\rm Fe/H}] = 0.23 \pm 0.05$ dex.

Using the angular diameter measurement of K17 together with the parallax measurement of P16, we revised the interferometric radius of α Centauri A by means of the expression (Ligi et al., 2016):

$$R(R_{\odot}) = \frac{\theta_{\rm LD} \times {\rm d[pc]}}{9.305} \quad , \tag{5.1}$$

where d[pc] is the distance to the star expressed in parsec. We find the revised interferometric radius to be 1.230 ± 0.0056 $R_{\odot}$. This is in agreement with the value obtained by P16 within 1σ.

Table 5.3: Spectroscopic and interferometric constraints adopted during the optimisation procedure.

Run	$T_{\rm eff}$ (K)	[Fe/H] (dex)	Radius
1	5832 ± 62	0.23 ± 0.05	1.231 ± 0.0036
2	5795 ± 19	0.23 ± 0.05	1.2234 ± 0.0053

We will be considering two optimisation runs in this work (Run 1 and Run 2) depending on the set of observables adopted (see Table 5.3). The value of $T_{\rm eff}$ used in Run 1 was derived in this work while the interferometric radius is from P16. For self–consistency, Run 2 uses the interferometric radius and $T_{\rm eff}$ from K16. The value of [Fe/H] used in both runs is the one derived here.

The set of observables in Table 5.3 was complemented with seismic data (i.e., individual oscillation frequencies) from de Meulenaer et al. (2010). We treated modes exhibiting rotational splittings in the same way as de Meulenaer et al. (2010), i.e., by taking their average and summing the associated uncertainties in quadrature. This is based on the assumption that such splittings are symmetric. The combined–term, surface frequency correction method of Ball and Gizon (2014) was used to handle the offset between observed and model frequencies (Dziembowski et al., 1988). This method has been shown to yield the least internal systematics in stellar mass, radius, and age when compared to other methods (for details, see Nsamba et al. 2018b).

Finally, we used AIM to generate a representative set of models reproducing the set of asteroseismic, spectroscopic, and interferometric constraints (as per above). The mean and standard deviation of the posterior probability distribution functions (PDFs)

are taken as estimates of the modelled stellar parameters and their uncertainties, respectively.

5.5 Results

Results obtained by combining both grids (A and B) and sets of observables (Run 1 and Run 2) are shown in Table 5.4 and Fig. 5.1. Only posterior PDFs showing significant differences are shown in Fig. 5.1.

Results based on the set of observables in Run 2 are consistent within 1σ. The derived stellar mass is in agreement with the dynamical mass obtained by P02 and K16 (even if at the 2σ level when considering grid A). These results are also consistent with those obtained by other modelling teams (Miglio and Montalbán, 2005, Bazot et al., 2012, 2016). This is because these teams complemented seismic and spectroscopic constraints with the interferometric radius of K03, whose value is in close agreement (within 1σ) with that used in Run 2.

Results based on the set of observables in Run 1 are also consistent within 1σ. The derived stellar mass is now in agreement with the revised dynamical mass of P16. We found similar results when replacing the interferometric radius of P16 with that derived in this work (cf. Sect. 5.4). This was expected as both values agree within 1σ.

When adopting the set of observables in Run 1, grids A and B return similar yields of 70% and 77% of best–fit models with convective cores, respectively. A contrasting picture emerges when considering the set of observables in Run 2: 46% (grid A) versus 77% (grid B). This is mainly due to the different nuclear reaction rates used in both grids. The reaction rate for $^{14}\mathrm{N}(p,\gamma)^{15}\mathrm{O}$ from Imbriani et al. (2005) used in grid A is lower compared to that from NACRE (Angulo et al., 1999) in grid B. This reduces the chances of having convection as a means of energy transport in the core of stellar models in grid A. In addition, Run 1 yields more models in the high mass regime (see Fig. 5.1), which increases the chances of the CNO cycle being the main energy production chain, resulting in more models with convective cores. We also find models with convective cores to have on average a higher metallicity compared to those with radiative cores. This is consistent with the findings of Bazot et al. (2016).

In the leftmost panel of Fig. 5.1, a shift (although still retaining a 1σ agreement) in the posterior PDFs for the stellar mass can be seen (dashed lines or Run 2). This is again due to the change in the nuclear reaction rates. Results based on grid B yield a large fraction of models with convective cores and therefore higher masses compared to results based on grid A, for which a relatively large fraction of models

Table 5.4: Stellar parameters obtained by combining both grids (A and B) and sets of observables (Run 1 and Run 2).

Grid	Run	M ($M_\odot$)	t (Gyr)	Z_0	X_0	$\alpha_{\rm mlt}$	$Y_{\rm surf}$	Convective Core (%)
A	1	1.12 ± 0.01	4.30 ± 0.35	0.034 ± 0.002	0.649 ± 0.006	1.97 ± 0.10	0.282 ± 0.004	70
	2	1.09 ± 0.01	4.74 ± 0.40	0.035 ± 0.002	0.648 ± 0.006	1.76 ± 0.07	0.280 ± 0.004	46
B	1	1.12 ± 0.01	4.32 ± 0.33	0.034 ± 0.002	0.650 ± 0.007	1.97 ± 0.10	0.282 ± 0.005	77
	2	1.10 ± 0.01	4.39 ± 0.38	0.034 ± 0.002	0.650 ± 0.006	1.76 ± 0.07	0.281 ± 0.003	77

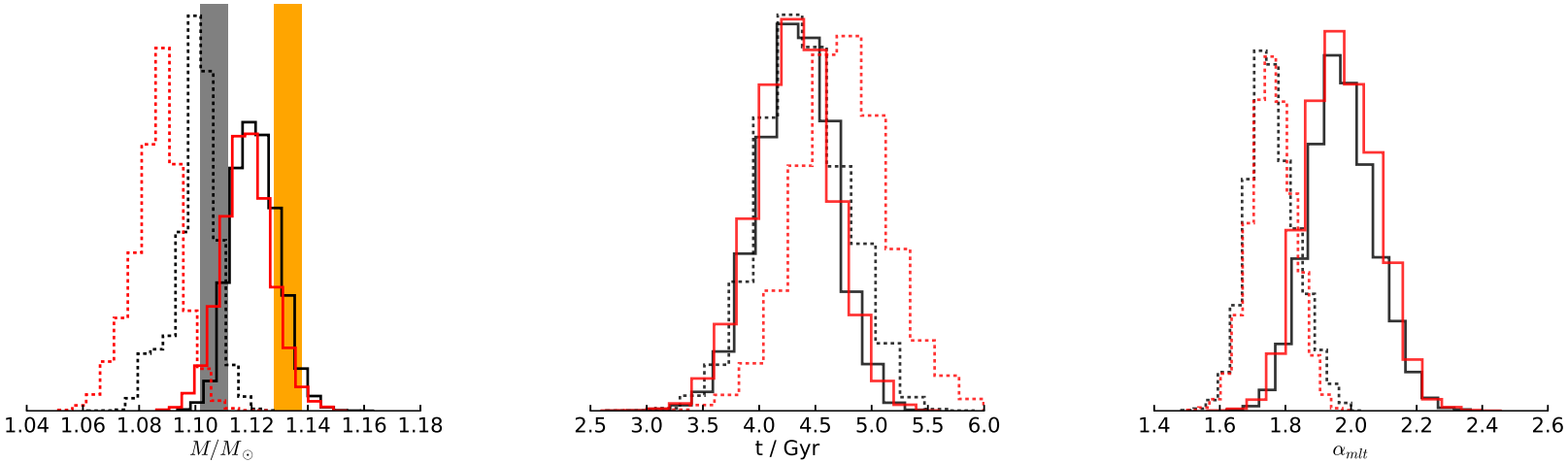

Figure 5.1: Posterior PDFs of stellar parameters obtained using grid A (red) and grid B (black). Solid lines show results from Run 1 while dashed lines are for Run 2. Grey and orange bars correspond to the dynamical mass measurements (and associated uncertainties) of K16 and P16, respectively.

with radiative cores are obtained, thus resulting in lower masses on average. The lower masses obtained in the latter case lead to a slightly higher age (middle panel of Fig. 5.1). The mass range of best–fit models obtained in Run 1 is shifted toward higher masses than that of Run 2. Also, the effect of changing the nuclear reaction rates turns out to be less effective in this higher–mass range since most models have developed convective cores. This explains the consistency in the results obtained with both grids when using Run 1.

A noticeable difference in the mixing length parameter, $\alpha_{\rm mlt}$, can be seen between the results based on Run 1 and Run 2 (rightmost panel of Fig. 5.1). The most probable cause for this, is the different interferometric radius constraint used.

The percentage of best–fit models with convective cores that reproduce the revised dynamical mass derived by P16 (Run 1) is similar for both grids. However, when reproducing the dynamical mass derived by P02 and K16 (Run 2), the percentage of best–fit models with convective cores varies depending on which grid is used, indicating a strong sensitivity to the nuclear reaction rates adopted (cf. Bazot et al., 2016).

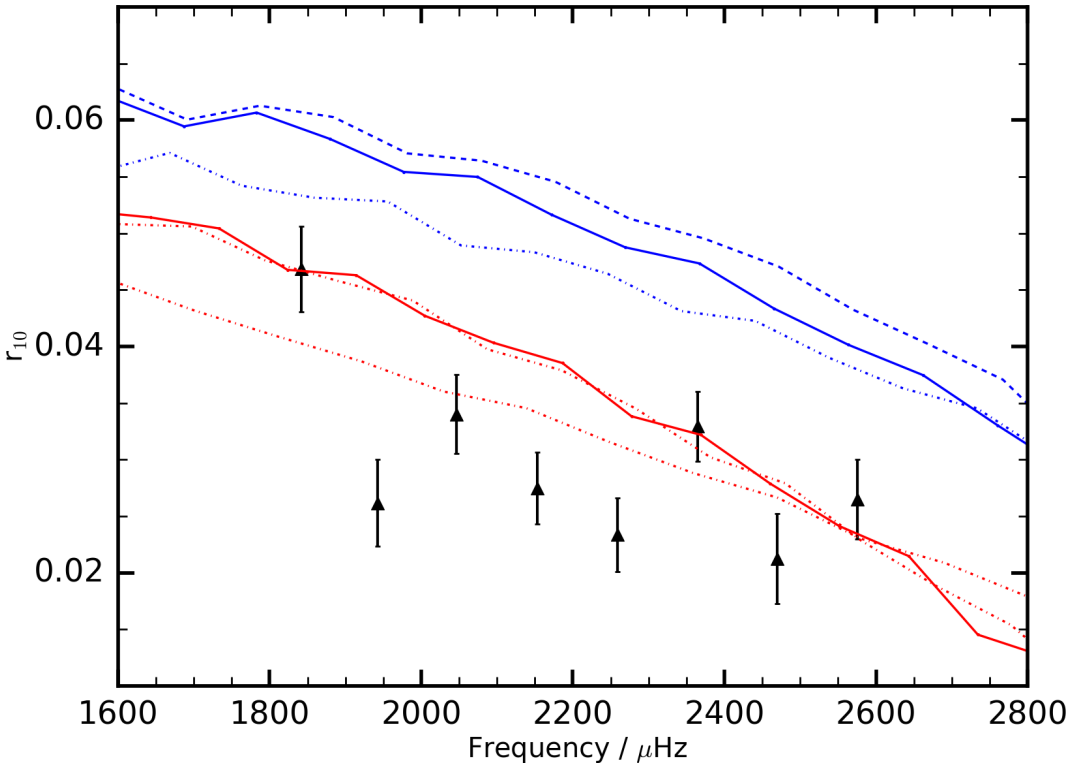

Figure 5.2: Comparison of observed frequency ratios r_{10} (black triangles) with those from models with radiative (blue lines) and convective cores (red lines).

We further compared the observed frequency ratios, r_{10} (see Roxburgh and Vorontsov 2003), to those computed for a handful of representative best–fit models (for Run 1, grid A) having either convective or radiative cores (see Fig. 5.2). Frequency ratios are less prone to the outer layers of the star and are therefore reliable indicators of the deep stellar interior conditions. Our findings seem to indicate that models having a convective core lead to a better agreement with the observed r_{10}, contrary to what was found by de Meulenaer et al. (2010). This is not surprising, as we complemented our seismic data with the interferometric radius of P16, which yields models that reproduce well the revised dynamical mass of P16. de Meulenaer et al. (2010), on the other hand, used models from Miglio and Montalbán (2005), which reproduce the dynamical mass of P02.

5.6 Conclusions

In this study, we have successfully reproduced the revised dynamical mass of α Centauri A derived by P16 using a forward stellar modelling approach. Our findings show that best–fit models favour the presence of a convective core in α Centauri A, regardless of the nuclear reaction rates adopted in the modelling. We therefore conclude that, if the revised dynamical mass of P16 is accurate, then α Centauri A may be used to calibrate stellar model parameters in the presence of a convective core. Furthermore, the percentage of best–fit models having convective cores that reproduce the smaller dynamical mass published by P02 and K16 varies depending on the choice of nuclear reaction rates.

Our findings further stress the importance of a precise interferometric radius (with a precision better than 1%) in complementing seismic data with the aim of tightly constraining stellar models when adopting a forward modelling approach (cf. Miglio and Montalbán, 2005, Creevey et al., 2007).

Seismic diagnostics of the nature of stellar cores based on frequency combinations demand a relative uncertainty on the observed individual frequencies of about 10^{-4} (e.g., Cunha and Metcalfe, 2007, Brandão et al., 2014), commensurate with that obtained from multi–year, space-based photometry (Silva Aguirre et al., 2013, Lund et al., 2017). Our results reveal that, for α Centauri A, a median relative uncertainty on the observed individual frequencies of 2.5×10^{-4} is sufficient to allow the use of frequency ratios in drawing a distinction — even if merely qualitative – between best–fit models with different core properties.

Chapter 6

On the nature of the core of α Centauri A: the impact of the metallicity mixture

The content presented in this chapter was published in April of 2019 in *Frontiers in Astronomy and Space Sciences*, volume 6, page 25. This was authored by B. Nsamba, M. J. P. F. G. Monteiro, T. L. Campante, M. S. Cunha, and S.G. Sousa. The spectroscopic analysis component of this project was carried out by S.G. Sousa. The research work was carried out by me and was based on the objectives of this thesis. The text was written by myself with a substantial contribution from my fellow coauthors.

6.1 Chapter synopsis

Forward asteroseismic modelling plays an important role towards a complete understanding of the physics taking place in deep stellar interiors. With a dynamical mass in the range over which models develop convective cores while in the main sequence, the solar–like oscillator α Centauri A presents itself as an interesting case study. We address the impact of varying the metallicity mixture on the determination of the energy transport process at work in the core of α Centauri A. We find that $\gtrsim 70\%$ of models reproducing the revised dynamical mass of α Centauri A have convective cores, regardless of the metallicity mixture adopted. This is consistent with the findings in Chapter 5, where nuclear reaction rates were varied instead. Given these results, we propose that α Centauri A be adopted in the calibration of stellar model parameters when modelling solar–like stars with convective cores.

6.2 Introduction

Most parameters used in stellar modelling are calibrated based on the Sun, e.g., the mixing length parameter, the helium–to–heavy–element ratio, chemical abundances etc. This approach is well–suited to the modelling of stars with similar properties to the Sun, i.e., for solar–type stars with a mass below 1.1 $M_{\odot}$. The quest for a more massive star with well–known properties and interior structure is of the utmost importance, as such star could become a potential model calibrator for solar–like stars having convection as the main energy transport process in their cores. α Centauri A is of particular interest, since its dynamical mass is in the range (1.1 – 1.15 $M_{\odot}$; Aerts et al. 2010) over which models constructed at solar metallicity are expected to develop convective cores while in the main sequence. This has given rise to studies that aimed at establishing the nature of its core and at exploring the physics that affect core properties.

Following the revision of the dynamical mass of α Centauri A (Pourbaix and Boffin 2016), we carried out a detailed modelling of this star again allowing the nuclear reaction rates to vary, and found about 70% of best–fit models to have convective cores (see Chapter 5). More recently, Joyce and Chaboyer (2018) suggested that, if α Centauri A has a convective core, then it would be necessary to modify standard physical prescriptions (e.g., enhancing diffusion) in order to correctly model the star. Amongst the different model physics explored in Chapter 5 and in Bazot et al. (2016), the impact of the metallicity mixture on the core properties of α Centauri A has, however, not been investigated. In this chapter, we investigate the impact of the metallicity mixture on the inferred nature of the core of α Centauri A.

6.3 Model grids and observational constraints

To explore the impact of varying the metallicity mixture on the nature of the core of α Centauri A, we set up two grids (A and B) with the same model physics except for the metallicity mixture (see Table 6.1). The stellar evolution code MESA version 9793 was used to generate the grids. We set the metallicity mixture in Grid A according to Grevesse and Sauval (1998) with a solar surface heavy element mass fraction $Z_{\mathrm{surface},\odot} = 0.016$, while Grid B uses the metallicity mixture from Asplund et al. (2009) with $Z_{\mathrm{surface},\odot} = 0.0134$. The main motivation for considering these two mixtures goes back to the theoretically predicted sound speed profiles for solar models constructed with the different composition mixtures. Delahaye and Pinsonneault (2006) reported that solar models using the Grevesse and Sauval (1998) and Asplund

et al. (2009) mixtures yield a sound speed profile close to that of the real Sun, as opposed to models that use the Asplund et al. (2005) mixture (see Sect. 3.1.2). We used opacities from OPAL tables (Iglesias and Rogers 1996) at high temperatures, whereas at low temperatures tables from Ferguson et al. (2005) were used instead, for the respective metallicity mixtures. We employed the Joint Institute for Nuclear Astrophysics Reaction Library (JINA REACLIB; Cyburt et al. 2010) in both grids. The $^{14}N(p,\gamma)^{15}O$ and $^{12}C(\alpha,\gamma)^{16}O$ rates were described according to Imbriani et al. (2005) and Kunz et al. (2002), respectively. We note that the $^{12}C(\alpha,\gamma)^{16}O$ reaction rate is less relevant for stars on the main sequence phase but is vital in more evolved stars, i.e., stars at the core helium–burning evolution stage. Table 6.1 lists the macrophysics used

Table 6.1: Main features of the model grids adopted in this work.

Grid	Metallicity Mixture	Core Overshoot	Diffusion
A	Grevesse and Sauval (1998)	Yes	Yes
B	Asplund et al. (2009)	Yes	Yes

in either grid. We note that core overshoot was included as described by Herwig (2000) for models identified to have developed convective cores. Atomic diffusion was included in all our models according to Thoul et al. (1994). The latter is known to be a vital chemical transport process in low mass stars (e.g., Silva Aguirre et al. 2017, Nsamba et al. 2018b). The mixing length theory, as described by Böhm-Vitense (1958), was used to describe convection. We also implemented the Grey–Eddington atmosphere to integrate the atmospheric structure from the photosphere to an optical depth of 10^{-4}. The helium mass fraction (Y) was estimated using equation 3.5, with $\Delta Y/\Delta Z$ set to 2.0 and Y_0 is the big bang nucleosynthesis value set to 0.2484 (e.g., Cyburt et al. 2003).

Evolutionary tracks were evolved from the zero–age main sequence to the end of the subgiant evolution phase. The terminal criterion affecting the tracks is similar to that implemented in Chapter 5. The parameter space of the model grids is as follows: $M \in [1.0, 1.2]$ $M_\odot$ in steps of 0.01 $M_\odot$; mixing length parameter, $\alpha_{mlt} \in [1.3, 2.5]$ in steps of 0.1; overshoot parameter, $f_{ov} \in [0, 0.03]$ in steps of 0.005; and $Z \in [0.023, 0.039]$ in steps of 0.005. Each model grid contains about 156,000 models. The corresponding adiabatic oscillation frequencies of each model, for spherical degrees $l = 0$, 1, 2, and 3, were determined using GYRE (Townsend and Teitler, 2013). The surface effects were accounted for using the combined–term surface correction method described by Ball and Gizon (2014). This surface correction method has been reported to yield the least internal systematic uncertainties among the different available corrections (e.g., Nsamba et al. 2018b, Compton et al. 2018).

Table 6.2 displays the spectroscopic and interferometric constraints used in the optimization process. Run I adopts $T_{\rm eff}$ and [Fe/H] values obtained in Chapter 5. These spectroscopic constraints were complemented with the interferometric radius

Table 6.2: Spectroscopic and interferometric constraints.

Run	$T_{\rm eff}$ (K)	[Fe/H] (dex)	Radius ($R_\odot$)
I	5832 ± 62	0.23 ± 0.05	1.2310 ± 0.0036
II	5795 ± 19	0.23 ± 0.05	1.2234 ± 0.0053

from Pourbaix and Boffin (2016). Run II adopts $T_{\rm eff}$ and interferometric radius values from Kervella et al. (2016). We further note that Pourbaix et al. (2002) derived a dynamical mass of 1.105 ± 0.0070 $M_\odot$. This dynamical mass was then revised by Pourbaix and Boffin (2016), who obtained a value of 1.133 ± 0.0050 $M_\odot$.

Finally, the same asteroseismic constraints as in Chapter 5 were adopted. The Bayesian code AIMS, a software for fitting stellar pulsation data, was used as our optimization tool (see Sect. 3.2.5). Stellar parameters and their associated uncertainties were taken as the mean and standard deviation of the resulting posterior probability distribution functions (PDFs), as output by AIMS.

6.4 Discussion

Table 6.3 presents the stellar parameters determined using the model grids described in Table 6.1 and the sets of observables in Table 6.2. Our results show that we are able to reproduce the dynamical masses of Pourbaix and Boffin (2016) (Run I) and Pourbaix et al. (2002) (Run II) within 1σ (see Fig. 6.1 and Table 6.3). We note that the observed luminosity (i.e., 1.521 ± 0.015 $L_\odot$; Kervella et al. 2017) of α Centauri A was not included among the sets of observables as shown in Table 6.2. This is constrained via the combination of the interferometric radius and effective temperature. Our derived luminosity values are in agreement with the observed values (see Table 6.4). Run II and Run I luminosity values from both grids are consistent within 1σ and 2σ, respectively. The slight increase in luminosity values obtained in Run I is attributed to the larger interferometric radius used (see Table 6.2).

A clear difference can be seen in the right panel of Fig. 6.1 (Run II) between the stellar mass posterior PDFs obtained using the two grids. Since varying the metallicity mixture has been shown to have a minimum effect on the estimated stellar mass (Silva Aguirre et al. 2015, Nsamba et al. 2018b), this feature can instead be explained by the different core properties of the best–fit models. Table 6.3 shows that the number of

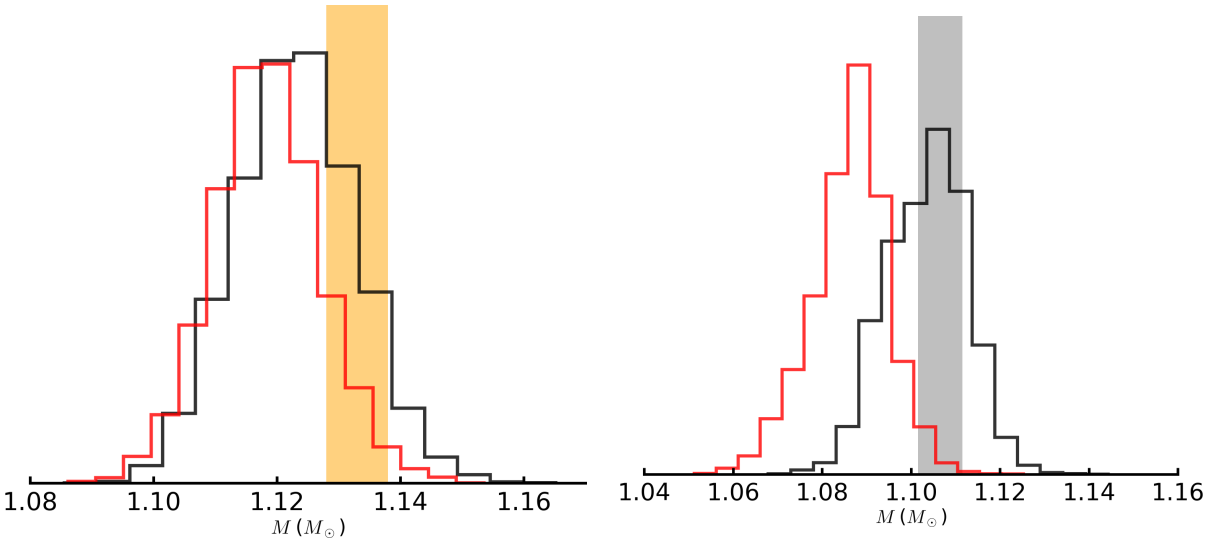

Figure 6.1: Run I (left) and Run II (right): Histograms represent the stellar mass posterior PDFs obtained using Grids A (red) and B (black). The dynamical masses (and corresponding uncertainties) of Pourbaix and Boffin (2016) and Pourbaix et al. (2002) are shown in orange and grey, respectively.

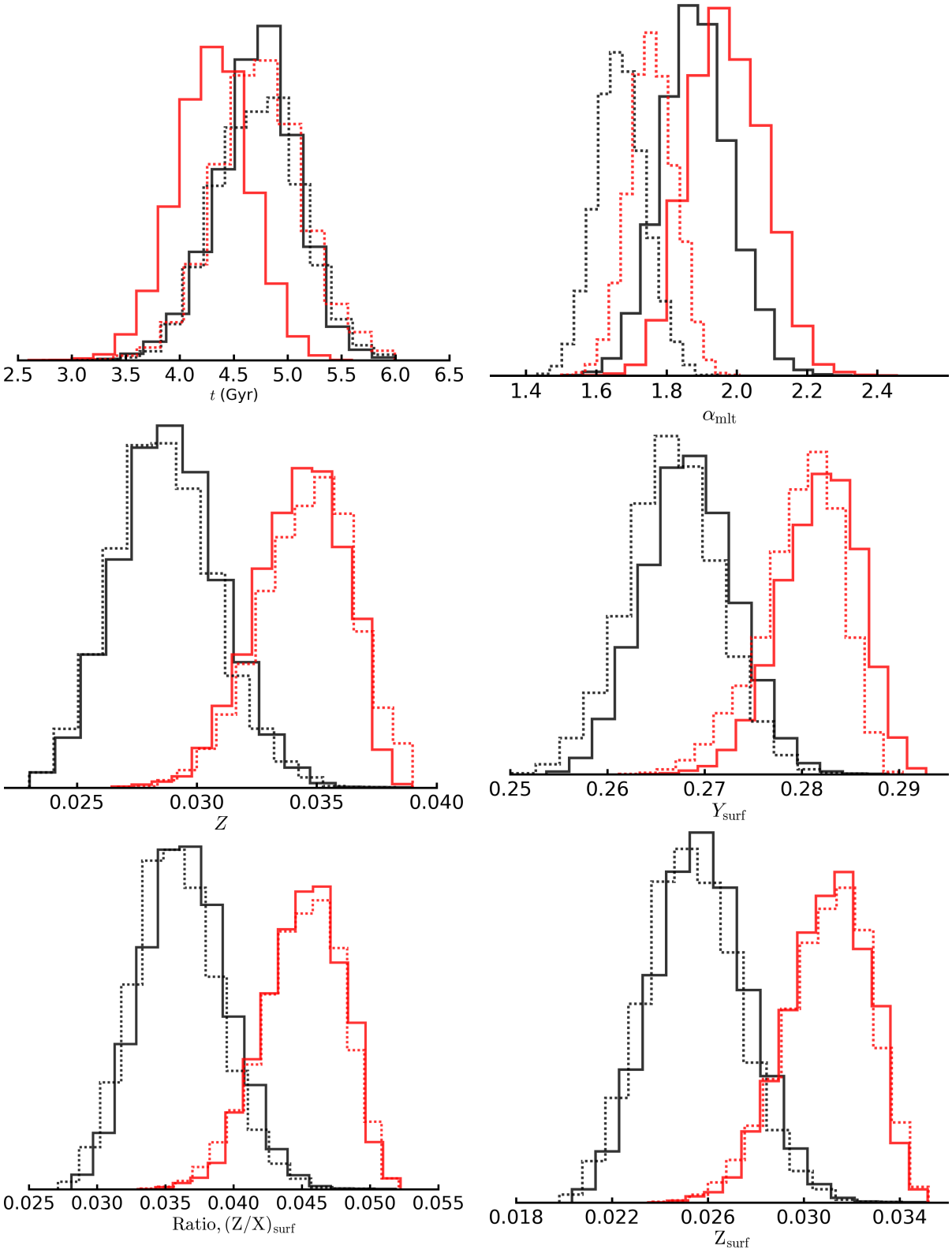

Figure 6.2: Histograms represent stellar parameter posterior PDFs obtained using different grids (Grid A in red and Grid B in black) and observational constraints (Run I as solid lines and Run II as dashed lines).

Table 6.3: Stellar parameters determined using different grids and observational constraints. The sixth column shows the percentage of best–fit models with convective cores, while the seventh column shows the upper convective–core mass limit.

Grid	Run	M ($M_\odot$)	t (Gyr)	$\alpha_{\rm mlt}$	Convective Core (%)	$M_{\rm c}$ ($M_\odot$)
A	I	1.12 ± 0.01	4.30 ± 0.35	1.97 ± 0.10	70	$\leqslant$ 0.085
	II	1.09 ± 0.01	4.74 ± 0.40	1.76 ± 0.07	46	$\leqslant$ 0.084
B	I	1.12 ± 0.01	4.72 ± 0.37	1.89 ± 0.10	79	$\leqslant$ 0.096
	II	1.10 ± 0.01	4.73 ± 0.39	1.67 ± 0.07	79	$\leqslant$ 0.092

Table 6.4: Luminosities and abundances determined using different grids and observational constraints.

Grid	Run	L ($L_\odot$)	Z	$Y_{\rm surf}$	$Z_{\rm surf}$	$(Z/X)_{\rm surf}$
A	I	1.703 ± 0.059	0.034 ± 0.002	0.282 ± 0.004	0.031 ± 0.002	0.045 ± 0.003
	II	1.502 ± 0.023	0.035 ± 0.002	0.279 ± 0.004	0.031 ± 0.002	0.045 ± 0.003
B	I	1.675 ± 0.063	0.028 ± 0.002	0.269 ± 0.005	0.026 ± 0.002	0.036 ± 0.003
	II	1.510 ± 0.022	0.028 ± 0.002	0.267 ± 0.005	0.025 ± 0.002	0.036 ± 0.003

best–fit models with convective cores changes from 46% to 79% when the metallicity mixture is changed from that of Grevesse and Sauval (1998) to that of Asplund et al. (2009). This happens since the dynamical mass of Pourbaix et al. (2002) lies within a range in which the onset of the CNO (carbon–nitrogen–oxygen) cycle, and thus core convection, is highly sensitive to the adopted metallicity mixture.

A different scenario is found when considering models that reproduce the dynamical mass of Pourbaix and Boffin (2016), with the stellar mass posterior PDFs showing excellent agreement (Run I; see left panel of Fig. 6.1). The percentage of models with convective cores is now consistent (i.e., $\gtrsim 70\%$) irrespective of the model grid adopted. We note that best–fit models are on average higher in mass compared to Run II and most have already developed convective cores, with any variation in the metallicity mixture generating no significant difference on their core properties.

In Table 6.3, we show the upper limits of the convective–core mass ($M_{\rm c}$) of our best–fit models. From all runs, we find the core radius to have an upper limit of 0.11 $R_{\odot}$. Bazot et al. (2012) derived an upper limit for the radius and the mass of a possible convective core in α Centauri A to be 0.059 $R_{\odot}$ and 0.035 $M_{\odot}$, respectively. These limits were derived while taking into account the small frequency separation ($\delta\nu$) in the optimisation, as this parameter can provide a direct estimation of the convective core characteristics. Furthermore, when exploring the contribution of the different model physics to the nature of the core of α Centauri A, Bazot et al. (2016), in their table 3, report the core radius of their best–fit models to vary between 0.026 and 0.084 $R_{\odot}$, which is consistent with our findings.

The top left panel of Fig. 6.2 shows that the derived stellar ages are in excellent agreement irrespective of the grid and observational constraints used. Furthermore, these ages are consistent with literature values (Kim 1999, Yıldız 2007, Bazot et al. 2016, Nsamba et al. 2018a, Joyce and Chaboyer 2018). Table 6.3 and the top right panel of Fig. 6.2 show that the $\alpha_{\rm mlt}$ estimated based on either Run I (solid lines) or Run II (dashed lines) are consistent within 1σ. The values of $\alpha_{\rm mlt}$ across runs are however different, this being mainly due to the different radius constraints used (see Table 6.2). We note that the interferometric radius measurements used in each run indirectly constrain the model mass. Moreover, $\alpha_{\rm mlt}$ is known to have a significant degree of correlation with the stellar mass and effective temperature (Pinheiro and Fernandes, 2013).

A clear contrast can be seen in the bottom panels of Fig. 6.2 between the best–fit models obtained using the two grids. As expected, the grid based on the metallicity mixture from Asplund et al. (2009) (Grid B) leads to best–fit models with a lower Z

compared to those based on the mixture from Grevesse and Sauval (1998) (Grid A). A similar feature can be seen for the surface helium mass fraction, $Y_{\rm surf}$.

The model properties that influence the onset of the CNO cycle (and associated convective core) include the adopted physics, metallicity, and mass. As mentioned in Sect. 6.3, both grids contain the same physics apart from the metallicity mixture. We note that models with high metallicity have a higher chance of developing convective cores. This is because a high metallicity leads to an increase in opacity, which in turn reduces the efficiency of radiative energy transport. This ultimately results in an increase in core temperature which favours the onset of the CNO cycle. Similarly, models with a higher mass have higher core temperatures, hence higher chances of developing a convective core. The top left panel of Fig. 6.3 shows that best–fit models with high mass develop large and massive convective cores. This could be explained by their high overshoot parameter values as shown in the bottom panel of Fig 6.3. Best–fit models with $f_{\rm ov} = 0$ have smaller core masses and radii. The top right panel of Fig. 6.3 shows no clear trend regarding the contribution from the initial metal mass fraction.

It is interesting to assess the dominant model property that facilitates the occurrence of convective cores for the best–fit models in either run. Despite the high metallicity of best–fit models from Grid A (Run II) (see bottom left panel of Fig. 6.2), the majority of these models have masses $\lesssim 1.1$ M$_\odot$ (see right panel of Fig. 6.1) resulting into 46% of models with convective cores. Grid B (Run II) contains most of the best–fit models with low metallicity but with masses $\gtrsim 1.1$ M$_\odot$ (see right panel of Fig. 6.1), leading to 79% of models with convective cores. Hence, for Run II (both grids), model mass is the dominant model property responsible for the onset of the CNO cycle.

For Grid A (Run I), it is challenging to determine the dominant model property that yields convective cores. This is because most of the best–fit models have masses $\gtrsim$ 1.1 M$_\odot$ and high metallicity (see left panel of Fig. 6.1 and bottom left panel of Fig. 6.2). However, for Grid B (Run I), the majority of best–fit models have low metallicity but masses $\gtrsim 1.1$ M$_\odot$, with 79% of models having convective cores. Therefore, also in this case model mass is the dominant model property contributing to the onset of the CNO cycle. Further, our results show that the mass range over which models constructed at different metallicities are expected to develop convective cores is 1.05 – 1.15 M$_\odot$.

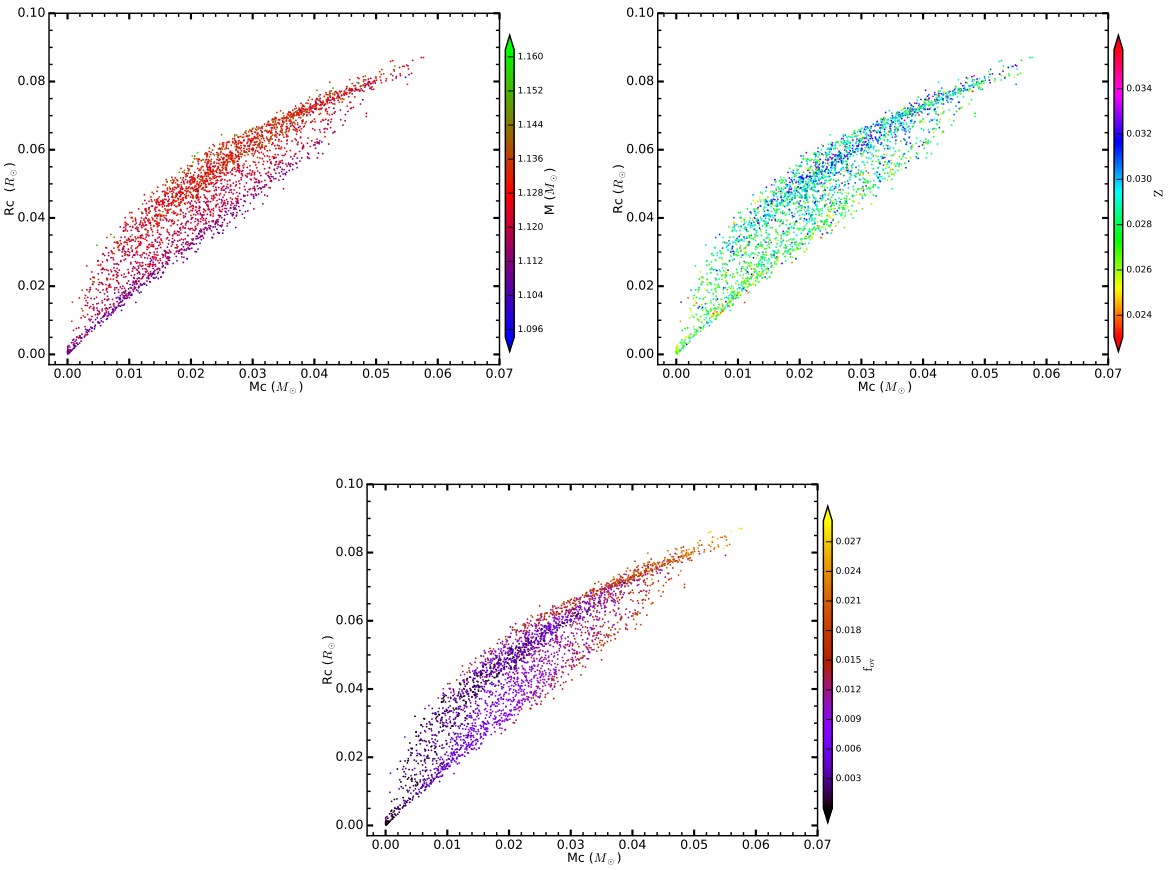

Figure 6.3: Scatter plots showing core radius (R_c) vs. core mass (M_c) for best–fit models with convective cores obtained using grid B (Run I). The top left panel is colour–coded according to the model mass (M), the top right panel according to the initial metal mass fraction (Z), and the bottom panel according to the overshoot parameter (f_{ov}).

6.5 Conclusions

In Chapter 5, we assessed the impact on the nature of the core of α Centauri A of varying the nuclear reaction rates, which showed that $\gtrsim 70\%$ of best–fit models reproducing the revised dynamical mass of Pourbaix and Boffin (2016) have convective cores. In this chapter, we expanded on the previous work by exploring the impact of varying the metallicity mixture (and corresponding opacities). Our findings show that $\gtrsim 70\%$ of best–fit models reproducing the revised dynamical mass have convective cores.

In sum, the percentage of best–fit models with convective cores remains above 70% when imposing the most up–to–date set of observational constraints. This happens

irrespective of the adopted metallicity mixture and nuclear reaction rates. Therefore, we propose that α Centauri A be adopted in the calibration of stellar model parameters when modelling solar–like stars with small convective cores.

During the "standard" solar calibration process, the initial metal mass fraction (Z), initial helium mass fraction (Y), and the mixing length parameter ($\alpha_{\rm mlt}$) are varied until a model is attained that satisfies the observed oscillation frequencies, effective temperature, metallicity, luminosity, and radius at the current solar age. The same model physics and solar calibrated parameters are then used to create grids for modelling other stars. Unlike the case of the Sun, there is no model–independent age for α Centauri A, but we do have a precise dynamical mass, interferometric radius, effective temperature, metallicity, and luminosity. In addition, we currently have ground–based seismic data, with the quality of those data expected to improve following the star's planned observations by space–based missions such as NASA's TESS and ESA's PLATO. This will improve the precision of observed oscillation frequencies and is also expected to increase the number of oscillation frequencies for all observable spherical degrees (l). This will support a more comprehensive asteroseismic analysis than the one presented in this chapter and in Chapter 5.

Therefore, with all these sets of observables, it will be possible to carry out a calibration procedure similar to the "standard" solar calibration routine briefly described above, without having the age among the constraints. It will also be feasible to provide effective constraints on some aspects of the physics, namely convection (mixing length, overshoot, surface effects), diffusion and opacities. The potential for constraining reaction rates is also a possibility when two or all stellar components of this triple system have seismic data of high precision available.

Chapter 7

Conclusions and outlook

This chapter highlights the most important findings of this thesis and the future prospects.

7.1 Conclusions

Before I highlight the conclusions of this thesis, I assess here the impact of including an interferometric radius as part of the observables in the asteroseismic optimisation process. This is essential because when exploring the physics that contributes towards the core properties of α Centauri A, an interferometric radius was included in the optimisation process (see Chapter 5 and Chapter 6). That being said, I demonstrate the relevance of an interferometric radius when coupled with other sets of observables towards constraining the stellar mass, and establish the precision needed on the interferometric radius beyond which its relevance in the optimisation process vanishes.

I employed the stellar grid GS98sta with the physics described in Sect. 4.4. The sets of observables included the seismic data (i.e., individual oscillation frequencies), classical constraints (i.e., metallicity and effective temperature), and an interferometric radius. I note that this exercise employs α Centauri A as a reference star, because it has a precisely determined interferometric radius and dynamical mass (e.g., Pourbaix et al. 2002, Kervella et al. 2003, 2017). The error on the interferometric radius was increased from 1σ to 18σ and, for every increment, the corresponding mass was derived. The top panel of Fig. 7.1 shows the trend of how the uncertainty on the derived stellar mass varies with the uncertainty on the interferometric radius. The uncertainty on the inferred mass is less than 1% when an interferometric radius with a precision below 1% is used in the optimisation process. The uncertainty on the inferred mass increases as that on the interferometric radius increases, and becomes approximately constant

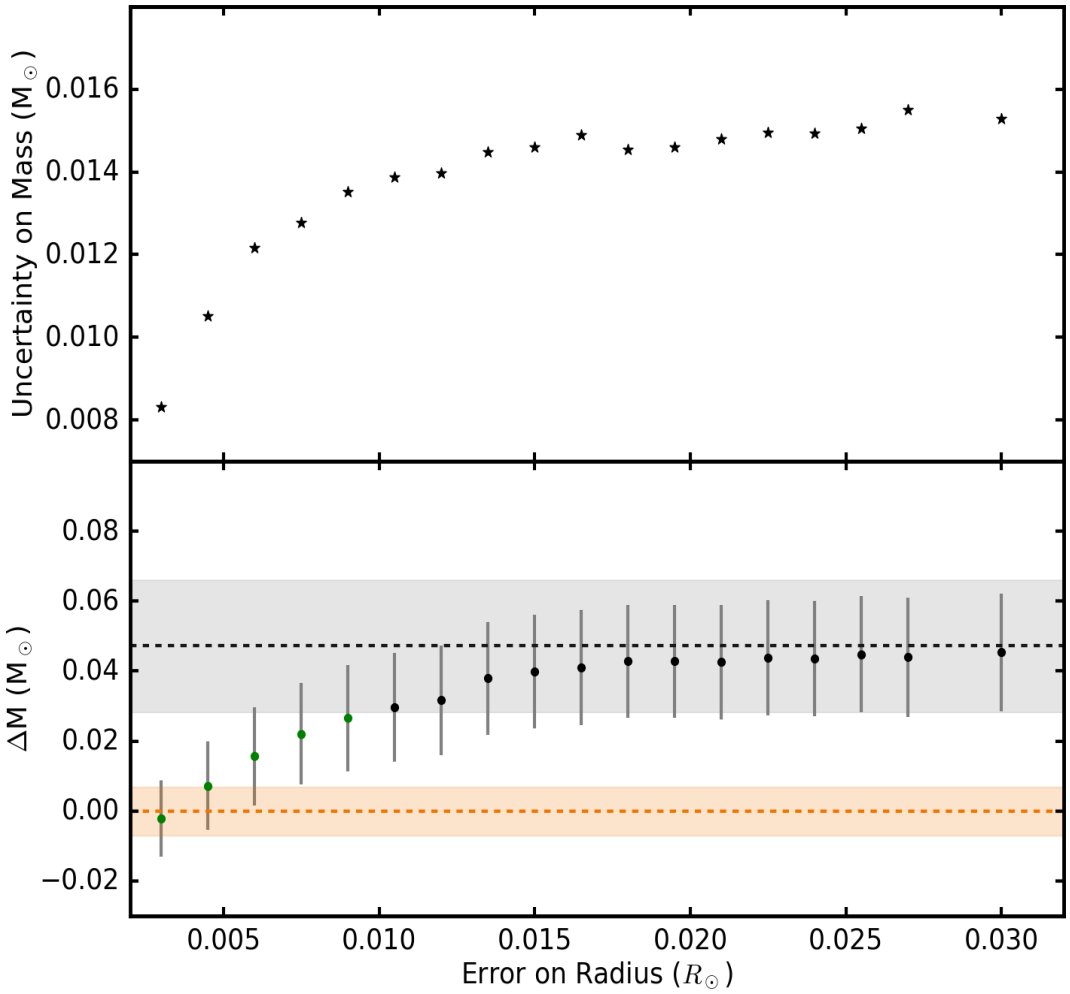

Figure 7.1: Bottom panel: ΔM is the difference between the dynamical mass and the derived stellar mass when the uncertainty on the interferometric radius is varied. The grey region shows the value of ΔM when the model mass is derived without the addition of an interferometric radius. The orange region shows the uncertainty on the dynamical mass. The top panel shows the trend on the derived stellar mass.

once the uncertainty on the interferometric radius is above $\sim$ 1.5%. The bottom panel of Fig. 7.1 shows that the dynamical stellar mass is accurately and precisely inferred when an interferometric radius with a precision below $\sim$ 1% is used in the optimisation process. The impact of the interferometric radius vanishes once its uncertainty is above $\sim$ 1.5% — seismic observables then dominate the determination of the stellar mass (grey region in Fig. 7.1). Furthermore, no significant improvement in the precision of the inferred stellar age is seen even when a radius with a precision below $\sim$ 1% is included in the optimisation process (see Fig. 7.2). These findings are consistent with the predictions of Creevey et al. (2007). Based on these findings, in order to

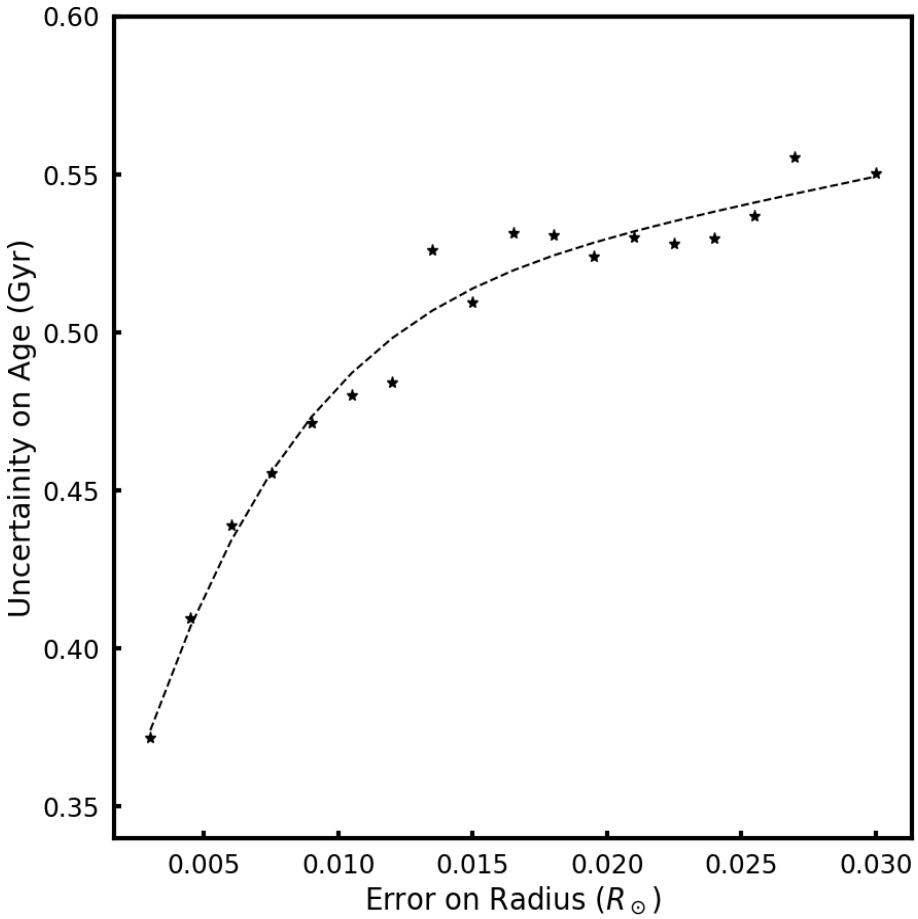

Figure 7.2: Variation of the uncertainty on the inferred stellar age as the uncertainty on the interferometric radius is varied. The dashed line is a fit through the derived values showing the trend of the uncertainty on age.

mitigate the systematic uncertainties of about 5% on the inferred astroseismic stellar mass (see bottom panel of Fig. 7.1) arising from the model physics and/or optimisation tool employed, it would be important to supplement the set of observables with an interferometric radius if available. I note that this is only useful if the precision on the interferometric radius is about $\sim$ 1%. This is expected to be the case for the brightest stars. A precision of at least 4% on the interferometric radius is expected for a majority of solar–type stars (e.g., Pijpers et al. 2003, Thévenin et al. 2005, North et al. 2007, Kervella 2008, Ligi et al. 2016). Based on my findings here and those of Creevey et al. (2007), this precision will not be sufficient to aid in constraining the stellar mass inferred using asteroseismic techniques.

The main conclusions emanating from this research work are the following:

(i) I draw the first conclusions of this work with respect to the surface term correction recipes. I echo that when the observed individual oscillation frequencies are used as seismic constraints, offsets exist when these are compared with theoretical oscillation frequencies. To correct for these differences, empirical relations have been suggested to mitigate this surface effect, as discussed in Sect. 3.2.3. To quantify the systematic uncertainties on the derived stellar parameters arising from the different surface correction methods, a very careful analysis subjecting the different correction methods to a grid of models with the same physics was carried out. The posterior probability distributions for stellar density, radius, mass, and age were obtained using surface correction relations. These stellar parameters were compared with those obtained using frequency ratios (Roxburgh and Vorontsov, 2003), which act as a reference to quantify the systematic uncertainties induced by the different surface correction methods. This is because frequency ratios are known to be insensitive to the surface layers. Among the different surface correction methods, and based on the findings of this thesis shown in Sect. 4.5.3, I conclude that the combined surface correction method of Ball and Gizon (2014) reproduces the stellar mean density, radius, mass, and age inferred by frequency ratios, with the lowest systematic uncertainties. A similar study has been carried out by Compton et al. (2018) for 67 stars, including the Sun and the *Kepler* Legacy sample. Their analysis was limited to only three surface correction approaches, i.e., the frequency correction power–law suggested by Kjeldsen et al. (2008), the cubic frequency term and the combined frequency terms of Ball and Gizon (2014). They reached similar conclusions as those presented in this thesis, yielding substantially better model fits when the combined cubic and inverse terms of Ball and Gizon (2014) are applied. The same conclusions have also been reached by Basu and Kinnane (2018). A rather interesting approach of mending the stellar model structural inadequacies is referred to as "patching", first suggested by Schlattl et al. (1997) and Rosenthal et al. (1999). Patching mainly involves correcting the structural contribution to the surface effect through substituting the envelope with mean stratifications from hydrodynamic simulations. A new scheme has been developed to mimic the structure of 3D envelopes, allowing for the interpolation of the mean 3D structure in effective temperature, gravitational acceleration, and metallicity (Jørgensen et al., 2017, Jørgensen et al., 2019). One drawback of this approach is that 3D hydrodynamic simulations are computationally expensive, thus its feasibility on large stellar grids is questionable. Jørgensen et al. (2019) compared their findings with results emanating from this thesis (i.e., presented

in Chapter 4.1), reaching similar conclusions. Based on the above, it may be possible to employ the parameter values from the combined surface correction of Ball and Gizon (2014) as a benchmark for other surface correction empirical relations. It is worth mentioning that the Lorentzian formulation suggested by Sonoi et al. (2015) also performs rather well and is consistent with findings of Jørgensen et al. (2019). The correction by Kjeldsen et al. (2008) has been shown to yield larger systematic uncertainties in radius, mass, and age than the combined surface correction of Ball and Gizon (2014). The largest discrepancies arise when the cubic surface correction term suggested by Ball and Gizon (2014) is applied.

(ii) I now highlight my conclusions on the model physics explored. One of the essential ingredients in stellar model grids is the choice of solar metallicity mixture. The estimated surface iron abundance in stellar models is compared to the observed [Fe/H] values determined using spectroscopic techniques. From equation 3.4, the observed [Fe/H] greatly depends on the solar reference considered, i.e., it assumes that the distribution of a fraction of each element comprising the metal mass fraction, Z, is based on the adopted solar abundance ratios. Unfortunately, the consistency of solar abundances is still far from being resolved (refer to Sect. 3.1.2 for details) — and the choice of solar metallicity mixture is thus left to the preference of the modeller. The findings in this thesis show that the systematic uncertainties on the derived stellar parameters (i.e., mean density, radius, mass, and age) are comparable to the statistical uncertainties as illustrated in Fig. 4.2. To put this into perspective, if I consider the two most commonly adopted metallicity mixtures (i.e., from Grevesse and Sauval 1998 and Asplund et al. 2009), for models computed with different solar metallicity mixtures but with the same (Z/X) at the surface, the theoretically determined [Fe/H] has a systematic difference of about 0.12 dex. This is consistent with the uncertainties on the observed [Fe/H] (for reference, see column three in table 4.1). Therefore, the systematic uncertainties on the inferred stellar parameters arising from variation in metallicity mixtures do not have a significant impact on the precision of the stellar parameters.

(iii) Variation in metallicity mixtures has been shown to have a significant impact on the model sound speed profile (see Fig. 3.3), — as it alters the chemical distribution in stellar interiors. In an effort to establish the core properties of α Centauri A, I investigated the impact of varying metallicity mixtures on the nature

of its core. A particularly interesting effect of varying metallicity mixtures can be examined when modelling stars with masses in the range 1.1 - 1.15 $M_{\odot}$. This is because stars in this mass range are in the transition region within which they develop a convective core while in the main–sequence. Increasing the metallicity leads to an increase in opacity, thus resulting in the reduction of the efficiency of radiative energy transport. This in turn results in an increase in core temperature favouring the onset of the CNO cycle. I stress that the largest discrepancies between solar metallicity mixtures are with respect to Carbon, Nitrogen, Oxygen, and Neon (e.g., Serenelli et al. 2009), which are needed in the CNO cycle. Hence, the impact of this microphysics on the core properties of a star such as α Centauri A can not be neglected. Furthermore, an assessment regarding the identification of the model properties that contribute to the existence of a convective core was made. In addition to the choice of solar metallicity mixture, the model mass and metallicity were identified, with models in the high–mass limit of the transition zone (i.e., 1.1 - 1.15 $M_{\odot}$) having higher chances of developing convective cores compared to their counterparts at the lower–mass end. However, I fail to draw any conclusions on the most dominant model property that contributes towards the onset of a convective core in stellar models within the transition region, being that this is rather an interplay of the model physics and model properties.

(iv) With the need to establish the core properties of α Centauri A, I explore the contribution of the nuclear reaction rates towards the onset of a convective core in stellar models that fit the seismic, spectroscopic, and interferometric observables. This was carried out considering the revised dynamical mass of α Centauri A (Pourbaix and Boffin, 2016). In addition, I extended a similar study considering the dynamical mass of α Centauri A suggested by Pourbaix et al. (2002). This was done to explore the consistency/robustness of my findings with those of Bazot et al. (2016) that, which were based on this mass. The cause of the discrepancies in the dynamical masses of α Centauri A is discussed in Sect. 5.2. I adopted the nuclear reaction rates of the NACRE collaboration (Angulo et al., 1999) and JINA REACLIB (Cyburt et al., 2010). An important difference between these nuclear reaction rate options is in the specific rate for $^{14}\mathrm{N}(p,\gamma)^{15}\mathrm{O}$. This reaction rate is essential for the CNO cycle and its variation is expected to significantly affect the chances of a model developing a convective core. The impact of varying nuclear reaction rates has no significant impact on the global stellar parameters such as radius, mass, and age, but it impacts on the onset of the CNO cycle and

therefore plays a significant role towards the onset of a convective core in stars with masses in the transition zone.

(v) From the exploration of the microphysics, i.e., metallicity mixtures and nuclear reaction rates, and their contribution to the nature of the core of α Centauri A, the results in this thesis show that $\gtrsim 70\%$ of the acceptable models suggest that α Centauri A has a convective core. Considering the dynamical mass of Pourbaix et al. (2002), my findings show that the number of acceptable models with convective cores varies significantly once the nuclear reaction rates are changed. This is consistent with findings of Bazot et al. (2016) indicating that there is only a 40% possibility for α Centauri A to have a convective core. A better procedure to ascertain the existence of a convective core in α Centauri A is using frequency ratios (Roxburgh and Vorontsov, 2003), since they carry information on the internal properties of the star. Unfortunately, the current available ground–based seismic data has missing modes and frequency ratios were only possible for a few modes. The comparison based on only a handful of possible observed frequency ratios shows that models with convective cores provide a better fit than those with radiative cores. The results presented in this thesis favour the existence of a convective core in α Cenaturi A, which may potentially be adopted in the calibration of stellar model parameters when modelling solar–like stars with convective cores. Based on the expected space observations by the recently launched NASA's TESS and the future ESA's PLATO missions, the precision and number of frequency modes is expected to increase. This will facilitate a detailed investigation similar to that carried out by Silva Aguirre et al. (2013) based on frequency ratios. The improved seismic data, when coupled with all the available observables (i.e., spectroscopic observables, interferometric radius, and dynamical mass measurements), will provide an opportunity for tightly constraining the essential model physics, such as convection (mixing length, overshoot, surface effects), diffusion, and opacities.

(vi) Atomic diffusion is one of the vital model input physics explored in this thesis and was implemented in the stellar grids according to Thoul et al. (1994). I note that atomic diffusion as considered here takes into account diffusion of hydrogen and gravitational settling of heavy elements, mainly, ^{4}He, ^{16}O, and ^{56}Fe without radiative acceleration. Inclusion of atomic diffusion in stellar grid construction increases the model computation time. It is for this reason that atomic diffusion is not included by some modellers (e.g., Silva Aguirre et al. 2017). I therefore

quantified the systematic uncertainties on the derived stellar parameters arising from exclusion of this model physics input. The results show that exclusion of atomic diffusion has a significant impact on stellar mass and age with systematic uncertainties of 2.1%, and 16%, respectively. These systematic uncertainties are larger than the statistical uncertainties (see Fig. 4.2). Taking the Sun as a reference star, since this study is restricted to low–mass stars, the accurate age of the Sun can only be reproduced from forward modelling procedures when atomic diffusion is included in the stellar grids (see table 3.1). This is because atomic diffusion enhances the diffusion of hydrogen from the stellar core, reducing the amount of fuel needed to keep the star for a longer period of time in the main–sequence. Furthermore, gravitational settling of heavy elements yields the correct surface abundances for the Sun. Based on these results, I confirm that atomic diffusion is a vital chemical transport process in stars with a mass close to that of the Sun (e.g., Basu and Antia 1994, Bahcall et al. 1995, Richard et al. 1996, Vauclair 1998, Yang et al. 2001, Gorshkov and Baturin 2008). If neglected, the systematic uncertainties found in this thesis should be taken into account when deriving stellar parameters.

7.2 Outlook

Exploring the systematic uncertainties on the stellar parameters inferred through asteroseismic forward modelling is essential because these affect the conclusions drawn on stellar physics, stellar interior structure and evolution. Furthermore, this has vital implications to other research fields such as exoplanet and Galactic archeology (i.e., study of the structure and evolution of the Milky way galaxy by measuring ages and chemical compositions of its stellar populations) studies. Therefore, it is essential to account for all the sources of systematic uncertainties on the derived stellar parameters, namely mean density, radius, mass, and age. The research work carried out in this thesis is limited to solar–type stars with masses below ~ 1.2 $M_{\odot}$. This implies that the impact of the model physics employed when modelling main–sequence stars with masses above ~ 1.2 $M_{\odot}$ was not explored. It is worth extending this research work to solar–type stars with convective cores, i.e., stars with masses in the range [1.2 - 1.6] $M_{\odot}$.

One of the essential model physics worth exploring in details in such stars is atomic diffusion. Atomic diffusion is commonly neglected when modelling main–sequence stars with convective cores. This is because it results in over settling of heavy elements

in models with masses above $\sim$ 1.2 $M_{\odot}$ (e.g., Goupil 2018). This is thought to be counteracted by the inclusion of other chemical transport processes such as radiative acceleration and rotation (e.g., Turcotte et al. 1998, Dotter et al. 2017, Deal et al. 2018). Inclusion of model physics such as rotation has a significant impact on the stellar oscillations which needs to be accounted for (e.g., Suárez et al. 2006, Goupil 2011). It is also worth stressing that inclusion of chemical processes, like radiative acceleration, in the modelling routines of large stellar grids is costly in terms of computational time. This is one of the reasons why it is ignored in the modelling routines. *To this end, apart from extensive exploration of chemical transport processes that can counteract the effects of atomic diffusion on the model surface elements, it is worth quantifying systematic uncertainties on the derived stellar parameters when atomic diffusion is neglected.*

In addition, the boundary between a convective core and the adjacent radiative region for stars above $\sim$ 1.2 $M_{\odot}$ is said to be "soft" in the sense that material driven by convection from the core can penetrate into the radiative region. This extends the convective region (hence the term "core overshoot") and increases the core size, with a significant impact on the stellar parameters derived through forward modelling techniques (e.g., Lebreton et al. 2014, Claret and Torres 2016, 2017, Goupil 2018, Claret and Torres 2018). For instance, the central hydrogen in the nearby radiative regions could be transported by convection into the core of the star. This impacts on the lifetime a star spends on the main–sequence. *It is therefore essential to extensively examine the relationship between core overshoot and stellar parameters, such as mass and age, and constrain convective core sizes.*

The available *Kepler* seismic data for stars in the mass range 1.1 - 1.6 $M_{\odot}$ (e.g., Lund et al. 2017) carries essential information about the stellar core, — presenting an opportunity to extend the works of Claret and Torres (2017) and Claret and Torres (2018), whose study sample does not contain seismic data. Furthermore, the number of solar–type stars having seismic data with masses in the range 1.1 - 1.6 $M_{\odot}$ is expected to increase with the ongoing TESS observations.

References

Adelberger, E. G., García, A., Robertson, R. G. H., Snover, K. A., Balantekin, A. B., Heeger, K., et al. (2011). Solar fusion cross sections. ii. the *pp* chain and cno cycles. *Rev. Mod. Phys.* 83, 195–245. doi: 10.1103/RevModPhys.83.195

Aerts, C., Christensen-Dalsgaard, J., and Kurtz, D. W. (2010). *Asteroseismology, Astronomy and Astrophysics Library. ISBN 978-1-4020-5178-4.*

Allen, C. W. (1976). *Astrophysical Quantities* (3rd edition, Athlone Press)

Aller, L. H. and Chapman, S. (1960). Diffusion in the Sun. *ApJ* 132, 461. doi: 10.1086/146943

Anders, E. and Grevesse, N. (1989). Abundances of the elements - Meteoritic and solar. *GeCoA* 53, 197–214. doi:10.1016/0016-7037(89)90286-X

Angulo, C., Arnould, M., Rayet, M., Descouvemont, P., Baye, D., Leclercq-Willain, C., et al. (1999). A compilation of charged-particle induced thermonuclear reaction rates. *Nuclear Physics A* 656, 3–183. doi: 10.1016/S0375-9474(99)00030-5

Asplund, M., Grevesse, N., and Sauval, A. J. (2005). The Solar Chemical Composition. In *Cosmic Abundances as Records of Stellar Evolution and Nucleosynthesis*, eds. T. G. Barnes, III and F. N. Bash. vol. 336 of *Astronomical Society of the Pacific Conference Series*, 25

Asplund, M., Grevesse, N., Sauval, A. J., and Scott, P. (2009). The Chemical Composition of the Sun. *Annual Review of Astron and Astrophys* 47, 481–522. doi: 10.1146/annurev.astro.46.060407.145222

Badnell, N. R., Bautista, M. A., Butler, K., Delahaye, F., Mendoza, C., Palmeri, P., et al. (2005). Updated opacities from the Opacity Project. *MNRAS* 360, 458–464. doi:10.1111/j.1365-2966.2005.08991.x

Baglin, A., Auvergne, M., Boisnard, L., Lam-Trong, T., Barge, P., Catala, C., et al. (2006). CoRoT: a high precision photometer for stellar evolution and exoplanet finding. In *36th COSPAR Scientific Assembly.* vol. 36 of *COSPAR Meeting*

Bahcall, J. N., Pinsonneault, M. H., and Wasserburg, G. J. (1995). Solar models with helium and heavy-element diffusion. *Reviews of Modern Physics* 67, 781–808. doi:10.1103/RevModPhys.67.781

Ball, W. H. and Gizon, L. (2014). A new correction of stellar oscillation frequencies for near-surface effects. *A&A* 568, A123. doi:10.1051/0004-6361/201424325

Ball, W. H. and Gizon, L. (2017). Surface-effect corrections for oscillation frequencies of evolved stars. *A & A* 600, A128. doi: 10.1051/0004-6361/201630260

Balona, L. A. (2010). *Challenges In Stellar Pulsation, Bentham Publishers, ISBN: 978-1-60805-185-4*

Balona, L. A. (2018). Pulsation in Intermediate-Mass Stars. *Frontiers in Astronomy and Space Sciences* 5, 43. doi: 10.3389/fspas.2018.00043

Balser, D. S. (2006). The Chemical Evolution of Helium. *Astronomical Journal* 132, 2326–2332. doi:10.1086/508515

Basu, S. (2018). Helioseismic Tests of Stellar Equations of State and Opacities. In *Workshop on Astrophysical Opacities.* vol. 515 of *Astronomical Society of the Pacific Conference Series*, 13

Basu, S. and Antia, H. M. (1994). Effects of Diffusion on the Extent of Overshoot Below the Solar Convection Zone. *MNRAS* 269, 1137. doi:10.1093/mnras/269.4.1137

Basu, S. and Antia, H. M. (2004). Constraining Solar Abundances Using Helioseismology. *ApJL* 606, L85–L88. doi: 10.1086/421110

Basu, S. and Antia, H. M. (2008). Helioseismology and solar abundances. *Phys. Rep.* 457, 217–283. doi:10.1016/j.physrep.2007.12.002

Basu, S. and Chaplin, W. J. (2019). *Chapter 4 - Helioseismic Inferences on the Internal Structure and Dynamics of the Sun*. 87–125. doi:10.1016/B978-0-12-814334-6.00004-2

Basu, S., Chaplin, W. J., and Elsworth, Y. (2010). Determination of Stellar Radii from Asteroseismic Data. *ApJ* 710, 1596–1609. doi:10.1088/0004-637X/710/2/1596

Basu, S. and Kinnane, A. (2018). The Robustness of Asteroseismic Estimates of Global Stellar Parameters to Surface Term Corrections. *ApJ* 869, 8. doi:10.3847/1538-4357/aae922

Bazot, M., Bouchy, F., et al. (2007). Asteroseismology of α Centauri A. Evidence of rotational splitting. *A & A* 470, 295–302. doi:10.1051/0004-6361:20065694

Bazot, M., Bourguignon, S., and Christensen-Dalsgaard, J. (2008). Estimation of stellar parameters using Monte Carlo Markov Chains. *Mem. Soc. Astron. Ital.* 79, 660

Bazot, M., Bourguignon, S., et al. (2012). A Bayesian approach to the modelling of α Cen A. *MNRAS* 427, 1847–1866. doi: 10.1111/j.1365-2966.2012.21818.x

Bazot, M., Christensen-Dalsgaard, J., Gizon, L., and Benomar, O. (2016). On the uncertain nature of the core of α Cen A. *MNRAS* 460, 1254–1269. doi:10.1093/mnras/stw921

Beck, P. G., Kambe, E., Hillen, M., Corsaro, E., Van Winckel, H., Moravveji, E., et al. (2015). Detection of solar-like oscillations in the bright red giant stars γ Piscium and θ^1 Tauri from a 190-day high-precision spectroscopic multi-site campaign. *A&A* 573, A138. doi:10.1051/0004-6361/201323019

Bedding, T. R., Butler, R. P., Kjeldsen, H., Baldry, I. K., O'Toole, S. J., Tinney, C. G., et al. (2001). Evidence for Solar-like Oscillations in β Hydri. *ApJL* 549, L105–L108. doi:10.1086/319139

Bedding, T. R. and Kjeldsen, H. (2003). Solar-like Oscillations. *Publications of the Astronomical Society of Australia* 20, 203–212. doi:10.1071/AS03025

Bedding, T. R., Kjeldsen, H., Bouchy, F., Bruntt, H., Butler, R. P., Buzasi, D. L., et al. (2005). The non-detection of oscillations in Procyon by MOST: Is it really a surprise? *A & A* 432, L43–L48. doi: 10.1051/0004-6361:200500019

Bellinger, E. P. (2019). Inverse problems in asteroseismology. *ArXiv* abs/1808.06649

Bellinger, E. P., Angelou, G. C., Hekker, S., Basu, S., Ball, W. H., and Guggenberger, E. (2016). Fundamental Parameters of Main-Sequence Stars in an Instant with Machine Learning. *ApJ* 830, 31. doi: 10.3847/0004-637X/830/1/31

Benomar, O., Masuda, K., Shibahashi, H., and Suto, Y. (2014). Determination of three-dimensional spin-orbit angle with joint analysis of asteroseismology, transit lightcurve, and the Rossiter-McLaughlin effect: Cases of HAT-P-7 and Kepler-25. *PASJ* 66, 94. doi:10.1093/pasj/psu069

Böhm-Vitense, E. (1958). Über die Wasserstoffkonvektionszone in Sternen verschiedener Effektivtemperaturen und Leuchtkräfte. Mit 5 Textabbildungen. *Zeit. Astrophys.* 46, 108

Bonaca, A., Tanner, J. D., Basu, S., Chaplin, W. J., Metcalfe, T. S., Monteiro, M. J. P. F. G., et al. (2012). Calibrating Convective Properties of Solar-like Stars in the Kepler Field of View. *ApJL* 755, L12. doi:10.1088/2041-8205/755/1/L12

Borucki, W. J., Koch, D., Basri, G., Batalha, N., Brown, T., Caldwell, D., et al. (2010). Kepler Planet-Detection Mission: Introduction and First Results. *Science* 327, 977. doi:10.1126/science.1185402

Bouchy, F. and Carrier, F. (2002). The acoustic spectrum of alpha Cen A. *A & A* 390, 205–212. doi:10.1051/0004-6361:20020706

Brandão, I. M., Doğan, G., Christensen-Dalsgaard, J., Cunha, M. S., Bedding, T. R., Metcalfe, T. S., et al. (2011). Asteroseismic modelling of the solar-type subgiant star β Hydri. *A & A* 527, A37. doi:10.1051/0004-6361/201015370

Brandão, I. M. et al. (2014). On the inference of stellar ages and convective-core properties in main-sequence solar-like pulsators. *MNRAS* 438, 1751–1761. doi:10.1093/mnras/stt2314

Brown, T. M. and Gilliland, R. L. (1994). Asteroseismology. *ARA&A* 32, 37–82. doi:10.1146/annurev.aa.32.090194.000345

Brown, T. M., Gilliland, R. L., Noyes, R. W., and Ramsey, L. W. (1991). Detection of possible p-mode oscillations on Procyon. *ApJ* 368, 599–609. doi:10.1086/169725

Bucaro, J. A., Houston, B. H., and Williams, E. G. (1991). Fiber-optic air-backed hydrophone transduction mechanisms. *Acoustical Society of America Journal* 89, 451–453. doi:10.1121/1.400481

Burgers, J. M. (1969). *Flow Equations for Composite Gases*

Butler, R. F., Shearer, J. A. L., and Redfern, R. M. (1996). Crowded Field Photometry of M15 Using the TRIFFID Camera. *Irish Astronomical Journal* 23

Campante, T. L. (2012). *Asteroseismology: Data Analysis Methods and Interpretation for Space and Ground-based Facilities*. Ph.D. thesis, PhDT Thesis, Universidade do Porto

Campante, T. L., Lund, M. N., Kuszlewicz, J. S., Davies, G. R., Chaplin, W. J., Albrecht, S., et al. (2016). Spin-Orbit Alignment of Exoplanet Systems: Ensemble Analysis Using Asteroseismology. *ApJ* 819, 85. doi:10.3847/0004-637X/819/1/85

Campante, T. L., Santos, N. C., and Monteiro, M. J. P. F. G. (2017). Asteroseismology and Exoplanets: Proceedings of the IVth Azores International Advanced School in Space Sciences. *ArXiv e-prints*

Casagrande, L., Flynn, C., Portinari, L., Girardi, L., and Jimenez, R. (2007). The helium abundance and $\Delta Y/\Delta Z$ in lower main-sequence stars. *MNRAS* 382, 1516–1540. doi:10.1111/j.1365-2966.2007.12512.x

Casagrande, L., Schoenrich, R., Asplund, M., Cassisi, S., Ramirez, I., Melendez, J., et al. (2011). VizieR Online Data Catalog: Geneva-Copenhagen survey re-analysis (Casagrande+, 2011). *VizieR Online Data Catalog* , J/A+A/530/A138

Casagrande, L., Silva Aguirre, V., Stello, D., Huber, D., Serenelli, A. M., Cassisi, S., et al. (2014). Strömgren Survey for Asteroseismology and Galactic Archaeology: Let the SAGA Begin. *ApJ* 787, 110. doi:10.1088/0004-637X/787/2/110

Chaplin, W. J., Basu, S., Huber, D., Serenelli, A., Casagrande, L., Silva Aguirre, V., et al. (2014). Asteroseismic Fundamental Properties of Solar-type Stars Observed by the NASA Kepler Mission. *ApJS* 210, 1. doi:10.1088/0067-0049/210/1/1

Chaplin, W. J., Elsworth, Y., Howe, R., Isaak, G. R., McLeod, C. P., Miller, B. A., et al. (1996). BiSON Performance. *Solar Physics* 168, 1–18. doi:10.1007/BF00145821

Chaplin, W. J., Houdek, G., Appourchaux, T., Elsworth, Y., New, R., and Toutain, T. (2008). Challenges for asteroseismic analysis of Sun-like stars. *A&A* 485, 813–822. doi:10.1051/0004-6361:200809695

Chaplin, W. J., Kjeldsen, H., Christensen-Dalsgaard, J., Basu, S., Miglio, A., Appourchaux, T., et al. (2011). Ensemble Asteroseismology of Solar-Type Stars with the NASA Kepler Mission. *Science* 332, 213. doi:10.1126/science.1201827

Chaplin, W. J. and Miglio, A. (2013). Asteroseismology of solar-type and red-giant

stars. *Annual Review of Astronomy and Astrophysics* 51, 353–392. doi:10.1146/annurev-astro-082812-140938

Chaplin, W. J. and Miglio, A. (2013). Asteroseismology of Solar-Type and Red-Giant Stars. *ARAA* 51, 353–392. doi:10.1146/annurev-astro-082812-140938

Chapman, S. (1917a). Convection and diffusion within giant stars. *MNRAS* 77, 540. doi:10.1093/mnras/77.7.540

Chapman, S. (1917b). Thermal diffusion and the stars. *MNRAS* 77, 539. doi:10.1093/mnras/77.7.539

Chiosi, C., Bertelli, G., and Bressan, A. (1992). New developments in understanding the HR diagram. *ARA&A* 30, 235–285. doi:10.1146/annurev.aa.30.090192.001315

Chiosi, C. and Matteucci, F. M. (1982). The helium to heavy element enrichment ratio, Delta Y/Delta Z. *A & A* 105, 140–148

Christensen-Dalsgaard, J. (2002). Helioseismology. *Reviews of Modern Physics* 74, 1073–1129. doi:10.1103/RevModPhys.74.1073

Christensen-Dalsgaard, J. (2008). Adipls—the aarhus adiabatic oscillation package. *Astrophysics and Space Science* 316, 113–120. doi:10.1007/s10509-007-9689-z

Christensen-Dalsgaard, J. (2009). The Sun as a fundamental calibrator of stellar evolution. In *The Ages of Stars*. vol. 258 of *IAU Symposium*, 431–442

Christensen-Dalsgaard, J., Dappen, W., Ajukov, S. V., Anderson, E. R., Antia, H. M., Basu, S., et al. (1996). The Current State of Solar Modeling. *Science* 272, 1286–1292. doi:10.1126/science.272.5266.1286

Christensen-Dalsgaard, J., Dappen, W., and Lebreton, Y. (1988). Solar oscillation frequencies and the equation of state. *Nature* 336, 634–638. doi:10.1038/336634a0

Christensen-Dalsgaard, J., Monteiro, M. J. P. F. G., Rempel, M., and Thompson, M. J. (2011). A more realistic representation of overshoot at the base of the solar convective envelope as seen by helioseismology. *MNRAS* 414, 1158–1174. doi:10.1111/j.1365-2966.2011.18460.x

Christensen-Dalsgaard, J., Proffitt, C. R., and Thompson, M. J. (1993a). Effects of Diffusion on Solar Models and Their Oscillation Frequencies. *ApJ* 403, L75. doi:10.1086/186725

Christensen-Dalsgaard, J., Proffitt, C. R., and Thompson, M. J. (1993b). Effects of diffusion on solar models and their oscillation frequencies. *ApJ* 403, L75–L78. doi:10.1086/186725

Christensen-Dalsgaard, J. and Thompson, M. J. (1997). On solar p-mode frequency shifts caused by near-surface model changes. *MNRAS* 284, 527–540. doi:10.1093/mnras/284.3.527

Claret, A. and Torres, G. (2016). The dependence of convective core overshooting on stellar mass. *A&A* 592, A15. doi:10.1051/0004-6361/201628779

Claret, A. and Torres, G. (2017). The Dependence of Convective Core Overshooting on Stellar Mass: A Semi-empirical Determination Using the Diffusive Approach with Two Different Element Mixtures. *ApJ* 849, 18. doi:10.3847/1538-4357/aa8770

Claret, A. and Torres, G. (2018). The Dependence of Convective Core Overshooting on Stellar Mass: Additional Binary Systems and Improved Calibration. *ApJ* 859, 100. doi:10.3847/1538-4357/aabd35

Claverie, A., Isaak, G. R., McLeod, C. P., van der Raay, H. B., and Cortes, T. R. (1979). Solar structure from global studies of the 5-minute oscillation. *Nature* 282, 591–594. doi:10.1038/282591a0

Coelho, H. R., Chaplin, W. J., Basu, S., Serenelli, A., Miglio, A., and Reese, D. R. (2015). A test of the asteroseismic ν_{max}

scaling relation for solar-like oscillations in main-sequence and subgiant stars. *MNRAS* 451, 3011–3020. doi:10.1093/mnras/stv1175

Collins, G. W. (1989). *The fundamentals of stellar astrophysics* (New York, W. H. Freeman and Co.)

Compton, D. L., Bedding, T. R., Ball, W. H., Stello, D., Huber, D., White, T. R., et al. (2018). Surface correction of main-sequence solar-like oscillators with the Kepler LEGACY sample. *MNRAS* 479, 4416–4431. doi:10.1093/mnras/sty1632

Cox, A. N. and Tabor, J. E. (1976). Radiative opacity tables for 40 stellar mixtures. *The Astrophysical Journal Supplement Series* 31, 271–312. doi:10.1086/190383

Cox, J. D., I (1980). *Theory of stellar pulsation* (Research supported by the National Science Foundation. Princeton University Press)

Cox, J. P. and Smith, R. C. (1981). Book-Review - Theory of Stellar Pulsation. *The Observatory* 101, 87

Creevey, O. L. et al. (2007). The Complementary Roles of Interferometry and Asteroseismology in Determining the Mass of Solar-Type Stars. *ApJ* 659, 616–625. doi:10.1086/512097

Cunha, M. S. and Metcalfe, T. S. (2007). Asteroseismic Signatures of Small Convective Cores. *ApJ* 666, 413–422. doi:10.1086/520045

Cyburt, R. H. et al. (2003). Primordial nucleosynthesis in light of WMAP. *Physics Letters B* 567, 227–234. doi:10.1016/j.physletb.2003.06.026

Cyburt, R. H. et al. (2010). The jina reaclib database: Its recent updates and impact on type-i x-ray bursts. *ApJS* 189, 240

Davies, G. R., Silva Aguirre, V., Bedding, T. R., Handberg, R., Lund, M. N., Chaplin, W. J., et al. (2016). Oscillation frequencies for 35 Kepler solar-type planet-hosting stars using Bayesian techniques and machine learning. *MNRAS* 456, 2183–2195. doi:10.1093/mnras/stv2593

de Boer, K. and Seggewiss, W. (2008). *Stars and Stellar Evolution* (EDP Sciences)

de Meulenaer, P. et al. (2010). Core properties of α Centauri A using asteroseismology. *A & A* 523, A54. doi:10.1051/0004-6361/201014966

Deal, M., Alecian, G., Lebreton, Y., Goupil, M. J., Marques, J. P., LeBlanc, F., et al. (2018). Impacts of radiative accelerations on solar-like oscillating main-sequence stars. *A&A* 618, A10. doi:10.1051/0004-6361/201833361

Deheuvels, S., Brandão, I., Silva Aguirre, V., Ballot, J., Michel, E., Cunha, M. S., et al. (2016). Measuring the extent of convective cores in low-mass stars using Kepler data: toward a calibration of core overshooting. *A&A* 589, A93. doi:10.1051/0004-6361/201527967

Deheuvels, S., Doğan, G., Goupil, M. J., Appourchaux, T., Benomar, O., Bruntt, H., et al. (2014). Seismic constraints on the radial dependence of the internal rotation profiles of six Kepler subgiants and young red giants. *A & A* 564, A27. doi:10.1051/0004-6361/201322779

Deheuvels, S. and Michel, E. (2011). Constraints on the structure of the core of subgiants via mixed modes: the case of HD 49385. *A & A* 535, A91. doi:10.1051/0004-6361/201117232

Delahaye, F. and Pinsonneault, M. H. (2006). The solar heavy-element abundances. i. constraints from stellar interiors. *The Astrophysical Journal* 649, 529–540. doi:10.1086/505260

Di Mauro, M. P. (2016). A review on Asteroseismology. In *Frontier Research in Astrophysics II*. 29

Dotter, A., Conroy, C., Cargile, P., and Asplund, M. (2017). The Influence of Atomic

Diffusion on Stellar Ages and Chemical Tagging. *ApJ* 840, 99. doi:10.3847/1538-4357/aa6d10

Dziembowski, W. (1977). Light and radial velocity variations in a nonradially oscillating star. *Acta Astronomica* 27, 203–211

Dziembowski, W. A. and Pamiatnykh, A. A. (1993). The opacity mechanism in B-type stars. I - Unstable modes in Beta Cephei star models. *MNRAS* 262, 204–212. doi:10.1093/mnras/262.1.204

Dziembowski, W. A., Paterno, L., and Ventura, R. (1988). How comparison between observed and calculated p-mode eigenfrequencies can give information on the internal structure of the sun. *A & A* 200, 213–217

Eddington, A. S. (1920). The internal constitution of the stars. *The Observatory* 43, 341–358

Feast, M. (1999). Cepheids as Distance Indicators. *PASP* 111, 775–793. doi:10.1086/316386

Ferguson, J. W., Alexander, D. R., Allard, F., Barman, T., Bodnarik, J. G., Hauschildt, P. H., et al. (2005). Low-Temperature Opacities. *ApJ* 623, 585–596. doi:10.1086/428642

Figueira, P., Faria, J. P., Adibekyan, V. Z., Oshagh, M., and Santos, N. C. (2016). A Pragmatic Bayesian Perspective on Correlation Analysis. The exoplanetary gravity - stellar activity case. *Origins of Life and Evolution of the Biosphere* 46, 385–393. doi:10.1007/s11084-016-9490-5

Fiorentino, G., Annibali, F., Clementini, G., Ramos, R. C., Marconi, M., Musella, I., et al. (2013). Ultralong-period Cepheids: a possible primary distance indicator? In *Advancing the Physics of Cosmic Distances*, ed. R. de Grijs. vol. 289 of *IAU Symposium*, 282–286. doi:10.1017/S1743921312021552

Fontaine, G. and Michaud, G. (1979). Diffusion time scales in white dwarfs. *ApJ* 231, 826–840. doi:10.1086/157247

Foreman-Mackey, D., Hogg, D. W., Lang, D., and Goodman, J. (2013). emcee: The MCMC Hammer. *PASP* 125, 306. doi:10.1086/670067

Formicola, A., Imbriani, G., Costantini, H., Angulo, C., Bemmerer, D., Bonetti, R., et al. (2004). Astrophysical s-factor of 14n(p,)15o. *Physics Letters B* 591, 61 – 68. doi:https://doi.org/10.1016/j.physletb.2004.03.092

Formicola, A., Imbriani, G., Junker, M., Bemmerer, D., Bonetti, R., Broggini, C., et al. (2003). The luna ii 400kv accelerator. *Nuclear Instruments and Methods in Physics Research Section A: Accelerators, Spectrometers, Detectors and Associated Equipment* 507, 609 – 616. doi:https://doi.org/10.1016/S0168-9002(03)01435-9

Fröhlich, C., Romero, J., Roth, H., Wehrli, C., Andersen, B. N., Appourchaux, T., et al. (1995). VIRGO: Experiment for Helioseismology and Solar Irradiance Monitoring. *Solar Physics* 162, 101–128. doi:10.1007/BF00733428

Gabriel, A. H., Charra, J., Grec, G., Robillot, J.-M., Roca Cortés, T., Turck-Chièze, S., et al. (1997). Performance and Early Results from the GOLF Instrument Flown on the SOHO Mission. *Solar Physics* 175, 207–226. doi:10.1023/A:1004911408285

Gaia Collaboration, Brown, A. G. A., Vallenari, A., Prusti, T., de Bruijne, J. H. J., Mignard, F., et al. (2016). Gaia Data Release 1. Summary of the astrometric, photometric, and survey properties. *A&A* 595, A2. doi:10.1051/0004-6361/201629512

Gelly, B., Lazrek, M., Grec, G., Ayad, A., Schmider, F. X., Renaud, C., et al. (2002). Solar p-modes from 1979 days of the GOLF experiment. *A&A* 394, 285–297. doi:10.1051/0004-6361:20021106

Goldreich, P. and Keeley, D. A. (1977). Solar seismology. II - The stochastic excitation of the solar p-modes by turbulent convection. *ApJ* 212, 243–251. doi:10.1086/155043

Goldreich, P., Murray, N., and Kumar, P. (1994). Excitation of solar p-modes. *ApJ* 424, 466–479. doi:10.1086/173904

Goldreich, P., Murray, N., Willette, G., and Kumar, P. (1991). Implications of solar p-mode frequency shifts. *ApJ* 370, 752–762. doi:10.1086/169858

Gorshkov, A. B. and Baturin, V. A. (2008). Diffusion settling of heavy elements in the solar interior. *Astronomy Reports* 52, 760–771. doi:10.1134/S1063772908090072

Gough, D. (1990). *Comments on helioseismic inference, in Progress of Seismology of the Sun and Stars* (Springer Berlin Heidelberg). Lecture Notes in Physics, Vol 367, 283. doi:10.1007/3-540-53091-6_93

Goupil, M.-j. (2011). Effects of Rotation on Stellar p-Mode Frequencies. *arXiv e-prints* , arXiv:1102.1884

Goupil, M. J. (2018). Main uncertainties in characterizing planet host main sequence solar -like oscillating stars. In *SF2A-2018: Proceedings of the Annual meeting of the French Society of Astronomy and Astrophysics*. Di

Gregory, P. C. (2005). *Bayesian Logical Data Analysis for the Physical Sciences: A Comparative Approach with 'Mathematica' Support* (Cambridge University Press)

Grevesse, N., Asplund, M., and Sauval, A. J. (2007). The Solar Chemical Composition. *Space Science Reviews* 130, 105–114. doi:10.1007/s11214-007-9173-7

Grevesse, N. and Sauval, A. J. (1998). Standard Solar Composition. *Space Science Reviews* 85, 161–174. doi:10.1023/A:1005161325181

Gruberbauer, M., Guenther, D. B., and Kallinger, T. (2012). Toward a New Kind of Asteroseismic Grid Fitting. *ApJ* 749, 109. doi:10.1088/0004-637X/749/2/109

Gruberbauer, M., Guenther, D. B., MacLeod, K., and Kallinger, T. (2013). Bayesian asteroseismology of 23 solar-like Kepler targets. *MNRAS* 435, 242–254. doi:10.1093/mnras/stt1289

Guzik, J. A. and Cox, A. N. (1993). Using solar p-modes to determine the convection zone depth and constrain diffusion-produced composition gradients. *ApJ* 411, 394–401. doi:10.1086/172840

Guzik, J. A., Kaye, A. B., Bradley, P. A., Cox, A. N., and Neuforge, C. (2000). Driving the Gravity-Mode Pulsations in γ Doradus Variables. *ApJ* 542, L57–L60. doi:10.1086/312908

Hansen, C. J., Kawaler, S. D., and Trimble, V. (2004). *Stellar interiors : physical principles, structure, and evolution, 2nd ed. . New York: Springer-Verlag*

Harvey, J. W., Hill, F., Hubbard, R. P., Kennedy, J. R., Leibacher, J. W., Pintar, J. A., et al. (1996). The Global Oscillation Network Group (GONG) Project. *Science* 272, 1284–1286. doi:10.1126/science.272.5266.1284

Heasley, J. N., Janes, K., Labonte, B., Guenther, D., Mickey, D., and Demarque, P. (1996). The Prospects for Asteroseismology from Ground-based Sites. *PASP* 108, 385. doi:10.1086/133737

Henyey, L. G., Wilets, L., Böhm, K. H., Lelevier, R., and Levee, R. D. (1959). A Method for Automatic Computation of Stellar Evolution. *ApJ* 129, 628. doi:10.1086/146661

Herwig, F. (2000). The evolution of AGB stars with convective overshoot. *A&A* 360, 952–968

Hilditch, R. (1992). Book Review: Introduction to stellar astrophysics Vol. 3: Stellar structure and evolution / Cambridge U Press, 1992. *The Observatory* 112, 295

Hoffleit, D. (1997). History of the Discovery of Mira Stars. *Journal of the American Association of Variable Star Observers (JAAVSO)* 25, 115–136

Houdek, G. (2006). Stochastic excitation and damping of solar-like oscillations. In *Proceedings of SOHO 18/GONG 2006/HELAS I, Beyond the spherical Sun*. vol. 624 of *ESA Special Publication*, 28

Houdek, G., Balmforth, N. J., Christensen-Dalsgaard, J., and Gough, D. O. (1999). Amplitudes of stochastically excited oscillations in main-sequence stars. *A&A* 351, 582–596

Howe, R. (2009). Solar Interior Rotation and its Variation. *Living Reviews in Solar Physics* 6, 1. doi:10.12942/lrsp-2009-1

Hu, H., Tout, C. A., Glebbeek, E., and Dupret, M.-A. (2011). Slowing down atomic diffusion in subdwarf B stars: mass loss or turbulence? *MNRAS* 418, 195–205. doi:10.1111/j.1365-2966.2011.19482.x

Huber, D., Chaplin, W. J., Christensen-Dalsgaard, J., Gilliland, R. L., Kjeldsen, H., Buchhave, L. A., et al. (2013). Fundamental Properties of Kepler Planet-candidate Host Stars using Asteroseismology. *ApJ* 767, 127. doi:10.1088/0004-637X/767/2/127

Huber, D., Ireland, M. J., Bedding, T. R., Brandão, I. M., Piau, L., Maestro, V., et al. (2012). Fundamental Properties of Stars Using Asteroseismology from Kepler and CoRoT and Interferometry from the CHARA Array. *ApJ* 760, 32. doi:10.1088/0004-637X/760/1/32

Iglesias, C. A. and Rogers, F. J. (1996). Updated Opal Opacities. *ApJ* 464, 943. doi:10.1086/177381

Imbriani, G., Costantini, H., Formicola, A., Vomiero, A., Angulo, C., Bemmerer, D., et al. (2005). S-factor of ^{14}N(p,γ)^{15}O at astrophysical energies. *EPJ A* 25, 455–466. doi:10.1140/epja/i2005-10138-7

Itoh, N., Hayashi, H., Nishikawa, A., and Kohyama, Y. (1996). Neutrino Energy Loss in Stellar Interiors. VII. Pair, Photo-, Plasma, Bremsstrahlung, and Recombination Neutrino Processes. *ApJS* 102, 411. doi:10.1086/192264

Jiménez, A., Roca Cortés, T., and Jiménez-Reyes, S. J. (2002). Variation of the low-degree solar acoustic mode parameters over the solar cycle. *Solar Physics* 209, 247–263. doi:10.1023/A:1021226503589

Jimenez, R., Flynn, C., MacDonald, J., and Gibson, B. K. (2003). The Cosmic Production of Helium. *Science* 299, 1552–1555. doi:10.1126/science.1080866

Jørgensen, A. C. S., Weiss, A., Angelou, G., and Silva Aguirre, V. (2019). Mending the structural surface effect of 1D stellar structure models with non-solar metallicities based on interpolated 3D envelopes. *MNRAS* 484, 5551–5567. doi:10.1093/mnras/stz337

Joyce, M. and Chaboyer, B. (2018). Classically and Asteroseismically Constrained 1D Stellar Evolution Models of α Centauri A and B Using Empirical Mixing Length Calibrations. *ApJ* 864, 99. doi:10.3847/1538-4357/aad464

Jørgensen, A. C. S., Weiss, A., Mosumgaard, J. R., Silva Aguirre, V., and Sahlholdt, C. L. (2017). Theoretical oscillation frequencies for solar-type dwarfs from stellar models with 3D-atmospheres. *MNRAS* 472, 3264–3276. doi:10.1093/mnras/stx2226

Kafka, S. and Waagen, E. O. (2017). *Variable Stars, Royal Astronomical Society of Canada Observer's Handbook 2017, edited by James S. Edgar. Toronto: Royal Astronomical Society of Canada, 2016, p.298*

Kervella, P. (2008). Interferometric Angular Diameters, Linear Radii and Stellar Modeling. In *14th Cambridge Workshop on Cool Stars, Stellar Systems, and the Sun*, ed. G. van Belle. vol. 384 of *Astronomical Society of the Pacific Conference Series*, 189

Kervella, P., Bigot, L., et al. (2017). The radii and limb darkenings of α Centauri A and B . Interferometric measurements with VLTI/PIONIER. *A & A* 597, A137. doi:10.1051/0004-6361/201629505

Kervella, P., Mignard, F., et al. (2016). Close stellar conjunctions of α Centauri A and B until 2050 . An $m_K = 7.8$ star may enter the Einstein ring of α Cen A in 2028. *A & A* 594, A107. doi:10.1051/0004-6361/201629201

Kervella, P. et al. (2003). The diameters of alpha Centauri A and B. A comparison of the asteroseismic and VINCI/VLTI views. *A & A* 404, 1087–1097. doi:10.1051/0004-6361:20030570

Kim, Y.-C. (1999). Standard Stellar Models; alpha Cen A and B. *Journal of Korean Astronomical Society* 32, 119–126

Kippenhahn, R. and Weigert, A. (1990). *Stellar Structure and Evolution, Springer-Verlag Berlin Heidelberg New York. Also Astronomy and Astrophysics Library*

Kippenhahn, R., Weigert, A., and Weiss, A. (2012). *Stellar Structure and Evolution*. doi:10.1007/978-3-642-30304-3

Kjeldsen, H. and Bedding, T. R. (1995). Amplitudes of stellar oscillations: the implications for asteroseismology. *A&A* 293, 87–106

Kjeldsen, H., Bedding, T. R., Butler, R. P., Christensen-Dalsgaard, J., Kiss, L. L., McCarthy, C., et al. (2005). Solar-like Oscillations in α Centauri B. *ApJ* 635, 1281–1290. doi:10.1086/497530

Kjeldsen, H., Bedding, T. R., and Christensen-Dalsgaard, J. (2008). Correcting Stellar Oscillation Frequencies for Near-Surface Effects. *ApJL* 683, L175. doi:10.1086/591667

Kjeldsen, H. et al. (2004). Latest Observational Results of Solar-Like Oscillations in Other Stars. *ESA Special Publication* 559, 101

Korn, A. J., Grundahl, F., Richard, O., Mashonkina, L., Barklem, P. S., Collet, R., et al. (2007). Atomic Diffusion and Mixing in Old Stars. I. Very Large Telescope FLAMES-UVES Observations of Stars in NGC 6397. *ApJ* 671, 402–419. doi:10.1086/523098

Kunz, R., Fey, M., Jaeger, M., Mayer, A., Hammer, J. W., Staudt, G., et al. (2002). Astrophysical Reaction Rate of $^{12}C(\alpha, \gamma)^{16}O$. *ApJ* 567, 643–650. doi:10.1086/338384

Kurucz, R. L. (1993). *SYNTHE spectrum synthesis programs and line data, Cambridge, MA: Smithsonian Astrophysical Observatory*

Lamb, H. (1932). *Hydrodynamics, Dover, New York*

Leavitt, H. S. and Pickering, E. C. (1912). Periods of 25 Variable Stars in the Small Magellanic Cloud. *Harvard College Observatory Circular* 173, 1–3

Lebreton, Y. and Goupil, M. J. (2014). Asteroseismology for "à la carte" stellar age-dating and weighing. Age and mass of the CoRoT exoplanet host HD 52265. *A & A* 569, A21. doi:10.1051/0004-6361/201423797

Lebreton, Y., Goupil, M. J., and Montalbán, J. (2014). How accurate are stellar ages based on stellar models?. I. The impact of stellar models uncertainties. In *EAS Publications Series*. vol. 65 of *EAS Publications Series*, 99–176. doi:10.1051/eas/1465004

Ledoux, P. (1947). On stellar models with convection and discontinuity of the mean molecular weight. *AJ* 52, 155. doi:10.1086/105977

Ledoux, P. and Walraven, T. (1958). Variable Stars. *Handbuch der Physik* 51, 353–604

Leighton, R. B., Noyes, R. W., and Simon, G. W. (1962). Velocity Fields in the Solar Atmosphere. I. Preliminary Report. *ApJ* 135, 474. doi:10.1086/147285

Ligi, R., Creevey, O., et al. (2016). Radii, masses, and ages of 18 bright stars using interferometry and new estimations of exoplanetary parameters. *A & A* 586, A94. doi:10.1051/0004-6361/201527054

Lo, K. Y. and Bechis, K. P. (1977). Variable 2.6 MM CO emission from Chi Cygni and Mira. *ApJL* 218, L27–L30. doi: 10.1086/182569

Lodders, K. (2003). Solar System Abundances and Condensation Temperatures of the Elements. *ApJ* 591, 1220–1247. doi: 10.1086/375492

Lodders, K. and Palme, H. (2009). Solar System Elemental Abundances in 2009. *Meteoritics and Planetary Science Supplement* 72, 5154

Lund, M. N. and Reese, D. R. (2018). Tutorial: Asteroseismic Stellar Modelling with AIMS. *Asteroseismology and Exoplanets: Listening to the Stars and Searching for New Worlds* 49, 149. doi:10.1007/978-3-319-59315-9_8

Lund, M. N., Silva Aguirre, V., Davies, G. R., Chaplin, W. J., Christensen-Dalsgaard, J., Houdek, G., et al. (2017). Standing on the Shoulders of Dwarfs: the Kepler Asteroseismic LEGACY Sample. I. Oscillation Mode Parameters. *ApJ* 835, 172. doi: 10.3847/1538-4357/835/2/172

Lundkvist, M., Kjeldsen, H., and Silva Aguirre, V. (2014). AME - Asteroseismology Made Easy. Estimating stellar properties by using scaled models. *A&A* 566, A82. doi:10.1051/0004-6361/201423408

MacDonald, J. (2015). *Structure and Evolution of Single Stars; An introduction.* doi: 10.1088/978-1-6817-4105-5

Maeder, A. (1974). Stellar evolution near the main sequence: on some systematic differences between cluster sequences and model calculations. *A&A* 32, 177–190

Maeder, A. (2009). *Physics, Formation and Evolution of Rotating Stars.* doi:10.1007/978-3-540-76949-1

Maeder, A. and Meynet, G. (2000). The Evolution of Rotating Stars. *Annual Review of Astron and Astrophys* 38, 143–190. doi: 10.1146/annurev.astro.38.1.143

Magic, Z., Serenelli, A., Weiss, A., and Chaboyer, B. (2010). ON USING THE COLOR-MAGNITUDE DIAGRAM MORPHOLOGY OF m67 TO TEST SOLAR ABUNDANCES. *The Astrophysical Journal* 718, 1378–1387. doi:10.1088/0004-637x/718/2/1378

Mamajek, E. E. (2012). On the age and binarity of fomalhaut. *ApJL* 754, L20

Marcy, G. W., Isaacson, H., Howard, A. W., Rowe, J. F., Jenkins, J. M., Bryson, S. T., et al. (2014). Masses, Radii, and Orbits of Small Kepler Planets: The Transition from Gaseous to Rocky Planets. *ApJS* 210, 20. doi:10.1088/0067-0049/210/2/20

Mathur, S., Metcalfe, T. S., Woitaszek, M., Bruntt, H., Verner, G. A., Christensen-Dalsgaard, J., et al. (2012). A Uniform Asteroseismic Analysis of 22 Solar-type Stars Observed by Kepler. *ApJ* 749, 152. doi: 10.1088/0004-637X/749/2/152

Metcalfe, T. S., Chaplin, W. J., Appourchaux, T., García, R. A., Basu, S., Brandão, I., et al. (2012). Asteroseismology of the Solar Analogs 16 Cyg A and B from Kepler Observations. *APJL* 748, L10. doi: 10.1088/2041-8205/748/1/L10

Metcalfe, T. S., Creevey, O. L., and Christensen-Dalsgaard, J. (2009). A Stellar Model-fitting Pipeline for Asteroseismic Data from the Kepler Mission. *ApJ* 699, 373–382. doi:10.1088/0004-637X/699/1/373

Metcalfe, T. S., Creevey, O. L., and Christensen-Dalsgaard, J. (2009). A STELLAR MODEL-FITTING PIPELINE FOR ASTEROSEISMIC DATA FROM THEKEPLERMISSION. *The Astrophysical Journal* 699, 373–382. doi:10.1088/0004-637x/699/1/373

Metcalfe, T. S., Creevey, O. L., Doğan, G., Mathur, S., Xu, H., Bedding, T. R., et al. (2014). Properties of 42 Solar-type Kepler Targets from the Asteroseismic Modeling Portal. *ApJS* 214, 27. doi:10.1088/0067-0049/214/2/27

Michaud, G. (1970). Diffusion Processes in Peculiar a Stars. *ApJ* 160, 641. doi: 10.1086/150459

Michaud, G., Charland, Y., Vauclair, S., and Vauclair, G. (1976). Diffusion in main-sequence stars - Radiation forces, time scales, anomalies. *ApJ* 210, 447–465. doi: 10.1086/154848

Michaud, G., Richer, J., and Richard, O. (2008). Abundance Anomalies in Horizontal Branch Stars and Atomic Diffusion. *ApJ* 675, 1223–1232. doi:10.1086/527541

Michaud, G., Vauclair, G., and Vauclair, S. (1983). Chemical separation in horizontal-branch stars. *ApJ* 267, 256–270. doi: 10.1086/160864

Miglio, A., Brogaard, K., Stello, D., Chaplin, W. J., D'Antona, F., Montalbán, J., et al. (2012). Asteroseismology of old open clusters with Kepler: direct estimate of the integrated red giant branch mass-loss in NGC 6791 and 6819. *MNRAS* 419, 2077–2088. doi:10.1111/j.1365-2966.2011.19859.x

Miglio, A. and Montalbán, J. (2005). Constraining fundamental stellar parameters using seismology. Application to α Centauri AB. *A&A* 441, 615–629. doi:10.1051/0004-6361:20052988

Monteiro, M. J. P. F. G. (2008). Porto Oscillation Code (posc). *AP&SS* 316, 121–127. doi:10.1007/s10509-008-9802-y

Monteiro, M. J. P. F. G. (2009). *Evolution and Seismic Tools for Stellar Astrophysics, Astrophysics and Space Science, vol. 316. 261 pages. Springer.*

Monteiro, M. J. P. F. G., Christensen-Dalsgaard, J., and Thompson, M. J. (1996). Seismic properties of the Sun's superadiabatic layer. I. Theoretical modelling and parametrization of the uncertainties. *A & A* 307, 624–634

Mosser, B., Michel, E., Belkacem, K., Goupil, M. J., Baglin, A., Barban, C., et al. (2013). Asymptotic and measured large frequency separations. *A&A* 550, A126. doi:10.1051/0004-6361/201220435

Mowlavi, N., Eggenberger, P., Meynet, G., Ekström, S., Georgy, C., Maeder, A., et al. (2012). Stellar mass and age determinations . I. Grids of stellar models from Z = 0.006 to 0.04 and M = 0.5 to 3.5 M. *A&A* 541, A41. doi:10.1051/0004-6361/201117749

Moya, A., Christensen-Dalsgaard, J., Charpinet, S., Lebreton, Y., Miglio, A., Montalbán, J., et al. (2008). Intercomparison of the g-, f- and p-modes calculated using different oscillation codes for a given stellar model. *Ap&SS* 316, 231–249. doi:10.1007/s10509-007-9717-z

Moya, A. and Garrido, R. (2008). Granada oscillation code (GraCo). *Astrophysics and Space Science* 316, 129–133. doi:10.1007/s10509-007-9694-2

Noerdlinger, P. D. (1977). Diffusion of helium in the sun. *A&A* 57, 407–415

North, J. R., Davis, J., Bedding, T. R., Ireland , M. J., Jacob, A. P., O'Byrne, J., et al. (2007). The radius and mass of the subgiant star β Hyi from interferometry and asteroseismology. *MNRAS* 380, L80–L83. doi:10.1111/j.1745-3933.2007.00355.x

Nsamba, B., Jurua, E., and Anguma, K. S. (2014). *Mass Loss and Age of the Rgc Stars in the Kepler Cluster Ngc 6819. ISBN 10: 3659637149. Published by LAP Lambert Academic Publishing.*

Nsamba, B., Monteiro, M. J. P. F. G., Campante, T. L., Cunha, M. S., and Sousa, S. G. (2018a). α Centauri A as a potential stellar model calibrator: establishing the nature of its core. *MNRAS* 479, L55–L59. doi:10.1093/mnrasl/sly092

Nsamba, B., Monteiro, M. J. P. F. G., Campante, T. L., Reese, D. R., White, T. R., García Hernández, A., et al. (2017). Asteroseismic modelling of the binary hd 176465. *EPJ Web Conf.* 160, 05010. doi: 10.1051/epjconf/201716005010

Nsamba, B. et al. (2018b). Asteroseismic modelling of solar-type stars: internal systematics from input physics and surface correction methods. *MNRAS* arXiv:1804.04935. doi:10.1093/mnras/sty948

Paxton, B., Bildsten, L., Dotter, A., Herwig, F., Lesaffre, P., and Timmes, F. (2011). Modules for Experiments in Stellar Astrophysics (MESA). *ApJS* 192, 3. doi:10.1088/0067-0049/192/1/3

Paxton, B., Cantiello, M., Arras, P., Bildsten, L., Brown, E. F., Dotter, A., et al. (2013). Modules for Experiments in Stellar Astrophysics (MESA): Planets, Oscillations, Rotation, and Massive Stars. *ApJS* 208, 4. doi:10.1088/0067-0049/208/1/4

Paxton, B., Marchant, P., Schwab, J., Bauer, E. B., Bildsten, L., Cantiello, M., et al. (2015). Modules for Experiments in Stellar Astrophysics (MESA): Binaries, Pulsations, and Explosions. *ApJS* 220, 15. doi:10.1088/0067-0049/220/1/15

Paxton, B., Schwab, J., Bauer, E. B., Bildsten, L., Blinnikov, S., Duffell, P., et al. (2018). Modules for Experiments in Stellar Astrophysics (MESA): Convective Boundaries, Element Diffusion, and Massive Star Explosions. *ApJS* 234, 34. doi:10.3847/1538-4365/aaa5a8

Peimbert, M. and Torres-Peimbert, S. (1976). Chemical composition of H II regions in the Small Magellanic Cloud and the pregalactic helium abundance. *ApJ* 203, 581–586. doi:10.1086/154114

Perryman, M. (2014). *The Exoplanet Handbook, Cambridge, UK: Cambridge University Press*

Piau, L., Kervella, P., Dib, S., and Hauschildt, P. (2011). Surface convection and red-giant radius measurements. *A & A* 526, A100. doi:10.1051/0004-6361/201014442

Pietrinferni, A., Cassisi, S., Salaris, M., and Castelli, F. (2004). A Large Stellar Evolution Database for Population Synthesis Studies. I. Scaled Solar Models and Isochrones. *ApJ* 612, 168–190. doi:10.1086/422498

Pijpers, F. P. (2003). Selection criteria for targets of asteroseismic campaigns. *A&A* 400, 241–248. doi:10.1051/0004-6361:20021839

Pijpers, F. P., Teixeira, T. C., Garcia, P. J., Cunha, M. S., Monteiro, M. J. P. F. G., and Christensen-Dalsgaard, J. (2003). Interferometry and asteroseismology: The radius of tau Cet. *A&A* 406, L15–L18. doi:10.1051/0004-6361:20030837

Pinheiro, F. J. G. and Fernandes, J. (2013). On the (non-)universality of the mixing length parameter. *MNRAS* 433, 2893–2899. doi:10.1093/mnras/stt910

Pinsonneault, M. H., An, D., Molenda-Żakowicz, J., Chaplin, W. J., Metcalfe, T. S., and Bruntt, H. (2012). A Revised Effective Temperature Scale for the Kepler Input Catalog. *ApJS* 199, 30. doi:10.1088/0067-0049/199/2/30

Pinsonneault, M. H., Elsworth, Y., Epstein, C., Hekker, S., Mészáros, S., Chaplin, W. J., et al. (2014). The APOKASC Catalog: An Asteroseismic and Spectroscopic Joint Survey of Targets in the Kepler Fields. *ApJS* 215, 19. doi:10.1088/0067-0049/215/2/19

Pols, O. (2011). *Stellar structure and evolution:Lecture notes for a Utrecht University, Astronomical Institute Utrecht*

Porceddu, S., Jetsu, L., Markkanen, T., and Toivari-Viitala, J. (2008). Evidence of periodicity in ancient egyptian calendars of lucky and unlucky days. *Cambridge Archaeological Journal* 18, 327–339. doi:10.1017/S0959774308000395

Pourbaix, D. and Boffin, H. M. J. (2016). Parallax and masses of α Centauri revisited. *A & A* 586, A90. doi:10.1051/0004-6361/201527859

Pourbaix, D., Nidever, D., et al. (2002). Constraining the difference in convective blueshift between the components of alpha Centauri with precise radial velocities. *A*

& A 386, 280–285. doi:10.1051/0004-6361:20020287

Pourbaix, D. et al. (1999). Revised masses of alpha Centauri. *A & A* 344, 172–176

Prandtl, L. and Angew, Z. (1925). *Math. Mech.* 5, 136

Prialnik, D. (2000). *An Introduction to the Theory of Stellar Structure and Evolution ISBN 052165937X. <A*

Prialnik, D. (2009). *An Introduction to the Theory of Stellar Structure and Evolution, Cambridge, UK, Cambridge University Press*

Ramírez, I., Meléndez, J., and Asplund, M. (2009). Accurate abundance patterns of solar twins and analogs. Does the anomalous solar chemical composition come from planet formation? *A & A* 508, L17–L20. doi:10.1051/0004-6361/200913038

Rau, M. M., Koposov, S. E., Trac, H., and Mand elbaum, R. (2019). Calibrating long-period variables as standard candles with machine learning. *MNRAS* 484, 409–421. doi:10.1093/mnras/sty3495

Rauer, H., Catala, C., Aerts, C., Appourchaux, T., Benz, W., Brandeker, A., et al. (2014). The PLATO 2.0 mission. *Experimental Astronomy* 38, 249–330. doi:10.1007/s10686-014-9383-4

Reid, I. N. and Hawley, S. L. (2005). *New light on dark stars : red dwarfs, low-mass stars, brown dwarfs*. doi:10.1007/3-540-27610-6

Rendle, B. M., Buldgen, G., Miglio, A., Reese, D., Noels, A., Davies, G. R., et al. (2019). AIMS - a new tool for stellar parameter determinations using asteroseismic constraints. *MNRAS* 484, 771–786. doi:10.1093/mnras/stz031

Renzo, M. (2014). *MESA Workshop: Notes.*

Richard, O., Vauclair, S., Charbonnel, C., and Dziembowski, W. A. (1996). New solar models including helioseismological constraints and light-element depletion. *A&A* 312, 1000–1011

Richer, J., Michaud, G., and Turcotte, S. (2000). The Evolution of AMFM Stars, Abundance Anomalies, and Turbulent Transport. *ApJ* 529, 338–356. doi:10.1086/308274

Ricker, G. R., Winn, J. N., Vanderspek, R., Latham, D. W., Bakos, G. Á., Bean, J. L., et al. (2015). Transiting Exoplanet Survey Satellite (TESS). *Journal of Astronomical Telescopes, Instruments, and Systems* 1, 014003. doi:10.1117/1.JATIS.1.1.014003

Rodrigues, T. S., Bossini, D., Miglio, A., Girardi, L., Montalbán, J., Noels, A., et al. (2017). Determining stellar parameters of asteroseismic targets: going beyond the use of scaling relations. *MNRAS* 467, 1433–1448. doi:10.1093/mnras/stx120

Rogers, F. J. and Nayfonov, A. (2002). Updated and Expanded OPAL Equation-of-State Tables: Implications for Helioseismology. *ApJ* 576, 1064–1074. doi:10.1086/341894

Rosenthal, C. S., Christensen-Dalsgaard, J., Nordlund, Å., Stein, R. F., and Trampedach, R. (1999). Convective contributions to the frequencies of solar oscillations. *A&A* 351, 689–700

Rosseland, S. and Randers, G. (1938). On the Stability of Pulsating Stars. *Astrophysica Norvegica* 3, 71

Roxburgh, I. W. and Vorontsov, S. V. (2003). *A & A* 411, 215–220. doi:10.1051/0004-6361:20031318

Samadi, R., Georgobiani, D., Trampedach, R., Goupil, M. J., Stein, R. F., and Nordlund, Å. (2007). Excitation of solar-like oscillations across the HR diagram. *A&A* 463, 297–308. doi:10.1051/0004-6361:20041953

Samadi, R. and Goupil, M.-J. (2001). Excitation of stellar p-modes by turbulent convection. I. Theoretical formulation. *A&A* 370, 136–146. doi:10.1051/0004-6361:20010212

Samus, N. N., Kazarovets, E. V., Durlevich, O. V., Kireeva, N. N., and Pastukhova, E. N. (2009). VizieR Online Data Catalog: General Catalogue of Variable Stars (Samus+, 2007-2017). *VizieR Online Data Catalog* 1

Sandage, A. (1999). Bias Properties of Extragalactic Distance Indicators. VIII. H_0 from Distance-limited Luminosity Class and Morphological Type-Specific Luminosity Functions for SB, SBC, and SC Galaxies Calibrated Using Cepheids. *ApJ* 527, 479–487. doi:10.1086/308123

Schlattl, H., Weiss, A., and Ludwig, H.-G. (1997). A solar model with improved subatmospheric stratification. *A&A* 322, 646–652

Schwarzschild, M. (1958). *Structure and evolution of the stars, Princeton, Princeton University Press.*

Schwarzschild, M. (1965). *Structure and evolution of the stars, New York: Dover Publication.*

Serenelli, A. M. and Basu, S. (2010). Determining the Initial Helium Abundance of the Sun. *ApJ* 719, 865–872. doi:10.1088/0004-637X/719/1/865

Serenelli, A. M., Basu, S., Ferguson, J. W., and Asplund, M. (2009). New Solar Composition: The Problem with Solar Models Revisited. *ApJL* 705, L123–L127. doi:10.1088/0004-637X/705/2/L123

Shapley, H. (1914). On the Nature and Cause of Cepheid Variation. *ApJ* 40, 448. doi:10.1086/142137

Shapley, H. (1961). *Galaxies. https://ui.adsabs.harvard.edu/abs/1961gala.book.....S*

Silva Aguirre, V., Ballot, J., Serenelli, A. M., and Weiss, A. (2011a). Constraining mixing processes in stellar cores using asteroseismology. Impact of semiconvection in low-mass stars. *A & A* 529, A63. doi:10.1051/0004-6361/201015847

Silva Aguirre, V., Chaplin, W. J., Ballot, J., Basu, S., Bedding, T. R., Serenelli, A. M., et al. (2011b). Constructing a One-solar-mass Evolutionary Sequence Using Asteroseismic Data from Kepler. *ApJ* 740, L2. doi:10.1088/2041-8205/740/1/L2

Silva Aguirre, V., Davies, G. R., Basu, S., Christensen-Dalsgaard, J., Creevey, O., Metcalfe, T. S., et al. (2015). Ages and fundamental properties of Kepler exoplanet host stars from asteroseismology. *MNRAS* 452, 2127–2148. doi:10.1093/mnras/stv1388

Silva Aguirre, V., Lund, M. N., Antia, H. M., Ball, W. H., Basu, S., Christensen-Dalsgaard, J., et al. (2017). Standing on the Shoulders of Dwarfs: the Kepler Asteroseismic LEGACY Sample. II.Radii, Masses, and Ages. *ApJ* 835, 173. doi:10.3847/1538-4357/835/2/173

Silva Aguirre, V. et al. (2013). Stellar Ages and Convective Cores in Field Main-sequence Stars: First Asteroseismic Application to Two Kepler Targets. *ApJ* 769, 141. doi:10.1088/0004-637X/769/2/141

Sneden, C. A. (1973). *Carbon and Nitrogen Abundances in Metal-Poor Stars.* Ph.D. thesis, THE UNIVERSITY OF TEXAS

Söderhjelm, S. (1999). Visual binary orbits and masses POST HIPPARCOS. *A & A* 341, 121–140

Sonoi, T., Samadi, R., Belkacem, K., Ludwig, H.-G., Caffau, E., and Mosser, B. (2015). Surface-effect corrections for solar-like oscillations using 3D hydrodynamical simulations. I. Adiabatic oscillations. *A & A* 583, A112. doi:10.1051/0004-6361/201526838

Sousa, S. G. (2014). *ARES + MOOG: A Practical Overview of an Equivalent Width (EW) Method to Derive Stellar Parameters.* 297–310

Sousa, S. G., Santos, N. C., et al. (2007). A new code for automatic determination of equivalent widths: Automatic Routine

for line Equivalent widths in stellar Spectra (ARES). *A & A* 469, 783–791. doi: 10.1051/0004-6361:20077288

Sousa, S. G., Santos, N. C., et al. (2011). Spectroscopic stellar parameters for 582 FGK stars in the HARPS volume-limited sample. Revising the metallicity-planet correlation. *A & A* 533, A141. doi:10.1051/0004-6361/201117699

Sousa, S. G., Santos, N. C., et al. (2015). ARES v2: new features and improved performance. *A & A* 577, A67. doi: 10.1051/0004-6361/201425463

Stancliffe, R. J., Fossati, L., Passy, J.-C., and Schneider, F. R. N. (2016). Confronting uncertainties in stellar physics. II. Exploring differences in main-sequence stellar evolution tracks. *A&A* 586, A119. doi: 10.1051/0004-6361/201527099

Stein, R., Georgobiani, D., Trampedach, R., Ludwig, H.-G., and Nordlund, Å. (2004). Excitation of Radial P-Modes in the Sun and Stars. *Solar Physics* 220, 229–242. doi: 10.1023/B:SOLA.0000031458.35121.33

Stein, R. F. (1967). Generation of Acoustic and Gravity Waves by Turbulence in an Isothermal Stratified Atmosphere. *Solar Physics* 2, 385–432. doi:10.1007/BF00146490

Stein, R. F. and Nordlund, Å. (1991). Convection and Its Influence on Oscillations. In *Challenges to Theories of the Structure of Moderate-Mass Stars*, eds. D. Gough and J. Toomre. vol. 388 of *Lecture Notes in Physics, Berlin Springer Verlag*, 195. doi: 10.1007/3-540-54420-8_67

Stein, R. F. and Nordlund, Å. (2001). Solar Oscillations and Convection. II. Excitation of Radial Oscillations. *ApJ* 546, 585–603. doi:10.1086/318218

Stello, D., Bruntt, H., Preston, H., and Buzasi, D. (2008). Oscillating K Giants with the WIRE Satellite: Determination of Their Asteroseismic Masses. *ApJ* 674, L53. doi: 10.1086/528936

Storm, J. (2006). How good are RR Lyrae and Cepheids really as distance indicators? . The observational approach. *MmSAI* 77, 188

Suárez, J. C., Goupil, M. J., and Morel, P. (2006). Effects of moderately fast shellular rotation on adiabatic oscillations. *A&A* 449, 673–685. doi:10.1051/0004-6361:20054181

Takata, M. (2005). Momentum Conservation and Mode Classification of the Dipolar Oscillations of Stars. *PASJ* 57, 375–389. doi:10.1093/pasj/57.2.375

Tassoul, M. (1980). Asymptotic approximations for stellar nonradial pulsations. *ApJS* 43, 469–490. doi:10.1086/190678

Thévenin, F., Kervella, P., Pichon, B., Morel, P., di Folco, E., and Lebreton, Y. (2005). VLTI/VINCI diameter constraints on the evolutionary status of δ Eri, ξ Hya, η Boo. *A&A* 436, 253–262. doi:10.1051/0004-6361:20042075

Thompson, M. J. (2004). Helioseismology and the Sun's interior. *Astronomy & Geophysics* 45, 4.21–4.25. doi:10.1046/j.1468-4004.2003.45421.x

Thoul, A., Scuflaire, R., et al. (2003). A new seismic analysis of Alpha Centauri. *A & A* 402, 293–297. doi:10.1051/0004-6361:20030244

Thoul, A. A., Bahcall, J. N., and Loeb, A. (1994). Element diffusion in the solar interior. *ApJ* 421, 828–842. doi:10.1086/173695

Torres, G. (2010). On the Use of Empirical Bolometric Corrections for Stars. *AJ* 140, 1158–1162. doi:10.1088/0004-6256/140/5/1158

Torres, G., Fischer, D. A., Sozzetti, A., Buchhave, L. A., Winn, J. N., Holman, M. J., et al. (2012). Improved Spectroscopic Parameters for Transiting Planet Hosts. *ApJ* 757, 161. doi:10.1088/0004-637X/757/2/161

Townsend, R. H. D. and Teitler, S. A. (2013). GYRE: an open-source stellar oscillation code based on a new Magnus Multiple Shooting scheme. *MNRAS* 435, 3406–3418. doi:10.1093/mnras/stt1533

Trampedach, R. and Stein, R. F. (2011). The Mass Mixing Length in Convective Stellar Envelopes. *ApJ* 731, 78. doi: 10.1088/0004-637X/731/2/78

Trampedach, R., Stein, R. F., Christensen-Dalsgaard, J., Nordlund, Å., and Asplund, M. (2014). Improvements to stellar structure models, based on a grid of 3D convection simulations - II. Calibrating the mixing-length formulation. *MNRAS* 445, 4366–4384. doi:10.1093/mnras/stu2084

Turcotte, S., Richer, J., Michaud, G., Iglesias, C. A., and Rogers, F. J. (1998). Consistent Solar Evolution Model Including Diffusion and Radiative Acceleration Effects. *ApJ* 504, 539–558. doi:10.1086/306055

Ulrich, R. K. (1970). The Five-Minute Oscillations on the Solar Surface. *ApJ* 162, 993. doi:10.1086/150731

Ulrich, R. K. (1986). Determination of stellar ages from asteroseismology. *ApJ* 306, L37–L40. doi:10.1086/184700

Unno, W., Osaki, Y., Ando, H., Saio, H., and Shibahashi, H. (1989). *Nonradial oscillations of stars. Tokyo: University of Tokyo Press*

Unno, W., Osaki, Y., Ando, H., and Shibahashi, H. (1979). *Nonradial oscillations of stars*

Valle, G., Dell'Omodarme, M., Prada Moroni, P. G., and Degl'Innocenti, S. (2014). Uncertainties in grid-based estimates of stellar mass and radius. SCEPtER: Stellar CharactEristics Pisa Estimation gRid. *A & A* 561, A125. doi:10.1051/0004-6361/201322210

Van Eylen, V., Kjeldsen, H., Christensen-Dalsgaard, J., and Aerts, C. (2012). Properties of extrasolar planets and their host stars: A case study of HAT-P-7. *Astronomische Nachrichten* 333, 1088. doi: 10.1002/asna.201211832

VandenBerg, D. A., Gustafsson, B., Edvardsson, B., Eriksson, K., and Ferguson, J. (2007). A Constraint on Z_{solar} from Fits of Isochrones to the Color-Magnitude Diagram of M67. *ApJ* 666, L105–L108. doi: 10.1086/521877

VandenBerg, D. A., Richard, O., Michaud, G., and Richer, J. (2002). Models of Metal-poor Stars with Gravitational Settling and Radiative Accelerations. II. The Age of the Oldest Stars. *ApJ* 571, 487–500. doi: 10.1086/339895

Vauclair, S. (1998). Evidence of Element Diffusion Inside the Sun and the Stars and its Consequences on the Lithium Primordial Abundance. *SSRv* 84, 265–271

Vauclair, S. and Vauclair, G. (1982). Element segregation in stellar outer layers. *ARA&A* 20, 37–60. doi:10.1146/annurev.aa.20.090182.000345

Verma, K. (2016). *Asteroseismology of sun-like main–sequence stars: inferences using acoustic glitch and machine learning approach.* Ph.D. thesis, Tata Institute of Fundamental Research, Mumbai, India

Verma, K., Raodeo, K., Antia, H. M., Mazumdar, A., Basu, S., Lund, M. N., et al. (2017). Seismic Measurement of the Locations of the Base of Convection Zone and Helium Ionization Zone for Stars in the Kepler Seismic LEGACY Sample. *ApJ* 837, 47. doi: 10.3847/1538-4357/aa5da7

Verma, K., Raodeo, K., Basu, S., Silva Aguirre, V., Mazumdar, A., Mosumgaard, J. R., et al. (2019). Helium abundance in a sample of cool stars: measurements from asteroseismology. *MNRAS* 483, 4678–4694. doi:10.1093/mnras/sty3374

Vorontsov, S. V., Baturin, V. A., et al. (2013). Helioseismic calibration of the equation of state and chemical composition in the solar convective envelope. *MNRAS* 430, 1636–1652. doi:10.1093/mnras/sts701

White, T. R., Benomar, O., Silva Aguirre, V., Ball, W. H., Bedding, T. R., Chaplin, W. J., et al. (2017). Kepler observations of the asteroseismic binary HD 176465. *A&A* 601, A82. doi:10.1051/0004-6361/201628706

White, T. R., Huber, D., Maestro, V., Bedding, T. R., Ireland, M. J., Baron, F., et al. (2013). Interferometric radii of bright Kepler stars with the CHARA Array: thetas Cygni and 16 Cygni A and B. *MNRAS* 433, 1262–1270. doi:10.1093/mnras/stt802

Xiong, D. R. and Deng, L. (2007). Non-adiabatic oscillations of red giants. *MNRAS* 378, 1270–1282. doi:10.1111/j.1365-2966.2007.11642.x

Yang, J. Y., Li, Y., and Xu, H. Y. (2001). Solar model: Element diffusion or metal-enhanced envelope? *A&A* 366, 311–316. doi:10.1051/0004-6361:20000290

Yıldız, M. (2007). Models of α Centauri A and B with and without seismic constraints: time dependence of the mixing-length parameter. *MNRAS* 374, 1264–1270. doi:10.1111/j.1365-2966.2006.11218.x

Appendix A

Other applications

The stellar modelling skills developed during this research period were not only limited to exploring the stellar physics and systematic uncertainties on the derived stellar parameters, but were also employed in other research activities. These include:

— Contributions to the modelling of six exoplanet–hosts with long–period giant planets discovered using radial velocities. The exoplanet–host stars were modelled using stellar evolutionary models generated with MESA (Paxton et al. 2011, 2013, 2015, 2018). The physics used when constructing the stellar grid is similar to that

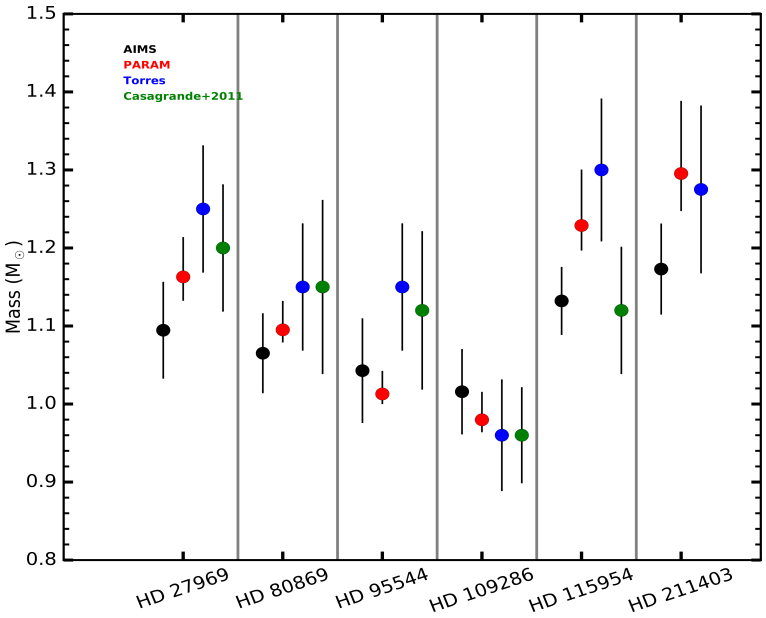

Figure A.1: Comparison of stellar masses derived using the optimisation tools AIMS and PARAM (Rodrigues et al., 2017), and the calibrations of Torres (2010) and Casagrande et al. (2011). See text for details.

in the GS98sta grid described in Sect. 4.4. I note that the stellar mass interval was extended to cover the range $M \in [0.7 - 1.6]$ $M_{\odot}$. In addition, for stars with a mass above 1.1 $M_{\odot}$, core overshoot was also included following the description of Herwig (2000). During the optimisation process conducted with AIMS, I adopted several observable constraints, namely, effective temperature, metallicity, and a parallax–based luminosity. I note that no seismic data are available for these stars. I included systematic uncertainties of 59 K in effective temperature and 0.062 dex in metallicity that arise from variations in spectroscopic methods as described by Torres et al. (2012). The stellar luminosities were calculated using equation 1 of Pijpers (2003). Figure A.1 shows the stellar masses obtained using AIMS and PARAM (see Rodrigues et al. 2017), compared to values obtained based on the Torres (2010) calibration and Casagrande et al. (2011). In general, the results are in agreement within 2σ. These stellar parameters are being employed in the characterisation of their orbiting planets in Demangeon et al. (in prep).

— Another vital contribution is to the “Hare & Hounds” modelling of both main –sequence and subgiant stars in the framework of PLATO. As part of this effort, I adopted a grid of subgiant stellar models developed using MESA by the team at the Stellar Astrophysics Centre in Aarhus –, Denmark, and applied AIMS to fit a set of seismic and classical constraints for six artificial targets. The results were compared to the "truth" by Dr. Margarida S. Cunha and are to be presented at the “PLATO Stellar Science Workshop” in Barcelona –, Spain. In addition, a detailed assessment of the model grid density needed so as to successfully fit the mixed modes of subgiant stars without diverting from the "true" stellar parameters, is being carried out together with a master’s student (Mr. Miguel T. Clara), supervised by Dr. Tiago L. Campante and Dr. Margarida S. Cunha. My contribution to this research activity involved introducing Mr. Miguel to the MESA, GYRE, and AIMS codes. The preliminary findings show that, for a grid with 500 subgiant evolutionary tracks, a minimum of 60 models along each subgiant track are required so as to successfully fit the mixed modes. Having a less dense grid yields significant systematic uncertainties on the derived stellar parameters.

— An interesting study has also been carried out together with undergraduate students Ms. Catarina I. S. A. Rocha and Mr. Cristiano J. G. N. Pereira, under supervision of Dr. Tiago L. Campante and Dr. Margarida S. Cunha. In this study, it is shown that forward modelling routines that involve fitting a set of classical

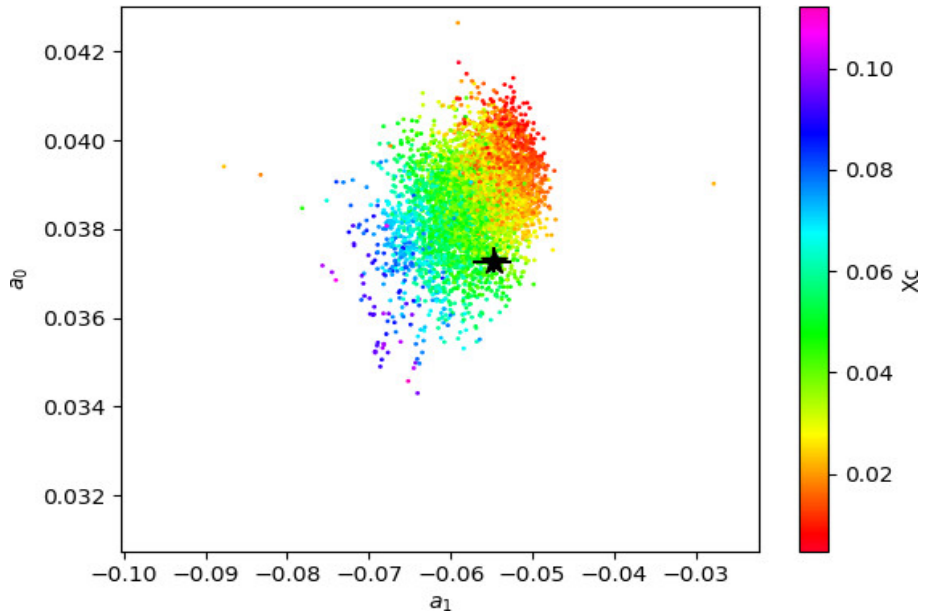

Figure A.2: (a_1, a_0) plane for the best–fit models colour coded according to their corresponding central hydrogen abundance (X_c). The Black "star" shows the position of 16 Cyg A. See text for details. Figure courtesy of Ms. Catarina I. S. A. Rocha and Mr. Cristiano J. G. N. Pereira.

constraints (i.e., effective temperature and metallicity) and individual oscillation frequencies as seismic constraints yield optimal models with the expected stellar parameters (mass, radius, and age) but with different internal structures. Here, I highlight the results on 16 Cyg A. I modelled this star taking into account similar model physics to that described in Chapter 5, and applied AIMS to generate models that fit a set of observables within 3σ. I note that individual oscillation frequencies were fitted during this process. For each of the best–fit models obtained, Ms. Rocha and Mr. Pereira fitted 2nd–order polynomials (see equation 6 in Deheuvels et al. 2016) to the frequency ratios r_{10} (Roxburgh and Vorontsov, 2003) and obtained the coefficients a_0 and a_1. Figure A.2 shows the (a_1, a_0) plane for the models colour–coded according to their corresponding central hydrogen abundance (X_c). Only models with X_c in the range from $\sim$ 0.04 to 0.06 satisfy the observed ratios (see Fig. A.2). These results suggest that additional constraints are required in the forward modelling routines so as to generate best–fit models with interior properties (such as central hydrogen abundance) similar to predictions based on frequency ratios. The results of this study are to be presented in the workshop titled “Dynamics of the Sun & Stars: Honoring the Life & Work of Michael Thompson” in Boulder, Colorado –, USA.